EFFECTS OF Ag ON STRUCTURAL AND MAGNETIC PROPERTIES OF FePt THIN FILMS

ZHOU YONGZHONG
(***B. Eng. University of Electronic Science and Technology of China***)

A THESIS SUBMITTED

FOR THE DEGREE OF DOCTOR OF PHILOSOPHY

DEPARTMENT OF MATERIALS SCIENCE AND

ENGINEERING

NATIONAL UNIVERSITY OF SINGAPORE

2008

Acknowledgements

I would like to express heartfelt gratitude to Professor Chow Gan Moog and Dr. Chen Jingsheng for their patient, insightful guidance and supervision on the project.

Thanks to Professor Jian-Ping Wang (University of Minnesota), for his guidance when I started my research.

I also feel grateful to the National University of Singapore, for providing me the scholarship for this research. I thank Data Storage Institute (DSI, Singapore), for providing the excellent research environment.

I acknowledge the help from Professor S. W. Han, Dr. Y. K. Hwu, Dr. C.J. Sun and Dr. J.O. Cross on the synchrotron experiments and data analysis.

I thank Mr. Dai Daoyang, and Dr. Liu Binghai for the help on TEM sample preparation and TEM operation.

I thank Dr. Yi Jiabao, Dr. Ding Yinfeng, Ms. Zou Yaying, Dr. Ren Hanbiao, Ms. Lu Meihua, and Mr. Lim Boon Chow for their friendship, discussion and help.

I also thank all those who have in one way or another contributed to the success of this thesis.

Finally, I especially thank my parents for their consistent encouragement and my wife, Ms. Ying Li, for her understanding and support.

Table of Contents

Abstract

With the demand on the areal density of magnetic recording media, $L1_0$ FePt alloy has attracted much attention because of its high magnetocrystalline anisotropy (7×10^7erg/cm^3), which allows magnetic grain of ~3 nm to be thermally stable. However, lower ordering temperature, lower magnetic exchange coupling, better control over film texture and read-write process on high-coercivity media are challenges to its application in magnetic recording media. In order to improve structural and magnetic performance, Ag was added into perpendicular FePt thin films by cosputtering and sequential sputtering. The microstructures, magnetic properties and phase miscibility of the FePt-Ag films were investigated. When cosputtered with Ag, FePt grain size and magnetic exchange coupling were reduced with increasing Ag content. A study on alloying of FePt-Ag by anomalous x-ray scattering (AXS) suggested that some Ag atoms resided in the FePt long-range order (LRO). Extended x-ray absorption fine structure (EXAFS) study indicated that most Ag atoms formed a separate phase from FePt. The small fraction of Ag atoms alloyed with FePt tended to replace Fe atoms. The coercivity of FePt films significantly increased when cosputtered with Ag. The coercivity enhancement was associated with the pinning effect of Ag and improvement in $L1_0$ ordering.

While Ag cosputtering changed the FePt thin films from perpendicular texture to longitudinal texture, sequential FePt/Ag/FePt deposition not only maintained the perpendicular texture but also improved the magnetic recording performance. Calculation of anisotropy constant (K_u) did not show ordering improvement in the sequential deposition. The improved coercivity was attributed to pinning effect and consequential

change in magnetic reversal mechanism. Investigation on the microstructure suggested that a nominal 3-nm Ag did not form a continuous layer structure between the FePt layers when the deposition temperature was 350 °C. Surface segregation of Ag confirmed Ag diffusion due to the low surface energy of Ag. Similar deposition at room temperature showed a continuous Ag layer between FePt layers.

The effects of Ag underlayer were investigated in terms of microstructure and magnetic properties. Ag underlayer enabled perpendicular texture because its lattice parameter is close to CrRu underlayer and FePt layer. A relatively larger lattice mismatch was favorable for strain-induced ordering. The result showed an optimized Ag thickness of 150 nm in terms of the perpendicular texture and exchange coupling for FePt media. In addition, the high thermal conductivity of Ag would be favorable to dissipate the heat generated in heat-assisted magnetic recording (HAMR).

List of Tables

List of Figures

List of Symbols and Abbreviations

AFM	Atomic Force Microscope
AGFM	Alternation Gradient Force Magnetometer
APS	Advanced Photon Source
AXS	Anomalous X-Ray Scattering
bcc	Body-centered Cubic
BE	Binding Energy
BF	Bright Field
DF	Dark Field
DSI	Data Storage Institute
DWF	Debye-Waller Factor
ESCA	Electron Spectroscopy for Chemical Analysis
EXAFS	Extended x-ray Absorption Fine Structure
fcc	Face-centered Cubic
fct	Face-centered Tetragonal
FT	Fourier Transform
FWHM	Full Width at Half Maximum
GMR	Giant Magneto Resistive
HAMR	Heat Assisted Magnetic Recording
h	Planck Constant
H_c	Coercive Field
$H_{c\perp}$	Perpendicular Coercivity

$H_{c//}$	In-plane Coercivity
H_d	Demagnetization Field
HF	High Frequency
H_k	Anisotropy Field
HRTEM	High-resolution Transmission Electron Microscopy
IMFP	In Elastic Mean Free Path
kfci	kilo Flux Charge per Inch
k_B	Boltzmann Constant
K_u	Magnetic Anisotropy Energy
$L1_0$	(Cu-Au I) Structure
LMR	Longitudinal Magnetic Recording
LRO	Long-Range Order
MBE	Molecular Beam Epitaxy
MFM	Magnetic Force Microscope
MR	Magnetoresistive
M_s	Saturation Magnetization
PMR	Perpendicular Magnetic Recording
Q_{vac}	Activation Energy for Vacancy formation
q_z	Momentum Transfer
RBS	Rutherford Back Scattering
RMS	Root Mean Square
S	Squareness
SAD	Selected Area Diffraction

SNR	Signal-to-Noise Ratio
SR	Synchrotron Radiation
SRO	Short-Range Order
UHV	Ultra-High-Vacuum
ν	Frequency
VSM	Vibrating Sample Magnetometer
XAFS	X-ray Absorption Fine Structure
XANES	X-ray Absorption Near-Edge Structure
XAS	X-ray Absorption Spectroscopy
XPS	X-ray Photoelectron Spectroscopy
XRD	X-Ray Diffraction Spectroscopy
X_{vac}	Vacancy Concentration

Chapter 1. Introduction

1.1 Background

In this information age, the demand for high performance, low cost and stable information storage systems is ever increasing. In the past 100 years, magnetic recording probably has represented the most rapidly developing area of high technology in the world, which has changed the way we live, work, learn and play. When IBM introduced the first hard disk drive in 1957, the areal density was only 2 kbit/in^2. It has increased at an astonishing rate over the last three decades. The density growth rates were 30% per year for 1970-1990 and 60% per year since 1990.[1] The significant improvement came in 1992 with the introduction of smoother sputter-deposited thin film media to replace the binder-based particulate media as well as the magnetoresistive (MR) head and giant magneto resistive (GMR) head playback transducers. After the demonstration at 20 Gbits/in^2 in 1999, the areal densities achieved in commercial products have grown at a rate approaching 100% per year.[2] However, from the viewpoint of physics, there will be a limit in the future to which the ultimate areal density can be achieved by conventional longitudinal magnetic recording (LMR). To extend this limit, perpendicular magnetic recording (PMR)[3,4] and patterned media[5,6] have been proposed.

The configuration of PMR theoretically promises several key advantages over LMR. In high density PMR, magnetization of adjacent bit aligned oppositely, resulting in low demagnetization field (H_d). In addition, the writing field can be much higher due to the pole-head/soft-underlayer configuration, which allows the use of media with high coercivity and high anisotropy energy density and in turn enhances the resistance to

thermal fluctuation. Moreover, sharp transitions on relatively thick media allow more grains to be included per unit area for a given grain volume. Strong uniaxial orientation of the perpendicular media leads to a tight switching-field distribution, sharper written transition and higher signals and lower noise.

It is considered that PMR might allow higher recording densities than LMR by about a factor of three to five. A high recording density of about 520 Gbit/in^2 on Co-based alloy perpendicular media has been demonstrated by Western Digital recently.[7] Simulation has shown that perpendicular recording density can exceed 1Tbits/inch^2.[8]

Because signal-to-noise ratio (SNR) is proportional to the number of grains per bit, when bit size becomes smaller and smaller, media grain size must be reduced to maintain a near constant number of grains per bit in order to satisfy the SNR requirements. The reduced bit cell volume and small grain size raise the issue of thermal instability of magnetization for each bit. This effect, referred to as superparamagnetism, will ultimately limit the achievable areal density for a given media material. The equation, $\Delta E = K_u V$, represents the energy barrier for magnetization reversal (Fig. 1-1), where K_u and V are anisotropy constant and magnetic switching volume, respectively. When switching volume is small, thermal fluctuation $k_B T$ (k_B and T are Boltzmann constant and absolute temperature, respectively) become comparable with the energy barrier. Magnetization has a higher probability to switch its direction.

The thermal relaxation time τ can be expressed by the exponential function.[9]

$$\tau = 10^{-9} \exp(\frac{K_u V}{k_B T}) \qquad \textbf{(1-1)}$$

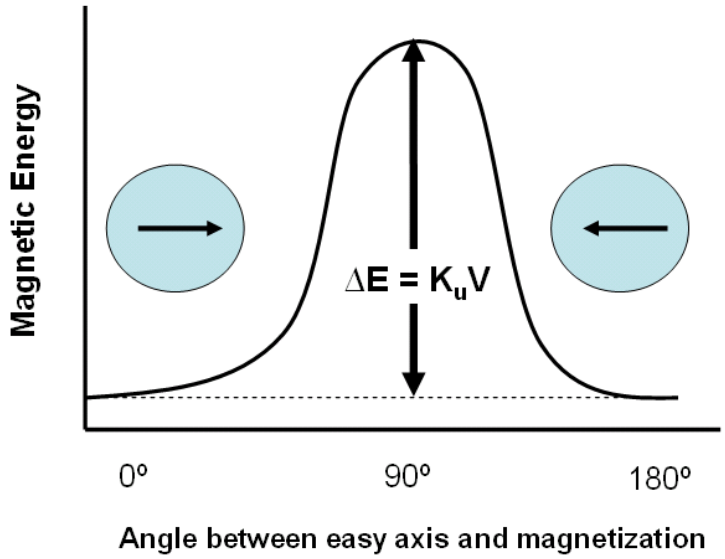

Figure 1-1 Schematic diagram of energy barrier for magnetization reversal

The typical criterion for disk stability is that each bit must maintain 95% of its magnetization over ten years, which requires a significant energy barrier $\Delta E > 60\ k_B T$.

Co-based media is commonly used in current PMR. However, the intrinsic properties of Co alloy media with relatively low anisotropy cannot support much higher areal density. To overcome the superparamagnetic limit, materials with high K_u are desirable. Among them, FePt alloy is a possible candidate.

1.2 Application of FePt alloy as recording media

The properties of FePt alloy were first studied in 1907.[10] A transformation between ordered and disordered phases was observed in the equiatomic composition range, which was confirmed by measurements of X-ray spectra,[11,12] magnetic,[13,14] electrical[13,15] and mechanical[16] properties. Kussman and Rittberg found that three stable crystal structures existed in Fe-Pt system: $FePt_3$, FePt, Fe_3Pt (Appendix 1). The phases and properties of these alloys have been documented by Hansen and Bozorth.[17]

The magnetic properties of FePt alloys have been studied since the 1930's. Fallot determined that equiatomic alloy was a ferromagnet with a Curie temperature of 670K.[18] Kussman and Rittberg found that the saturation magnetization was greater for the disordered alloy than that for the ordered alloy.[13] The FePt $L1_0$ alloy uniaxial magnetocrystalline anisotropy constant K_u was measured as 7.0×10^6 J/m^3 for bulk alloy.[19,20] A similar value, $K_u = 6\times10^6$ J/m^3, was measured for thin film.[21] In comparison, the disordered alloy has cubic anisotropy and $K_u = 6\times10^3$ J/m^3.[22] The ordered alloy has a saturation magnetization at 298K of 1150G.[21] The critical diameter for a single domain FePt particle is around 300 nm.[22] The thickness of a domain wall in the FePt bulk alloy is around 3.9 nm.[23]

1.2.1 Advantages of FePt

Table 1-1 Magnetic properties of $L1_0$ FePt alloy and other ferromagnetic materials

Material	K_u (10^7 erg/cm^3)	M_s (emu/cm^3)	H_k (kOe)	T_c (K)	δ_B (Å)	γ (erg/cm^3)	D_c (μm)	D_p (nm)
CoPtCr	0.2	298	13.7	--	222	5.7	0.89	10.4
Co	0.45	1400	6.4	1404	148	8.5	0.06	8.0
Co_3Pt	2.0	1100	36	--	70	18	0.21	4.8
FePd	1.8	1100	33	760	75	17	0.20	5.0
FePt	6.6-10	1140	116	750	39	32	0.34	3.3-2.8
CoPt	4.9	800	123	840	45	28	0.61	3.6
MnAl	1.7	560	69	650	77	16	0.71	5.1
$Fe_{14}Nd_2B$	4.6	1270	73	585	46	27	0.23	3.7
$SmCo_3$	11-20	910	240-400	1000	22-30	42-57	0.71-0.96	2.7-2.2

- **Anisotropy field: $H_k = 2K_u/M_s$**
- **Domain wall width: $\delta_B = \pi(A/K_u)^{1/2}$**
- **Single particle domain size: $D_c = 1.4\,\delta_B / M_s^2$**
- **Exchange coupling constant: $A = 10^{-6}$ erg/cm**
- **Minimal stable grain size: $D_p = (60k_BT/K_u)^{1/3}$ (τ = 10 years)**

High anisotropy constant, large M_s and high corrosion resistance make FePt a possible candidate for future high-density media. Table 1-1 compares the magnetic

properties of FePt $L1_0$ alloy with other ferromagnetic materials.[24] It is noted that the anisotropy constant of $L1_0$ FePt alloy is an order of magnitude higher than that of currently used CoPtCr material. The high K_u allows for thermally stable grain size to be as small as ~3 nm.[25]

1.2.2 Challenges and solutions for FePt application

In spite of the advantages of FePt alloy, some challenges to its application as magnetic recording media remain. Following aspects are main challenges:

1.2.2.1 Lower ordering temperature

Long-range order has critical effects on the magnetic properties of FePt films. FePt alloy prepared by sputtering below 550 ^{o}C is disordered face-centered cubic (*fcc*) phase (Fig. 1-2(a)), which is magnetically soft with coercivity value less than 20 Oe.[26] In FePt $L1_0$ phase, Fe and Pt atoms form superlattice tetragonal structure ($c < a$), where Fe and Pt layers stack alternatively and give rise to a magnetic easy axis along the *c* direction (Fig. 1-2(b)). For application as recording media, the transition from *fcc* ($c = a$) to the ordered $L1_0$ phase ($c < a$) is essential.

Lower ordering temperature for $L1_0$ phase transformation is desired for practical applications, especially for depositing the media on glass substrate. Usually, a heated substrate or a post-deposition thermal annealing is needed to achieve the ordered structure. One of the adverse effects of thermal treatment is the grain growth. Several methods were developed to decrease ordering temperature: (1) promotion of $L1_0$ ordering by elemental doping. For example, It was reported that Cu significantly reduced the ordering temperature;[27,28,39] (2) Strain or stress induced $L1_0$ ordering and.

i.e. optimized lattice mismatch is favorable for $L1_0$ ordering; (3) Other ordering, such as irradiation induced ordering.

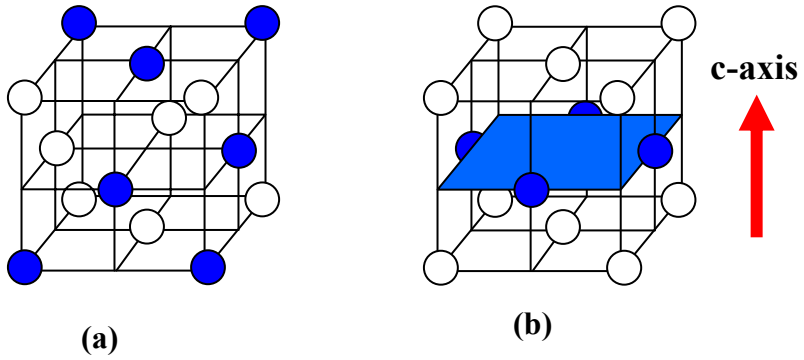

Figure 1-2 Schematic figure for (a) disordered FePt alloy and (b) $L1_0$ ordered FePt superlattice structure

1.2.2.2 Reduction of grain size and exchange coupling for SNR requirement

Nanocomposite structure, where FePt grains were embedded in nonmagnetic matrix, can also alleviate the grain growth. The surrounding material will suppress the grain growth during thermal treatment. It was reported that SiO_2,[29] Cr,[30] Si_3N_4,[31] BN,[32] AlN,[33] B_2O_3,[34] C,[35] W, Ti,[36] Zr,[37] Ag,[38-40] and Au[40] had restraining effects on FePt grain size and led to magnetic decoupling of FePt grains. Preparation methods, such as cosputtering, laser ablation and annealing of multilayers have been attempted to fabricate granular thin films.

1.2.2.3 Better control of the magnetic easy axis alignment

In $L1_0$ phase FePt crystal, magnetic easy axis is parallel to the shorter *c* axis. FePt film with FePt(001) texture has an out-of-plane magnetic easy axis, whereas an in-plane easy axis exists for FePt(200) textured film. FePt thin films deposited by magnetron sputtering tend to develop a (111) texture, placing the easy axis of most grains at an angle of 36^o above the film plane.[41] This can be explained in terms of surface energy minimization, because (111) plane is the close-packed plane in *fcc*

structure. For recording application, however, it is necessary to align the magnetic easy axis either parallel with or perpendicular to film plane depending on the recording mode used.

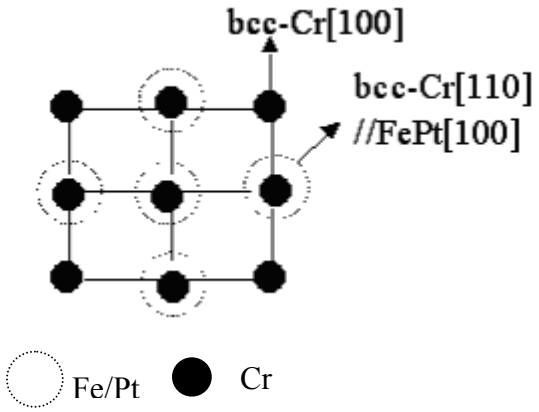

Figure 1-3 Schematic diagram of the lattice relationship between Cr underlayer and perpendicular-textured FePt thin film

To realize the advantages of perpendicular recording mode, much effort has been made to fabricate FePt thin films with perpendicular texture. Perpendicular-orientated $L1_0$ FePt thin films were achieved by several methods, such as: molecular beam epitaxial (MBE) growth on MgO single crystal substrates, e-beam evaporation, Cr(100) underlayer/MgO/glass, non-epitaxial growth (post-annealing FePt/C or FePt/B_2O_3) and sputtering FePt/Ag/Mn_3Si/Ag on heated Si(001) substrate[42] (300 ^oC), etc. However, the above methods are not practical for application due to high cost, high roughness and high temperature required.

Another method is to use Cr underlayer to induce perpendicular FePt texture. The schematic diagram of the lattice relationship is shown in Fig. 1-3. In *bcc* Cr, the (110) plane is the close-packed plane with the highest atomic density. Hence, Cr(110) texture can be expected in the equilibrium Cr thin films deposited at room temperature. However, by adjusting the deposition parameters, such as deposition

temperature, deposition rate, etc. Cr(002) texture can be achieved at optimized conditions. In this case, the in-plane Cr(110) spacing is close to FePt(100). Therefore, FePt [100] would lie in the film plane by matching Cr [110]. The in-plane FePt [100] means the perpendicular FePt(001) and (002) texture. The lattice relationship is schematically shown in Fig. 1-3. In addition, the Cr(110) spacing is 5.8% higher than that of FePt(100). This mismatch may cause the expansion of the in-plane FePt(100) axes. Generally, the unit cell volume would keep constant because a high energy is required to change it. Assuming a constant unit cell volume, shrinkage of perpendicular FePt(001) axis can be expected (c<a). Note that $L1_0$ FePt phase is characteristic of a shorter *c* axis, which refers to the magnetic easy axis, a slightly higher lattice mismatch between Cr(110) and FePt(100) may aid the transformation from *fcc* phase to $L1_0$ phase. By adding Ru into Cr thin films, the lattice mismatch can be further controlled, because the atomic radius of Ru is bigger than that of Cr. Higher Ru concentration can result in a larger lattice parameter of CrRu alloy according to the Vergard's law. Previous work showed that 10 at.% Ru optimized the mismatch.[43] With in-situ annealing, perpendicular FePt(001) texture with rocking curve full width at half maximum (FWHM) of 4 ° and good $L1_0$ ordering were obtained at a relatively lower temperature of 350 °C, whereas temperature over 550 °C was generally required in the thermal treatment in order to achieve good $L1_0$ ordering. This means that a reduction of ordering temperature by 200 °C of FePt was achieved with the use of CrRu underlayer.

1.3 Objectives

Some reports have shown promising effects of Ag on FePt thin films and CoPt nanoparticles, such as size restraining and lower ordering temperature[38]. However, there has been a lack of systematic study and better understanding on FePt-Ag system. Current work attempted to study the effects of Ag on properties of FePt thin films. Granular structure by cosputtering and layered structure were studied. The selection of Ag was based on following considerations:

- It was reported that Ag had the restraining effect on FePt grain size and led to decoupling of FePt grains,[38] that is favorable for the application in high-density media.
- In bulk Fe-Ag binary phase diagram, the miscibility of Ag in Fe is very low (<0.02 at.%). According to the parameters listed in Table 1-2, the big size of Ag atom is unfavorable for interstitial alloy. Therefore, granular structure with separate Ag phase is possible, which is favorable to suppress the FePt grain growth and reduce the exchange coupling between FePt grains.

Table 1-2 Elemental parameters of Fe, Pt and Ag

Element	Atomic Radius (nm)	Crystal Structure	Electronegtivity
Fe	0.124	*bcc*	1.83
Pt	0.138	*fcc*	2.28
Ag	0.144	*fcc*	1.93

The objectives of this project include:

- Effects of Ag on structure and magnetic properties of the cosputtered FePt-Ag thin films, including texture, grain size, $L1_0$ ordering, coercivity, exchange coupling and recording performance.

- Correlation between the microstructure and magnetic properties in cosputtered FePt-Ag thin films.
- Sequential deposition of FePt/Ag/FePt thin films to achieve both perpendicular texture and property improvement.
- Effects of Ag underlayer on microstructure and magnetic properties of FePt thin films for ordering improvement.

1.4 Organization of the thesis

In this chapter, the advantages and challenges of FePt alloy for high-density recording media application are reviewed. The scope and objectives of this thesis are introduced.

Chapter 2 introduces the experimental details for the preparation, characterization and analysis of the samples used in this study. In Chapter 3, the study of structural and magnetic properties of the composite FePt-Ag with various Ag concentrations is presented. The correlation between microstructure and magnetic properties is discussed. In Chapter 4, the alloying and local atomic environment of composite FePt-Ag system are investigated by means of AXS and EXAFS techniques. In Chapter 5, the effects of sandwich structured FePt-Ag film on crystallographic structure, microstructure, magnetic properties and recording performance are presented. In Chapter 6, the effects of Ag underlayer on the magnetic properties and crystallographic structure are discussed. The main achievements of this research are summarized in Chapter 7.

Chapter 2. Experimental Techniques

In order to study magnetic and structural properties of FePt-Ag thin films, the first step is to fabricate the materials. Characterization of the thin films provided information about structural and magnetic information of FePt-Ag thin films.

In this chapter, an overview is given on the selected experimental techniques used in this study, mainly focusing on sputtering and relevant characterization methods used to characterize the structural and magnetic properties of thin films.

2.1 Sample preparation

The samples were fabricated by magnetron sputtering, which is widely used in industry production due to the high deposition rate and easy control. Even refractory metal can be easily deposited by sputtering. The relevant concepts, working principle and critical parameters of sputtering technique are introduced below.

2.1.1 Plasma and Sputtering

Plasma is a fluid of a mixture of electrons and positive ions in a quasi-neutral electrical state. Generally, positive ions are generated by collisions between mobile electrons and uncharged particles. The electrons in plasma are highly energetic, especially compared to the larger ions (normally argon for sputtering).

By applying a high voltage across a low-pressure gas, such as Ar, “plasma”, an electrically approximately neutral association, which consists of electrons and gas ions in

a high-energy state, is created. The plasma allows the Ar^+ ions to hit the target with high kinetic energies.

Sputtering has been used to fabricate various kinds of microelectronic devices and systems in many different industries.[44] It is one of the most important methods in preparing the media and head thin films for magnetic recording purpose.[45, 46] In this research work, all the films were prepared by the sputtering deposition method. The significant advantages of the sputtering deposition method, compared with other physical deposition methods, are high yielding rates, good adhesion and controllability of structural and magnetic properties of the films.[47]

The sputtering process is accomplished by applying a certain voltage of potential across the paralleled electrodes, which is bonded with a metal target and a selected substrate in a vacuum chamber that contains a sputtering gas. A glow discharge (also called plasma) is then ignited and maintained, where the sputtering gas particles continuously collide with the metal targets and generate the sputtered particles, which are later deposited on the substrate.

In sputtering deposition, the target (the material that is to be deposited) is placed in a vacuumed chamber. Atoms or molecules are removed from a target using energetic ion bombardment.

By applying a high radio frequency or direct current voltage on the target, energetic electrons are emitted from the target form ions using a process gas, normally Ar. Under these conditions, plasma is formed. This applied electric field accelerates Ar^+ ions onto the target with high kinetic energies of up to several hundred eV. This has

comparably much higher energy than the fraction of one eV that is involved in thermal evaporation.

The Ar^+ ions then collide with the target. Some of the secondary collisions in the target near to the surface cause target atoms to be knocked off the target and this is known as 'sputtering'. Between target and substrate, each ejected atom has numerous gas phase collisions with the process gas, which lowers its energy. Hence, optimizing the distance between target and substrate and rotating the substrate continuously allow uniform deposition of the film.

Magnetron sputtering using magnets offers more advantages than normal sputtering. The electrons are forced to spiral near the target surface when magnets are placed behind the target. This technique has many benefits. Firstly, the mean free path length of electrons in the magnetron is increased and thus its ionization probability is raised. Secondly, electrons contained by the magnetic fields are less likely to escape and bombard the substrate. The localized plasma confines the Ar^+ ions to a volume near the target surface and keeps their impact energy high. This will maximize the sputtering rate and hence in turn maximize the deposition rate.

Sequential sputtering is commonly used to fabricate multilayer thin films. Different layers are deposited by sputtering from individual targets one after another. The deposition rate and film thickness are controlled by the power and sputtering duration. Cosputtering is useful to deposit different materials with various compositions. During cosputtering, the sputtering targets with different compositions are sputtered simultaneously, giving the desirable compositions from different targets. The relative composition of individual materials in the thin film can be changed by adjusting the

sputtering power for the targets. In this project, the home-made Ultra-High-Vacuum (UHV) sputtering system had 4 targets installed in the main chamber with same distance from the substrate. The system is capable for both sequential and cosputtering, depending on the sample design.

2.2 Structure Characterization

2.2.1 X-Ray Diffraction (XRD)

The basic principle of x-ray diffraction is the Bragg's Law, which is given by:[48]

$$n\lambda = 2d_{hkl}\sin\theta_{hkl} \qquad \textbf{(2-1)}$$

where λ is the wavelength of the x-ray source, d is the lattice spacing of the diffracting planes, θ is the angle between the x-ray beam and the diffraction planes, and n is an integer index. The strong diffraction intensity will occur when the outgoing waves add up in phase.

When grain size is taken into consideration, the destructive interference results in the broadening of diffraction curve. The width of the diffraction curve increases as the thickness of the crystal decreases. The line broadening can be expressed by Scherrer's formula:

$$t = \frac{0.9\lambda}{BCos\theta} \qquad \textbf{(2-2)}$$

where B is the full-width at half maximum (FWHM) of the diffraction curve. t is the crystal thickness. The formula is used to estimate the size of very small crystal from the measured width of the diffraction curves.

Unlike single crystal, alignment of lattice in polycrystalline materials is random. The distribution of lattice alignment results in the width broadening of diffraction peaks. By fixing the θ-2θ angles and rotating the sample in Ω, ψ and χ directions, respectively, the rocking curve for particular diffraction peak can be obtained with high-resolution x-ray diffraction (HR-XRD). The peak width of rocking curve is an indicator of texture quality. Large FWHM means wide orientation distribution. The geometry of HR-XRD is shown in Fig. 2-1.

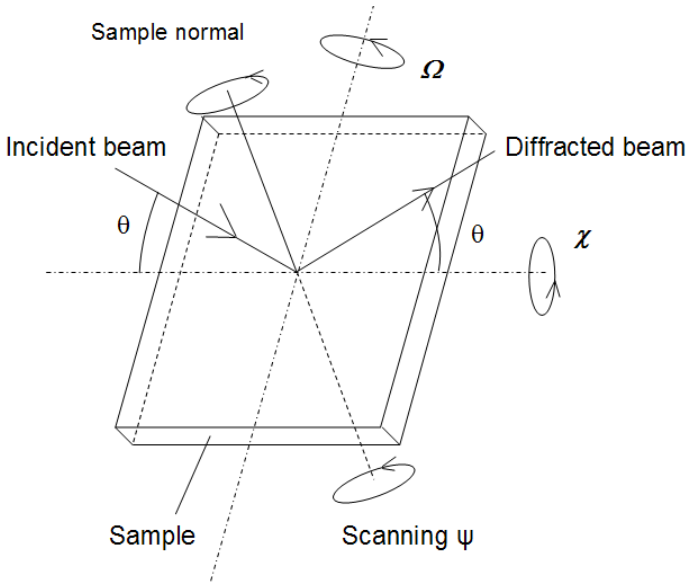

Figure 2-1 Schematic diagram for HR-XRD geometry

2.2.2 Transmission Electron Microscopy (TEM)

TEM works on the same fundamental principles as the light microscope. What is different is TEM uses electrons instead of light. A light microscope is limited by the wavelength of light. TEM uses electrons as the "light source". Therefore with their much shorter wavelength, it is possible to get a resolution a thousand times better than with a light microscope.

Basically, TEM can be used to study the microstructure (size, shape and arrangement) of the particles that make up the specimen as well as their relationship to each other on the scale of atomic diameters. TEM can also be used to give the crystallographic information in the specimen and the degree of order, detection of atomic-scale defects in areas a few nanometers in diameter. The working principles of TEM are briefly introduced below.

Firstly, the electron gun produces a stream of electrons. This stream is focused into a small and thin coherent beam with the two condenser lenses. The coherent beam is then restricted by the condenser aperture. The condenser aperture knocks out high angle electrons.

Next, the beam arrives at the specimen and parts of the beam are transmitted. The objective lens focuses the transmitted beam into an image. After that, the objective aperture and selected area aperture further restrict the beam knocking out high angle diffracted electrons. The image is then enlarged as it passes through both the intermediate and projector lenses.

Lastly, the image reaches the main screen, which allowing the image to be seen by the user. The lighter regions of the image represent thinner or less dense parts of the sample where more electrons are transmitted while the darker regions represent denser or thicker parts of the sample where fewer electrons are transmitted.

To obtain lattice images, a larger objective aperture must be selected, which allows many beams including the direct beam to pass. The image is formed by the interference of the diffracted beams with the direct beam (phase contrast). If the point resolution of the microscope is sufficiently high and a suitable sample oriented along a

zone axis, then high-resolution TEM (HRTEM) images are obtained. In many cases, the atomic structure of the specimen can directly be investigated by HRTEM. In the bright field (BF) mode of TEM, mass-thickness and diffraction contrast contribute to image formation: thick areas, areas in which heavy atoms are enriched, and crystalline areas appear with dark contrast. In spite of the useful information obtainable from BF images, it should be mentioned that the interpretation of contrast is often impeded since these phenomena occur simultaneously. In the dark field (DF) mode of the TEM, the diffracted beam has interacted strongly with the specimen, and often very useful information is presented in DF images, e.g., that about planar defects, stacking faults or particle size.

One of the powerful features of TEM is its ability to display diffraction patterns of the sample. In this case, the wave like nature of electrons is utilized to diffract the incident beam from the atomic structure within the sample. Electron diffraction (ED) is a collective elastic scattering phenomenon with electrons being scattered by atoms in a regular array (crystal). The incoming plane electron wave interacts with the atoms, and secondary waves are generated, which interfere with each other (analogous to the Huygens principle for diffraction of light). This occurs either constructively (reinforcement at certain scattering angles generating diffracted beams) or destructively (extinguishing of beams). As in XRD, inter-planar distances can be calculated from ED patterns based on Bragg law. This can provide information on the crystal structure within the sample and is particularly useful when the atomic arrangement is regular and periodic, as in a crystal. Furthermore, information about crystal symmetry can be obtained. Consequently, electron diffraction represents a valuable tool in crystallography.

TEM was used to measure the size and shape of the microstructure constituents of the material. In this research, the TEM specimens were prepared using traditional method: by mechanical lapping and dimpling followed by the ion milling.

2.2.3 X-Ray Photoelectron Spectroscopy (XPS)

In XPS, photo-ionization and energy-dispersive analysis of the emitted photoelectrons are used to study the composition and electronic state of the surface region of a sample.

XPS is based on the process of electron excitation by photon. The energy of a photon is given by the Einstein relation:

$$E = h\nu \qquad \textbf{(2-3)}$$

where h is the Planck constant (6.62×10^{-34}Js) and ν is the frequency of the radiation (Hz). In this project, XPS with an Al-K_α (1486.55 eV) source was used.

The binding energy (BE) is assumed to be the energy that is required to emit the electron from its core level to the vacuum level. Therefore the kinetic energy of the photoelectron is equal to the energy of the photon minus the binding energy:

$$KE = h\nu - BE \qquad \textbf{(2-4)}$$

In XPS, the photon is absorbed by an atom in a molecule or solid, leading to ionization and the emission of a core (inner shell) electron. The kinetic energy distribution of the emitted photoelectrons (i.e. the number of emitted photoelectrons as a function of their kinetic energy) can be measured by means of any appropriate electron energy analyzer and a photoelectron spectrum can thus be recorded.

Each element will give rise to a characteristic set of peaks in the photoelectron spectrum at kinetic energies determined by the photon energy and the respective binding energies. The presence of peaks at particular energies therefore indicates the presence of a specific element in the sample under study - furthermore, the intensity of the peaks is related to the concentration of the element within the sampled region. Thus, the technique provides a quantitative analysis of the surface composition and is sometimes known by the alternative acronym, ESCA (Electron Spectroscopy for Chemical Analysis).

The exact binding energy of an electron depends not only upon the level from which photoemission is occurring, but also upon:

- The formal oxidation state of the atom
- The local chemical and physical environment

XPS is a sensitive technique for investigating the elemental composition and the associated chemical bonding states. Relative atomic concentration percentages can be determined with a sensitivity of 0.1 to 1 at.% for Li and heavier elements.

The Inelastic Mean Free Path (IMFP) is a measure of the average distance traveled by an electron through a solid before it is inelastically scattered; it is dependent upon the initial kinetic energy of the electron and the nature of the solid (but most elements show very similar IMFP vs energy relationships).

The IMFP is actually defined by the following equation which gives the probability of the electron traveling a distance, d , through the solid without undergoing scattering

$$P(d) = \exp (- d / l) \qquad \textbf{(2-5)}$$

where l is the IMFP for the electrons of energy E. From Eq. 2-5, the probability of escape decays very rapidly and is essentially zero for a distance $d > 5l$. Therefore, information by XPS is typically obtained for the near-surface region within ~30 Å of the outer surface.

By sputtering on sample with ion beam, a crater can be formed. The obtained spectra provide interior information of the sample. Sequential sputtering and spectra acquisition can reveal the depth profile of elemental composition. The depth resolution can be improved with grazing angle. With 45º incident angle and Al K-α source, the depth resolution is about 3 nm. For layer thickness less than the depth resolution, the sputtering step size should be set no more than half of the depth resolution to ensure that the information of thinner layer is not missed. In our depth profile study, the sputtering step size is 1/3 of the thinnest nominal thickness in the multilayer samples.

2.2.4 Extended X-Ray Absorption Fine Structure (EXAFS)

During the last 15 years, x-ray absorption spectroscopy (XAS) has been applied extensively to determine the local atomic and electronic structure of the absorbing centers (atoms) in the materials science, physics, chemistry, biology, and geophysics.

When x-rays of energies close to the electron binding energies are absorbed, features known as absorption edges are observed. The typical x-ray absorption spectrum for the nickel *K* edge in a sputtered Ni thin film is shown in Fig. 2-2. It exhibits an oscillating fine structure, which extends far from the absorption edge. For convenient interpretation, two regions are often separated: (i) the x-ray absorption near-edge structure (XANES), and (ii) the extended x-ray absorption fine structure (EXAFS).

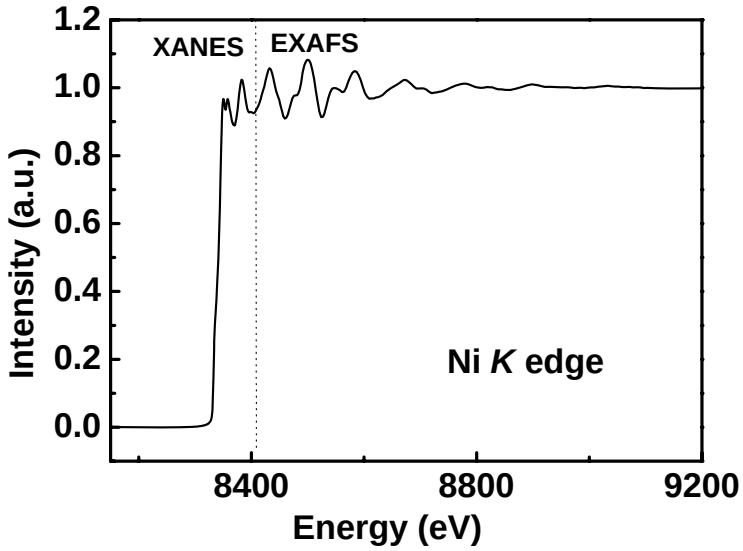

Figure 2-2 Example EXAFS spectrum of Ni thin film

It is agreed that the XANES region extends for 50-100 eV beyond an absorption edge and is determined by the local density of vacant states in an absorbing atom, as well as by multiple-scattering effects, i.e., scattering of an excited photoelectron on several atoms. The farther EXAFS region is dominated by the single scattering processes and extends up to 400-2000 eV from an edge. Its upper bound is determined by the signal-to-noise ratio and/or another absorption edge. Note that this division of an x-ray absorption spectrum into two regions is conventional and the intervals of these regions can vary for various compounds. For this reason, the term x-ray absorption fine structure (XAFS) is now often used for the whole oscillating component beyond an absorption edge.

The fine structure beyond an absorption edge was first observed about 70 years ago.[49- 55] However, it took more than 40 years to interpret this phenomenon. In 1931, Kronig[56] was the first who attempted to explain XAFS by the long-range order in a system. Later, this mechanism broke down. One year later, Kronig[57] proposed another theory, which was based on the substantial importance of short-range order and attributed

XAFS to the modulation of the final-state wave function of a photoelectron scattered on the neighboring atoms. This approach was later further developed[58-62] and provides the basis of the current concept of the XAFS.

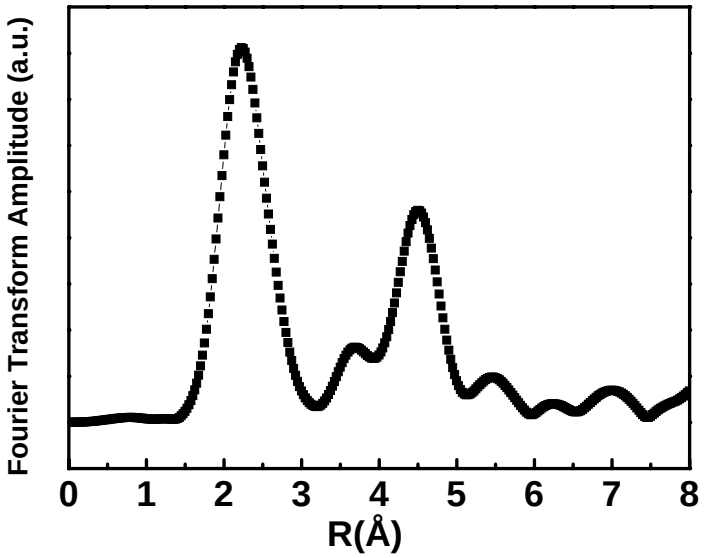

Figure 2-3 Fourier transform amplitude of Fe foil standard

The fundamental development in x-ray absorption spectroscopy occurred in the early 1970s, when Sayers, Stern, and Lytle[63] demonstrated that the Fourier transform of the EXAFS oscillations gives a pattern close to the radial atomic density distribution. This circumstance testified to the crystallographic origin of information contained in the EXAFS oscillations. Fourier transform spectrum for the Fe foil standard is shown in Fig. 2-3.

Moreover, the spectroscopic measurements in the XANES region with soft x-rays from 300 eV to 10 keV were shown to provide information on vacant states near the Fermi level with high energy resolution.[64,65] The use of synchrotron radiation (SR) as a source of a continuous spectrum significantly stimulated the development of EXAFS spectroscopy and its various applications. The SR sources are many orders of magnitude

brighter than x-ray tubes and ensure quick (as short as several milliseconds) EXAFS-spectrum measurement for low densities of an element.[66]

The excited photoelectron can be described by outwardly propagating spherical wave function, which is scattered by the surrounding atoms. The interference between the outgoing wave and the backscattered waves is the source of the oscillatory structure in EXAFS. The interference process is schematically shown in Fig. 2-4.

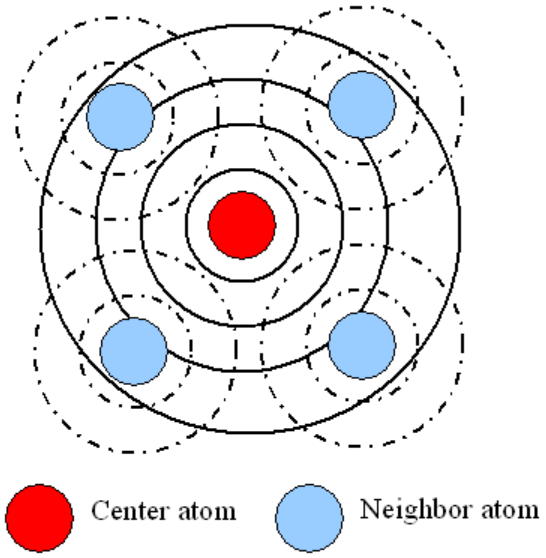

Figure 2-4 Schematic diagram of the radial portion of the photoelectron wave (solid lines) being backscattered by the neighboring atoms (dotted lines)

The backscattering amplitude and phase differences are determined by the type of the absorbing and scattering atoms, the interatomic distance and the electron wave number *k*. In single scattering approximation the theoretical EXAFS signal is given by the well-known formula:[67]

$$\chi(k) = \sum_i \frac{N_i S_0^{\,2}}{kR_i^{\,2}} \left| f_i(k, R_i) \right| \exp(-2R_i / \lambda) \exp(-2k^2\delta^2) \sin\left[2kR_i + \delta_i(k)\right] \qquad \textbf{(2-6)}$$

Here N_i is the equivalent number of neighboring atoms, at a distance R_i. S_0^2 is an empirical amplitude correction factor parameter taking into account of many-body losses in the photo absorption process (also called passive electron reduction factor), $f_i(k,R_i)$ is the backscattering amplitude, λ is the photoelectron mean free path, and δ^2 is the correlated Debye-Waller factor (DWF) of the absorber-scatterer pairs, E_0 is the photoelectron energy origin and $\delta_i(k)$ is the phase shifts.

The above parameters can be either fixed or allowed to vary when an experimental EXAFS spectrum is fitted. Therefore, the atomic local environment information, e.g. the coordination number and distance, can be resolved from the EXAFS data analysis.

XAS can provide information that substantially complements the results of other experimental methods, such as the diffraction (scattering) of x-rays and neutrons, photoelectron, and emission x-ray spectroscopy. The basic XAS advantages are (i) selectivity in the chemical-element type (in some cases, also in the location of an element in a material), which enables one to acquire information on pair and multiatomic distribution functions for the local environment of each element in the material under investigation; (ii) sensitivity to the partial densities of vacant states near the Fermi level; (iii) high density sensitivity (10–100 particles per mole) and relatively short times (from milliseconds to tens of minutes) of detecting experimental spectra when the synchrotron radiation is used; and (iv) a small required sample volume (usually, an amount less than 30 mg/cm^2 is enough). Due to these advantages, the employment of XAS is especially attractive for studying crystalline and disordered (amorphous, glassy, liquid, and gaseous)

multicomponent materials, as well as for carrying out *in situ* investigations of dynamical processes (phase transitions and chemical reactions).

2.2.5 Anomalous X-Ray Scattering (AXS)

XRD is widely used for both qualitative and quantitative analysis of various materials. However, in a multi-component mixture with a relatively complicated chemical composition, the identification of the individual chemical constituents cannot be obtained by the conventional x-ray powder diffraction method. There are also generally insufficient differences in the x-ray diffraction peak intensities for two elements of nearly the same atomic number in the periodic table. For example, it has been recently shown in an AXS study of nanostructured Ni-Co films that the appearance of a single XRD peak alone is not sufficient evidence to determine if a solid solution has formed.[68]

AXS is an alternative to overcome the problem due to its elemental sensitivity arising from the so-called "anomalous dispersion effect" near the absorption edge or remarkable variation in the crystallographic structure factors.[48]

In conventional XRD, the energy of incident x-rays is chosen to be away from the absorption edge of the constituent elements, and the energy independence is then well accepted for the so-called atomic scattering factor, $f(q)$, given by simple potential scattering theory. When the energy of the incident x-ray beam is close to the absorption edges of the constituent elements, the scattering factor depends not only on the wave vector but also on the incident x-ray energy. $f(q)$ becomes complex and can be expressed in the following form:

$$f(q,E) = f^{0}(q) + [f'(E) + if''(E)] \qquad \textbf{(2-7)}$$

where q is wave vector, E is the incident x-ray energy. $f^{o}(q)$ corresponds to the normal atomic scattering factor given by the Fourier transform of the electron density in an atom. $f'(E)$ and $if''(E)$ are the real and imaginary components of the so-called anomalous dispersion term, which arising from anomalous (resonance) scattering depend upon the incident x-ray energy. $f'(E)$ and $f''(E)$ can be correlated each other by the Kramers-Kronig relation:

$$f'(\omega) = \frac{2}{\pi}\int_0^{\infty} \frac{f''(\omega')\partial\omega'}{\omega^2 - \omega'^2} \qquad \textbf{(2-8)}$$

where ω=E/ħ is the angular frequency.

The variation of $f'(E)$ and $f''(E)$ as a function of energy is illustrated below using the *K*-absorption edge of a Co atom as an example:

The real part $f'(E)$ significantly decreases at the absorption edge and forms a sharp negative peak with a typical FWHM of 50 eV. It is also noted that $f'(E)$ almost keep constant when the energy is far away from the absorption edge.

During AXS measurement, $f^{o}(q)$ is fixed by fixing the momentum transfer (q). The diffraction intensity is monitored as the x-ray energy is scanned through the relevant absorption edge. If an element in question is associated with the Bragg peak, the elemental absorption will cause a cusp at its absorption edge. Therefore, AXS can be used to characterize the elemental chemistry in particular LRO that cannot be unequivocally determined by conventional XRD.

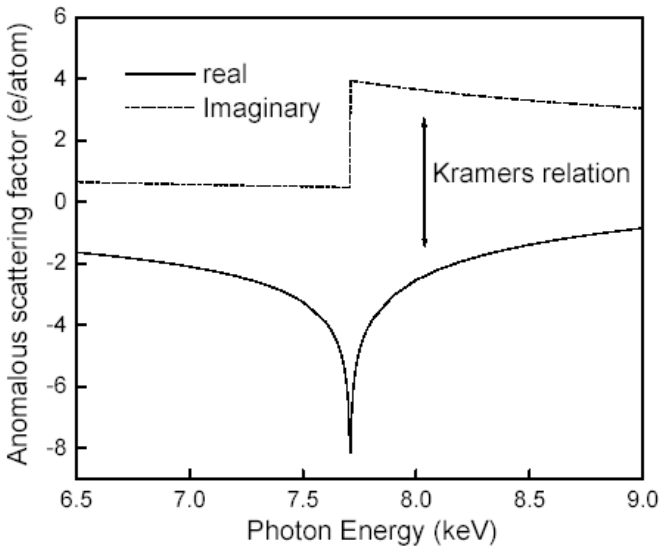

Figure 2-5 The anomalous dispersion terms of $f'(E)$, and $f''(E)$ and their variation as a function of energy is illustrated using the *K*-absorption edge of a Co atom as an example

2.3 Magnetic Characterization

2.3.1 Vibrating Sample Magnetometer (VSM)

The characteristics of any magnetic material, whether it is hard, soft, or intermediate, are best described in terms of their hysteresis loop. The most common measurement method employed for hysteresis loop determination at ambient temperature is the VSM.[69] Properties of materials as a function of magnetic field, temperature, and time could be determined.

The VSM is based upon Faraday's law, according to which an e.m.f. is induced in a conductor by a time-varying magnetic flux. A sample magnetized by a homogenous magnetic field is vibrated sinusoidally at small fixed amplitude with respect to stationary pick-up coils.

As the sample moves, its magnetic field, which is proportional to its magnetic moment, M, alters the magnetic flux through the coils. This induces a voltage across the terminals of the pick-up coils. The voltage is proportional to the magnetization of the sample by the following relationship:

$$V(t) = C\frac{df_i(t)}{dt} \qquad \textbf{(2-9)}$$

where $f_i(t)$ represents the (changing) flux in the pick-up coils caused by the moving magnetic sample. Thereafter, the coil output voltage is combined with the output from the displacement transducer to produce a magnetization signal. Variations in vibration amplitude and frequency are then cancelled out. The signal is then detected by a high gain but narrow bandwidth "lock-in amplifier" and fed along with the applied field signal to an x-y plotter to generate a hysteresis loop.

For hysteresis loop measurement, a DC magnetic filed (H_{max}) which is strong enough to saturate the magnetic sample was applied and then decreased step by step to -H_{max}. Similarly, for the reverse direction, the applied filed was changed from -H_{max} to H_{max}. At each step, the magnetic moment was measured and a hysteresis loop was thus obtained. The hysteresis is of great help to the study of the magnetic properties.

When examining magneto-optical materials, the easy-axis hysteresis loop will be obtained when the applied field is perpendicular to the plane of the sample. To apply the field in the plane of the film, sample is rotated by 90°. The deviation of M_s from the easy axis determines the magnetic anisotropy constant K_u.

The coercivity angular dependence measured with VSM was used in this thesis to compare the magnetization reversal mechanism. Theoretically, the coercivity angular

dependence is different for the two magnetization reversal mechanisms, domain wall motion and domain rotation.

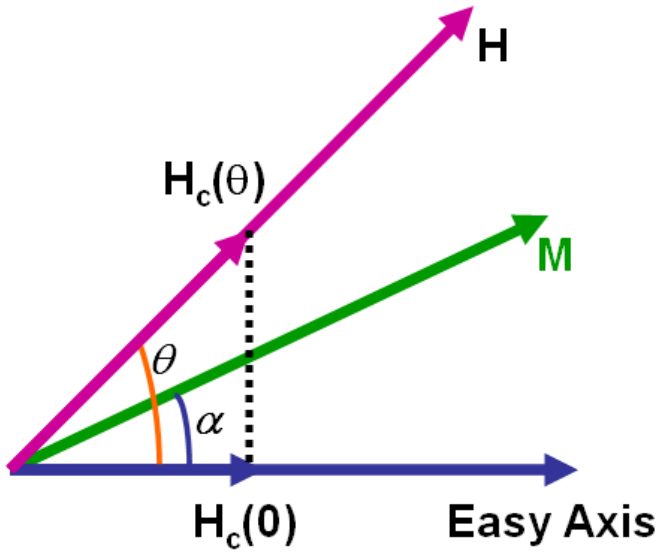

Figure 2-6 Schematic diagram of a single-domain particle with uniaxial anisotropy *K* and applied field H

In domain wall motion mode, coercivity is the critical field for irreversible wall expansion. As shown in Fig. 2-6, M is the magnetization of the material, and H the external applied field and α the angle of magnetization with respect to the easy axis. θ is the angle of external applied field direction with the easy axis. H_c is smallest when the field is applied parallel to the easy axis. Let this value be $H_c(0)$, when the field makes an angle θ with the easy axis, the critical field to reverse the magnetization ($H_c(\theta)$) is:

$$H_c(\theta) = \frac{H_c(0)}{\cos\theta} \qquad \textbf{(2-10)}$$

Therefore, the coercivity angular dependence for domain wall motion mode should follow the trend of

$$\frac{H_c(\theta)}{H_c(0)} = \frac{1}{\cos\theta} \qquad \textbf{(2-11)}$$

In a single domain Stoner–Wohlfarth particle, magnetization reversal is caused by domain rotation. The coercivity angular dependence trend can be expressed as below:[70]

$$\frac{H_c(\theta)}{H_c(0)} = \left(\sin^{\frac{2}{3}}\theta + \cos^{\frac{2}{3}}\theta \right)^{-\frac{3}{2}} \qquad \textbf{(θ ≤ 45º)} \qquad \textbf{(2-12)}$$

$$\frac{H_c(\theta)}{H_c(0)} = \frac{1}{2}\sin 2\theta \qquad \textbf{(θ ≥ 45 º)} \qquad \textbf{(2-13)}$$

2.3.2 Alternating Gradient Force Magnetometry (AGFM)

Alternating gradient magnetometry is highly sensitive measurement to measure the magnetic properties of materials. More specifically, it is used to measure the hysteresis properties of various types of samples. The AGFM uses a different technique from the conventional VSM. In VSM, a sample is positioned in an external magnetic field and vibrated at a constant frequency.

In AGFM, as the name suggests, the sample is mounted to a piezoelectric transducer that oscillates when the sample is subjected to an alternating magnetic field gradient within a variable or static DC field of an electromagnet.

The alternating gradient field is used to exert a periodic force on a sample positioned. The force is actually proportional to the magnitude of the gradient field and the magnetic moment of the sample. The force deflects the sample. The piezoelectric element gives a voltage output, which measures in accordance with the resulting

deflection of the cantilever rod. By operating at or near the mechanical resonance frequency of the cantilever rod, the output signal will be greatly amplified.

AGFM has enjoyed significant acceptance in present magnetic metrology because of its high sensitivity, easy operation and fast measurement. AGFM has a noise level of 10^{-8} emu compared to 10^{-6} emu for the normal VSM.

2.3.3 Magnetic Recording Properties Characterization: Read-Write Testing

Read-write tests were carried out on air bearing spin-stand with a commercial 60 Gbit/in^2 ring head.

The Noise Test measures the ratio between the amplitude of a high-frequency (HF) signal written on a given track and the RMS (root mean square) value of the signal after the track is erased. The SNR testing is defined as:

SNR = 20Log(reproduction output/integration noise) **(2-14)**

In this thesis, the noise and SNR level were tested to compare the media recording performance of pure perpendicular FePt thin film and the FePt thin films with Ag insertion. Prior to the read-write test, the samples were coated with 3 nm carbon and 2 nm Moresco lubricant. The carbon layer and Moresco lubricant layer were used to protect the magnetic media, as per common practice in commercial media materials.

The maximum linear density level at which the SNR and noise were measured was 450 kilo flux charge per inch (kfci). Although the density level is less than half of the current industry benchmark (1000-1200 kfci), the test provides a recording performance comparison between the samples.

Chapter 3. Composite FePt-Ag thin films

FePt thin films prepared below 550 ^{o}C possess randomly distributed *fcc* (A1) phase. Post-annealing or elevated deposition temperature is needed for the phase transformation from A1 to $L1_0$ phase. The side effect of high-temperature treatment are grain coarsening and agglomeration. In order to control grain size as well as to achieve magnetic isolation among grains, various nonmagnetic additives were investigated. Materials such as C,[71,35] AlO_x,[72,73] SiO_2,[74] AlN,[33] SiN_x,[31] BN,[32] Zr,[75] ZrO_x,[41] Cr,[30] Ag,[38] W[36], Ti,[36] HfO_2 [76] were doped into FePt films by post-deposition annealing of co-sputtered or multilayered films. It was found that C, AlO_x, ZrO_x, SiN_x, HfO_2 and Ag were effective to suppress the growth of FePt grains during subsequent annealing. B[77,78] only reduced magnetic coupling and showed little effect on the control of grain size.

Doping with Zr also enhanced the chemical ordering kinetics for annealed polycrystalline films prepared by sputtering.[37] It was proposed that the larger covalent radius of Zr introduced lattice strain and defects in as-deposited films, enhancing diffusion of Fe and Pt and ordering kinetics. However, the H_c of the alloy only increased for films subject to short annealing time. For longer annealing, Zr preferentially reacted with Pt to form an inter-metallic compound at the expense of the FePt $L1_0$ phase.

Elements such as Cu and Ag have been most effective to promote FePt ordering. Maeda et.al. reported that with the addition of the optimized 15 at.% Cu into FePt alloy, the ordering temperature was reduced to 300 °C.[28] The coercivity of $(Fe_{46.5}Pt_{53.5})_{85}Cu_{15}$ film exceeded 5 kOe whereas undoped FePt film remained magnetically soft. It was found that the ternary alloy of FePtCu was formed[79] and Fe sites in the lattice were

substituted by Cu atoms. It was argued that the Gibbs free energy of FePtCu alloy was smaller than that of FePt and thus the driving force for the A1-to-$L1_0$ transformation was enhanced.[80] Takahashi et.al. also reported that the ordering temperature of FePtCu film was reduced.[27] The coercivity was 8 kOe and the ordering parameter was equal to 1 after annealing at 400 °C, while the coercivity and the ordering parameter of undoped FePt films remained very low at the same temperature. The optimized composition was found to be $(FePt)_{96}Cu_4$. The Cu addition enhanced diffusion-driven phase transformation since Cu doping decreased the melting temperature of the alloy. The contradictory results however had been reported by Wierman et al.[81,82] They found that Cu decreased the film coercivity and did not significantly improve the $L1_0$ ordering process. They suggested that the decrease of ordering temperature by Cu doping was due to deviation from the equiatomic FePt composition that would alter the ordering kinetics.[83] Barmark et.al. demonstrated that the ordering temperature showed a large dependence on Fe:Pt ratio by use of differential scanning calorimetry.[84]

Kang et al reported that with 15 vol.% Ag addition in FePt nanoparticles, the coercivity of the nanoparticles assembly was more than 10 kOe after 500 °C annealing.[85] Without Ag addition, FePt nanoparticles assembly was only 2 kOe. In this case both FePt and FePt-Ag nanoparticles were well separated. The increase of coercivity of FePt-Ag may therefore be attributed to the increase of $L1_0$ ordering and magnetocrystalline anisotropy.

The above ordering temperature reduction in FePt-Ag system was achieved by post-deposition annealing. In-situ annealing has not been systematically studied while it is more favorable for industry production. In this Chapter, composite FePt-Ag thin films

by cosputtering were studied in order to achieve in-situ ordering under relatively low temperature.

3.1 Composite FePt-Ag thin films on glass substrate

FePt thin films deposited on amorphous glass substrates normally show *fcc* phase and random of magnetic easy axis. Cosputtering Ag with FePt directly on glass substrate can simplify the analysis and exclude the effects from other layers in multilayer structure. In this section, FePt-Ag composite thin films cosputtered on glass substrates were studied to see the effects of Ag on FePt properties.

3.1.1 Sample preparation and characterization

Cosputtered FePt-Ag samples with thickness of 100 nm and various Ag concentrations were directly fabricated on corning 7059 glass substrates. The pre-heated substrate temperature was 350 ^{o}C. The base pressure was better than 1×10^{-7} Torr. The Ag concentration was controlled by varying the deposition rate of Ag. Ag concentration ranged from 0 to 70 vol.%.

Sample texture and phase were characterized by XRD with Cu K-α source. Sample microstructure was investigated with TEM. The magnetic properties were studied with VSM.

3.1.2 Structure and microstructure characterization

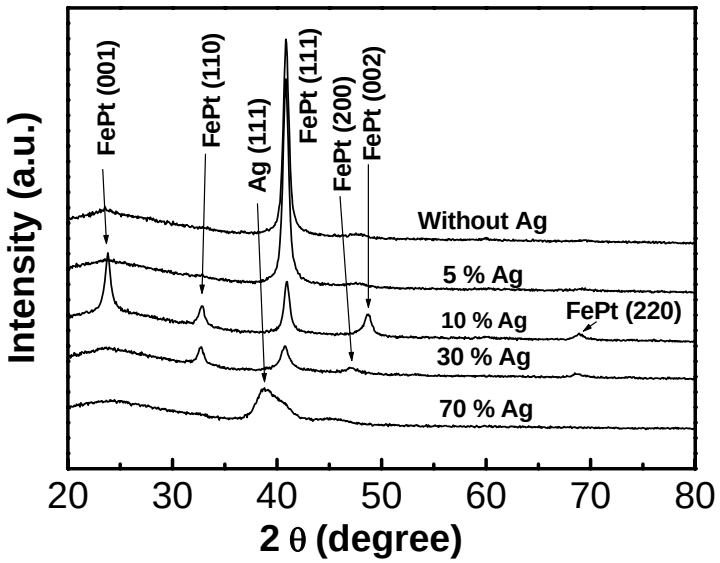

Figure 3-1 XRD scans of 100-nm FePt thin films on glass substrates with different Ag volume fraction

Figure 3-1 showed the XRD scans of FePt films cosputtered with different Ag concentrations on glass substrates. The pure FePt (without Ag) thin film showed a dominant *fcc* (111) texture with a broad hump corresponding to FePt(001). No superlattice peak was observed. For this sample, XRD χ and ψ scans at the peak position of FePt(001) (2θ =23.9 °) did not show higher diffraction intensity than the hump in the θ-2θ scan (Fig. 3-2), confirming the low fraction of FePt(001) in the 3-dimensional space.

For the sample with 10 vol.% Ag, superlattice FePt(001) and (110) peaks emerged, whereas the intensity of the FePt(111) peak significantly decreased. This confirmed that the (111) texture was no longer dominant with 10 vol.% Ag addition. The superlattice reflections indicated the transformation of the *fcc* phase to the $L1_0$ phase. When Ag volume fraction further increased to 30 vol.%, FePt(001) peak became a wider hump while FePt(110) peak remained the same intensity as that with 10 vol.% Ag addition. The decreased FePt(001) intensity indicated the suppression of perpendicular orientation.

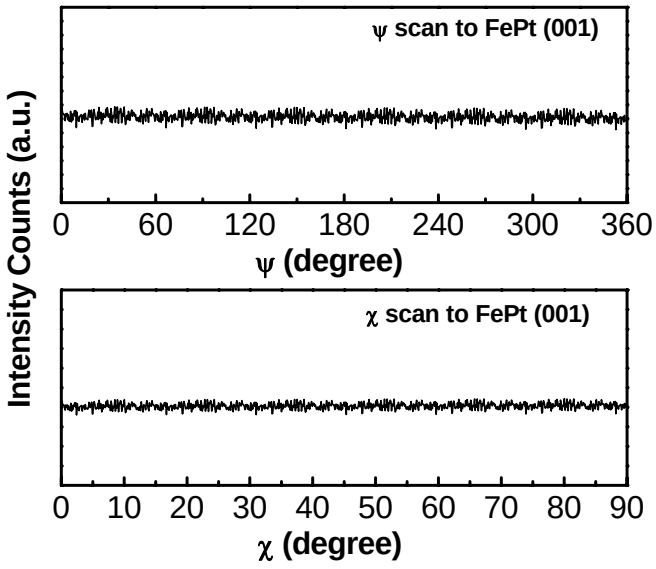

Figure 3-2 XRD χ and ψ scans to FePt(001) peak of 100-nm FePt thin films on glass

$L1_0$ phase transition normally occurs above 550 ^oC for FePt thin film deposited directly on amorphous glass substrate. Our results showed that the ordering temperature of FePt thin film was reduced by more than 200 ^oC with the cosputtering of Ag. The reduced ordering temperature is favorable for industry application. The reduction of ordering temperature of CoPt or FePt alloy thin films doped with other elements has been reported. For example, surface segregation of Ag to film surface was observed in CoPt-Ag system, and the driving force for reduced ordering temperature was attributed to the vacancy-enhanced phase transition created by Ag surface segregation.[86] A1-to-$L1_0$ phase transformation is a diffusion-based reaction by the vacancy mechanism. The atomic size of Ag is comparable to Co and Pt. Ag tended to diffuse to surface due to its low surface energy, creating vacancies in the film. Reduction of the activation energy for vacancy formation and diffusing mobility can be expected when Ag was incorporated in the lattice. Thermodynamic calculations suggested that the ternary FePt-Cu alloy was favorable for

the transformation of disordered to ordered phase.[80] We will discuss the Ag distribution and its correlation to ordering temperature in cosputtered FePt-Ag thin films in Chapter 4.

Table 3-1 Comparison of FePt(111) and FePt(110) peaks in terms of peak position, intensity area and peak width for cosputtered FePt-Ag thin films on glass

Sample	FePt(111)			FePt(110)			(111)/(110)
	Position	Area	FWHM (°)	Position	Area	FWHM (°)	
FePt	40.87	2147	0.58	-	-	-	-
FePt+5 vol.%Ag	40.84	2283.7	0.60	32.832	11.204	0.20	203.83
FePt+10 vol.%Ag	40.82	583.09	0.61	32.797	245.29	0.65	2.38
FePt+30 vol.%Ag	40.75	394.01	0.93	32.715	219.18	0.67	1.80

Detailed comparisons of FePt(111) and FePt(110) peaks by Gussian fitting after background subtraction were summarized in Table 3-1. It is noted that the peak position for both FePt(111) and FePt(110) shifted to lower angles with increasing Ag fraction. The lower angle of FePt(110) indicated the expansion of *a* lattice parameter. If unit cell volume remained constant, the *c* lattice parameter should be shrunk. The left shift of FePt(111) peak indicated an increased FePt(111) interplannar spacing, which also suggested a larger degree of transformation to tetragonal phase. Therefore, the $L1_0$ phase ordering was improved with addition of Ag. Peak broadening with increasing Ag fraction was observed in both peaks indicating the decrease in grain size according to Scherrer's equation (Eq. 2-2). The observed size restraining effect of Ag is favorable for application. The increasing intensity ratio of FePt(110)/FePt(111) suggested that FePt(110) texture was enhanced with the increasing Ag fraction in the cosputtered FePt-Ag thin films.

HRTEM measurements were attempted to investigate the phase separation between FePt and Ag. Figure 3-3A showed the bright field TEM images of the sample with 30 vol.% Ag, in which mixed FePt(200) and FePt(111) lattice fringes were observed. The d-spacings of FePt(200) and FePt(111) planes are 1.92 Å and 2.20 Å, respectively,

corresponding to that of FePt alloy. Consistent with the XRD data, FePt(100) and FePt(110) superlattice reflections were observed in the selected area diffraction (SAD) pattern Fig. 3-3B, confirming the formation of $L1_0$ phase. However, separate Ag grain was not observed in the HRTEM images.

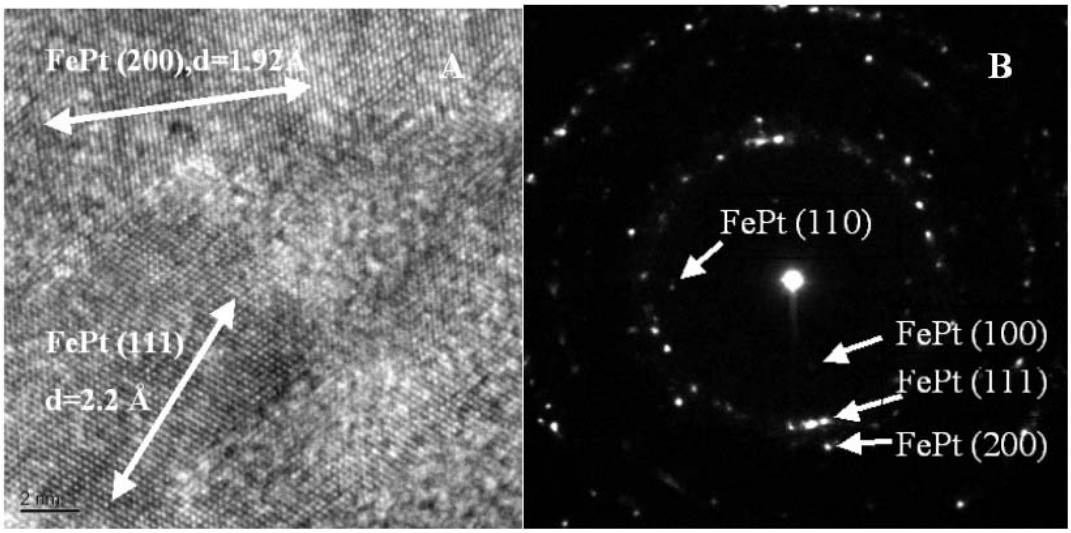

Figure 3-3 TEM images of 100-nm FePt thin film cosputtered with 30 vol.% Ag. A) High resolution image; B) Selected area diffraction pattern

Although bulk binary phase diagram of Fe-Ag found in the literatures showed very low solubility of Ag in Fe (< 0.022 at.%) even at 1398 ^{o}C, metastable solubility may be possible when the grain size falls within nanoscale due to the high ratio of surface atoms and significant surface energy. In addition, Pt-Ag alloy is possible according to binary phase diagram.[26] SEM cannot provide more information about alloying and phase separation for the dark area in the image.

The shift of FePt peak position with Ag fraction that was observed in the XRD data suggested possible alloying between FePt and Ag. However, we could not draw a clear conclusion on the FePt-Ag alloying only on the basis of existing data, because:

1. In spite of alloying, FePt lattice variation could be caused by the lattice mismatch between Ag and FePt, considering that Ag(200) lattice is close to FePt(200).
2. As we discussed previously, conventional XRD and electron diffraction in TEM have the deficiency of identifying the phase between close elements and their alloys. In our case, Ag peak was absent in the XRD spectra when Ag fraction was 30 vol.% and below. However, the Ag atomic number is close to the average of Fe and Pt. Overlapping of close peaks may give misleading information, rendering it difficult to identify Ag from FePt by conventional diffraction spectroscopy.

Therefore, alternative characterization technique with elemental selectivity is necessary to further study the alloying in cosputtered FePt-Ag thin films.

3.1.3 Magnetic properties

The hysteresis loops of the FePt thin films with different Ag fractions are shown in Fig. 3-4. The low coercivity of the FePt sample without Ag agreed with the XRD results showing a dominant *fcc* FePt(111) texture. In-plane anisotropy of this sample was observed. Both the in-plane (//) and out-of-plane (⊥) H_c was only a few hundred Oe. The low coercivity indicated that the majority of FePt remained magnetically soft.

With the addition of 10 vol.% Ag, the close values of $H_{c\perp}$ and $H_{c//}$ suggested that the magnetic easy axis was neither longitudinal nor perpendicular. The changed easy axis alignment was consistent with the mixture of FePt(001) (⊥ alignment of magnetic easy axis) and FePt(110) (// alignment of magnetic easy axis). With further increase of Ag concentration to 30 vol.%, the magnetic anisotropy switched back to the // direction,

agreeing with the XRD result of preferred orientation of in-plane peaks of FePt(110) and FePt(111). While the FePt film with 10 vol.% Ag was not magnetically saturated under the applied filed, the in-plane loops of the samples without Ag and with 30 vol.% Ag were saturated. Moreover, the $H_{c//}$ was higher than $H_{c\perp}$, further confirming the dominant longitudinal anisotropy.

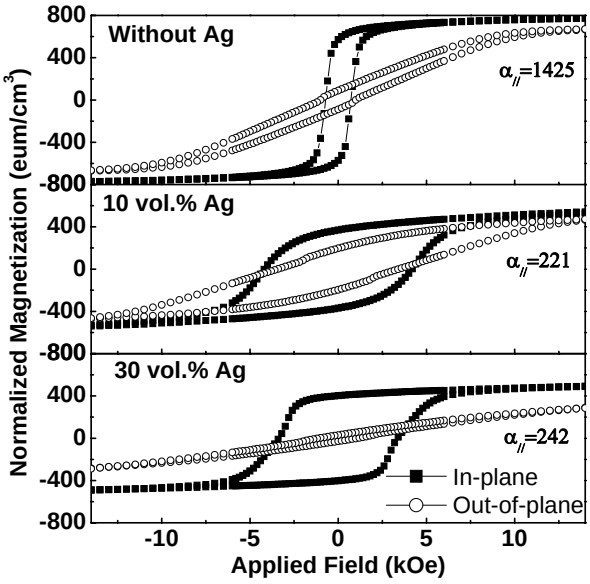

Figure 3-4 Hysteresis loops of 100-nm FePt thin films on glass substrates with different Ag volume fraction, where the magnetization is normalized by FePt thickness

The increased H_c could be correlated to the $L1_0$ phase enhancement that was reflected by FePt(001) and FePt(110) superlattice reflections in XRD results.

The loop-slope parameter $\alpha=dM/dH$ $(_{H=Hc})$ was commonly used as a measure of the exchange coupling in magnetic recording media. Since stronger exchange coupling causes more coherent magnetization rotation in thin films, the loop slope at coercive field increases with increasing exchange coupling. The FePt thin film without Ag showed the highest α value, indicating strong exchange coupling. The samples with Ag co-sputtered,

showed much lower α value, indicating the reduction of exchange coupling. The α values for the FePt samples with 10 vol.% and 30 vol.% Ag were comparable.

The trend of $H_{c//}$ and $H_{c\perp}$ as a function of Ag fraction was shown in Fig. 3-5. $H_{c//}$ and $H_{c\perp}$ followed similar trend and increased with increasing Ag concentration in the range of 0-10 vol. % Ag. The sample with 10 vol.% Ag showed maximum $H_{c//}$ and $H_{c\perp}$. Further increase in Ag fraction resulted in a decrease of coercivity, which may be attributed to the size reduction effect that is reflected by XRD line broadening.

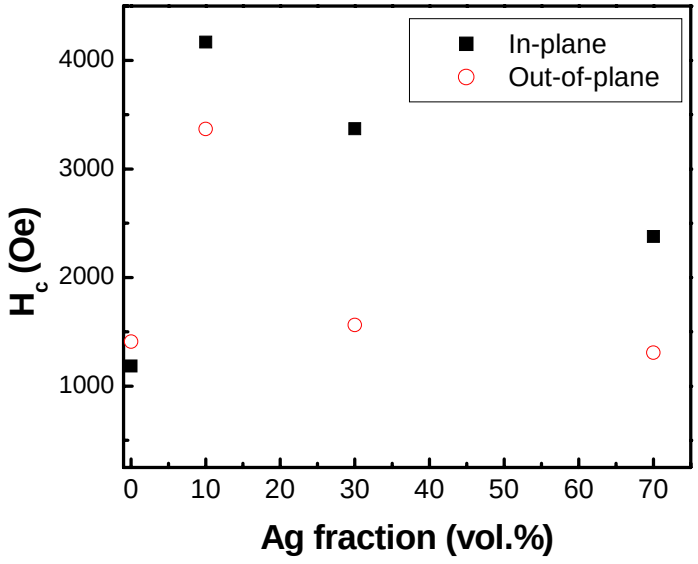

Figure 3-5 In-plane and out-of-plane H_c as a function of Ag fraction for cosputtered FePt-Ag thin films on glass

The saturation magnetization (M_s) value decreased with increasing Ag fraction due to the diluting effect of Ag (Fig. 3-6). It is noted that the M_s value of the sample with 30 vol.% Ag reduced to ~700 emu/cm^3 (normalized with the thickness of FePt) compared to the sample without Ag (M_s ~800 emu/cm^3). If Ag atoms entered the FePt lattice, M_s value would be lowered since M_s is closely related to the concentration of nonmagnetic

materials in the lattice.[31] However, it is possible that the interface effect also accounts for the M_s reduction even though the Ag atoms were not within the FePt lattice.

The increase of in-plane squareness ($S_{//} = M_r/M_s$) with increasing Ag fraction up to 30 vol.% supported the improvement of longitudinal FePt texture (Fig. 3-6). The increased $S_{//}$ is favorable for SNR improvement.

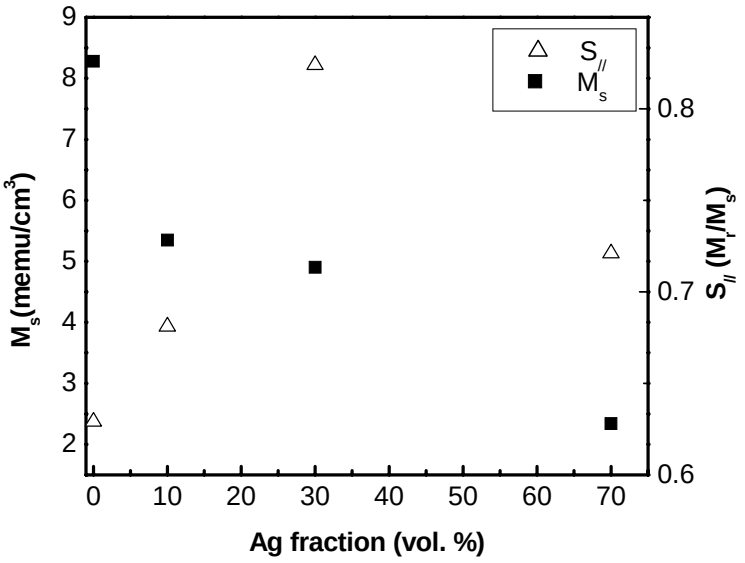

Figure 3-6 M_s and in-plane squareness ($S_{//}$) as a function of Ag fraction

3.2 Composite FePt-Ag thin films on CrRu underlayer

As discussed in Chapter 1, $L1_0$ ordering and perpendicular texture can be achieved at a relatively low temperature of 350 °C by means of CrRu underlayer. However, the extent of ordering need to be enhanced, and the grain size and exchange coupling of FePt thin films deposited on CrRu underlayer need to be reduced for better SNR performance. The favorable effects of Ag observed in section 3.1 suggested a method to further improve the structural and magnetic properties in perpendicular FePt

thin film. In this section, Ag was cosputtered with FePt on CrRu underlayer, in order to further improve the properties.

3.2.1 Sample preparation and characterization

The sample structures are schematically shown in Fig. 3-7. Films of $(FePt)_{100-x}Ag_x$/Pt/$Cr_{90}Ru_{10}$/glass (x is volume fraction) were deposited on corning 7059 glass by DC magnetron sputtering. The Ag contents in the films ranged from 0 to 80 vol.% by varying the sputtering power for Ag, while keeping FePt power fixed. The volume concentration of Ag was estimated from the deposition rate dependence of Ag film on sputtering power. The chamber base pressure was better than 2×10^{-8} Torr. The Pt intermediate layer was used to block the Cr diffusion from the underlayer. The thickness of the magnetic layer, Pt intermediate layer, and $Cr_{90}Ru_{10}$ underlayer were fixed at 20 nm, 4 nm, and 30 nm, respectively. The samples were covered with a 2 nm Pt layer at room temperature to prevent oxidation.

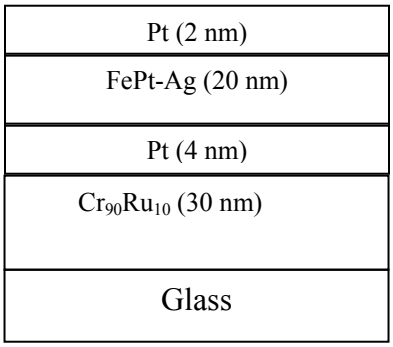

Figure 3-7 Structure illustration of cosputtered FePt-Ag thin films

3.2.2 Structure and microstructure characterization

The XRD spectra for the samples with various Ag concentrations are shown in Fig. 3-8. Without Ag, the strong *fct* FePt(001) superlattice peak indicated the good

ordering and perpendicular orientation of the *c* axis. The FePt(001) rocking curve had a FWHM of 5°, confirming the high degree of FePt(001) texture.

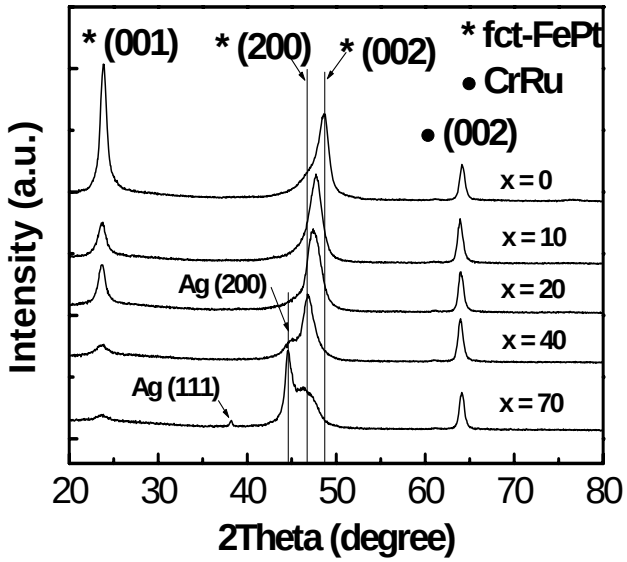

Figure 3-8 XRD scans of $(FePt)_{1-x}$-Ag_x films on CrRu underlayer

The FePt(002) peak was asymmetric, suggesting the overlap of the Pt(002), FePt(002) and FePt(200) peaks. As the Ag concentration increased, the FePt(002) peak shifted gradually to FePt(200) peak and the intensity of the FePt(001) peak decreased. When the Ag concentration exceeded 40 vol.%, the FePt(001) peak significantly decreased. These results indicated that cosputtering of Ag promoted the growth of the FePt longitudinal (200) texture and suppressed the perpendicular FePt(001) texture.

Table 3-2 Fitting result of XRD spectra with various Ag content

Sample	FWHM			(001)/(002) ratio	(200)/(001) ratio
	FePt (001)	FePt (002)	FePt (200)		
FePt	0.83	0.98	3.22	20.61	1.02
FePt+10 vol.%Ag	1.12	1.21	3.50	7.21	2.16
FePt+20 vol.%Ag	0.95	1.36	4.14	6.01	2.25
FePt+40 vol.%Ag	1.58	2.17	0.95	3.11	2.73

Peak width and integrated intensity can be obtained by fitting the XRD spectra. Since Ag(200), FePt(200) and FePt(002) peaks are located close to each other, deconvolution fitting was conducted for them. The analysis results were summarized in Table 3-2.

The promotion of longitudinal texture by Ag was reflected by the increased ratio of FePt(200)/(001). The intensity ratio of FePt(001)/(002) is commonly used to characterize the ordering degree in perpendicular FePt thin films,[87] because it reflects the relationship between the superlattice and fundamental peaks in XRD spectra. In Table 3-2, the intensity ratio of FePt(001)/(002) decreased with increasing Ag content. However, it is insufficient to characterize the ordering trend in this series of samples, because the film texture changed significantly from sample to sample.

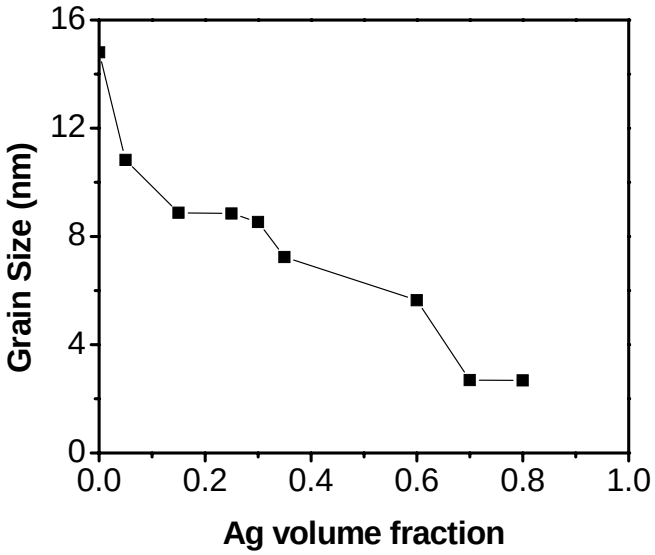

Figure 3-9 FePt grain size as a function of Ag content (calculated from XRD line broadening)

The broadening of FePt peaks with increasing Ag content was observed, indicating the size restraining effect of Ag. The average FePt grain size estimated from XRD line broadening of FePt(001) and FePt(200) peaks monotonically decreased with

increasing Ag concentration, indicating the efficient reduction of magnetic grain size by cosputtering with Ag (Fig. 3-9).

The evolution of the FePt texture with Ag doping could be caused by the competition of the epitaxial-strain energy and grain-boundary energy.[88,89,90] When FePt is cosputtered with Ag, the energy equilibrium which favors the development of FePt(001) texture could be broken and the effect of the grain boundary energy could be enhanced.

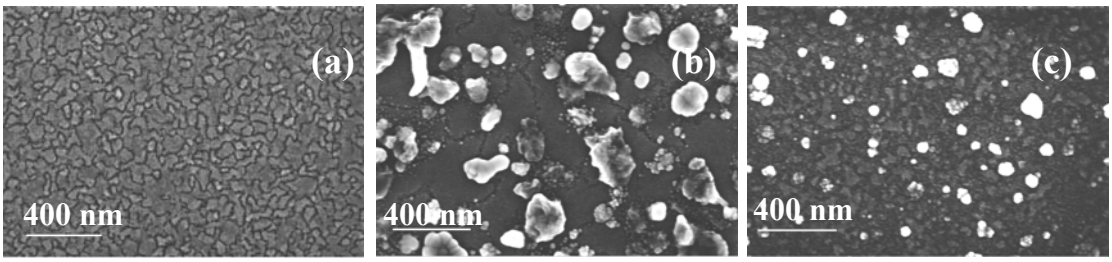

Figure 3-10 SEM images of FePt samples cosputtered with a) 15 vol.%; b) 40 vol.%; and c) 70 vol.% Ag

When Ag content was less than 40 vol.%, Ag peak was absent in the XRD spectra, which is consistent with the result in section 3.1. The textured Ag(200) peak appeared with the further increase of Ag content, indicating the phase separation of Ag. The Ag(200) texture could be due to the epitaxial growth of Ag(200)[001] || CrRu(002)[110], where the lattice mismatch is only 0.2%.

The SEM images of the samples with different Ag content were shown in Fig. 3-10. While no phase separation was observed for the samples with 15 vol.% Ag, clear phase separation was observed for the samples with 40 vol.% and 70 vol.% Ag.

Figure 3-11 compared the EDX spectra of the dark and bright areas for the sample with 40 vol.% Ag content. The spectra revealed much higher Ag and Pt composition in the bright areas than in the dark areas, indicating the phase separation in the films. It was noted that Ag EDX peak was also seen for the dark areas, indicating the existence of Ag

with relatively uniform distribution. Alloying or grain boundary distribution of Ag could be possible.

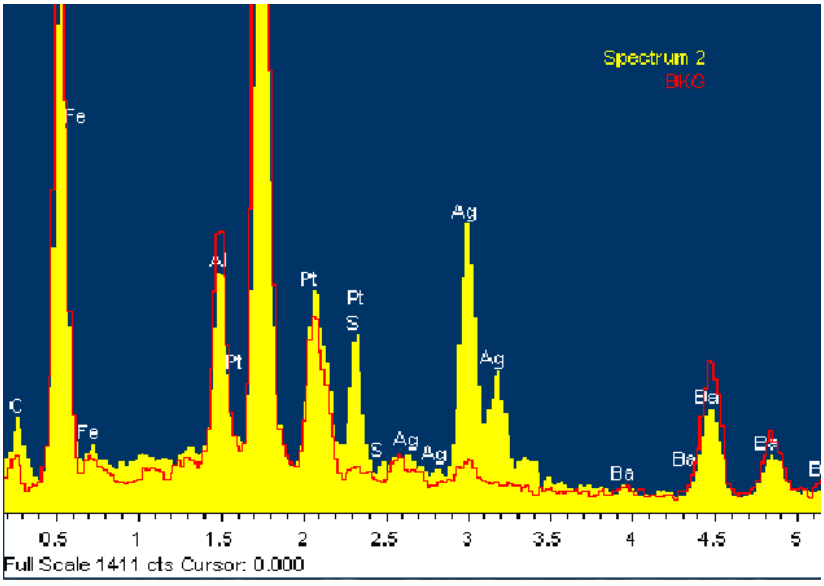

Figure 3-11 EDX spectra of the sample with 40 vol.% Ag

The phase segregation with increasing Ag content resulted in the increase of film roughness as shown in Fig. 3-12. It may be attributed to the low surface energy of Ag, which promoted island structure on the surface to minimize the total energy.

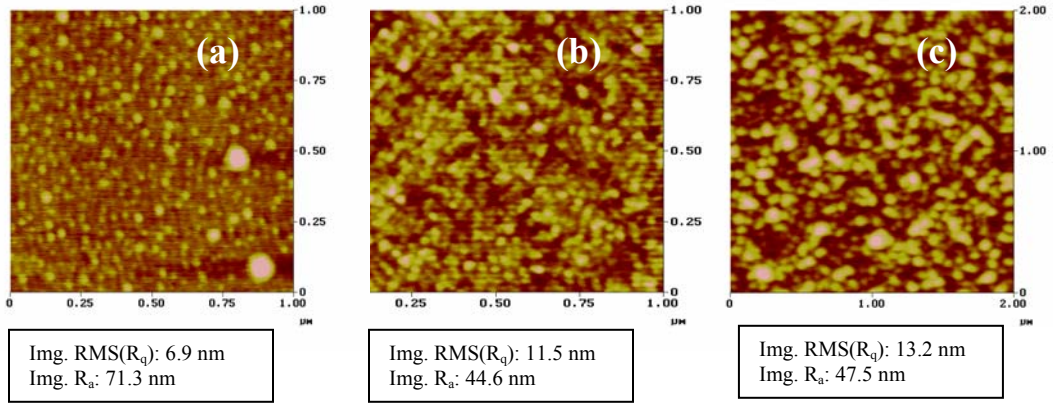

Figure 3-12 AFM images of the FePt thin films with a)15 vol.%; b)40 vol.%; and c)70 vol.% Ag

The high roughness is unfavorable for application, as lower head flying height is required for more effective writing and better SNR. From this point of view, Ag content needed to be carefully controlled to alleviate this morphology problem.

Figure 3-13 showed the plane view TEM images of the samples with 30 vol.% and 70 vol.% Ag content. The FePt grain size decreased from ~25 nm to ~7 nm, when Ag content increased from 30 to 70 vol.%. The estimation of grain size was obtained by averaging the diameters of 25 grains in each TEM image. This result confirmed the size reduction base on the XRD data.

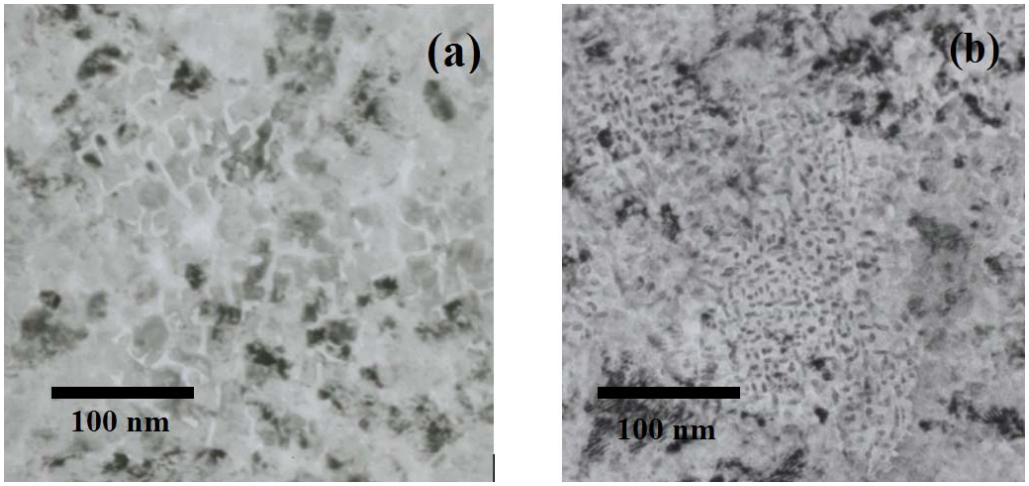

Figure 3-13 Bright field TEM images of cosputtered FePt-Ag samples with a) 30 vol.% Ag and b) 70 vol.% Ag

3.2.3 Magnetic properties

Figure 3-14 showed the in-plane and out-of-plane hysteresis loops of the FePt film with different Ag concentrations. The hysteresis loops revealed a change of magnetic easy axis from perpendicular to longitudinal direction with increasing Ag fraction in the thin films. The FePt film without Ag showed a perpendicular anisotropy

with out-of-plane coercivity ($H_{c\perp}$) of ~2.6 kOe. For the FePt film with 20 vol.% Ag, a high in-plane coercivity ($H_{c//}$) of ~5.5 kOe was obtained.

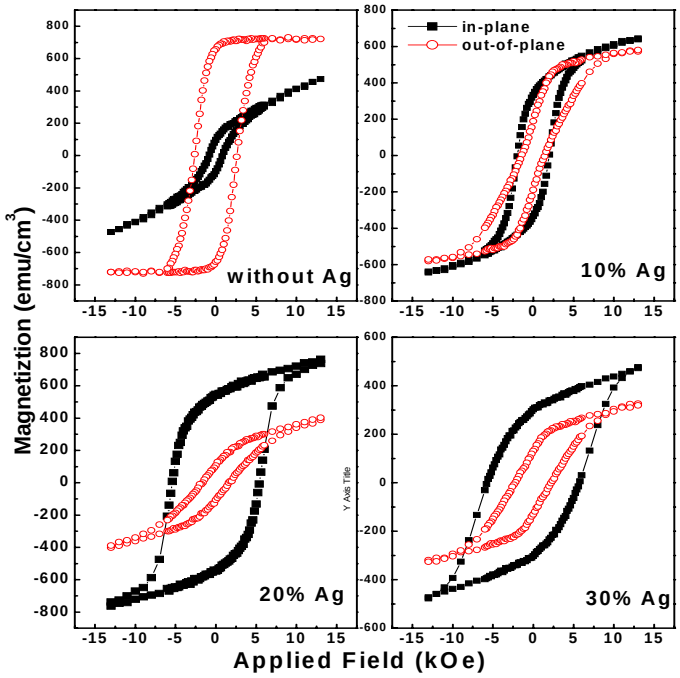

Figure 3-14 In-plane and out-of-plane hysteresis loops of FePt thin films with different Ag fraction

In-plane and out-of-plane coercivities as a function of Ag content are shown in Fig. 3-15. From 0 to 15 vol.% Ag, $H_{c//}$ increased whereas $H_{c\perp}$ decreased, confirming the switch of magnetic easy axis from perpendicular to longitudinal direction. The increases of both $H_{c//}$ and $H_{c\perp}$ in the range of 15 to 30 vol.% Ag may be due to the increase of pinning sites with Ag doping, rendering the reversal of magnetic domains difficult in both directions. Further increase of Ag content above 30 vol.% resulted in the decrease of both $H_{c//}$ and $H_{c\perp}$. The decrease in grain size of FePt may account for the decreases in both $H_{c//}$ and $H_{c\perp}$ when Ag content above 30 vol.%. Other factors, besides the chemical ordering which increases the anisotropy constant (K_u), can also affect H_c. For example, magnetic

pinning effect, magnetic reversal mechanism and exchange coupling etc., would have significant influence on coercivity.70

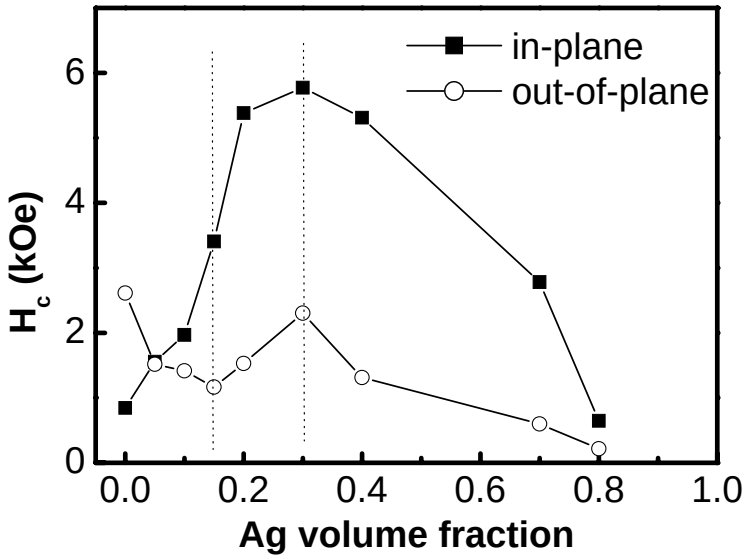

Figure 3-15 In-plane and out-of plane coercivities as a function of Ag content

With the consideration of thermal fluctuation, the size dependence of coercivity for an assembly of randomly orientated non-interacting particles may be described as the following: [13,14]

$$H_c = [1-(D_p/D)^{0.77}](0.96K_u/M_s), \quad \textbf{(3-1)}$$

where D_p is the critical grain diameter for superparamagnetism, which is estimated to be

$$D_p = [150k_BT/(\pi K_u)]^{1/3}, \quad \textbf{(3-2)}$$

For FePt alloy, D_p is about 3 nm at room temperature.[15]

Angular coercivity dependence on Ag content shown in Fig. 3-16 indicated that magnetic reversal mechanism also changed with Ag content in these FePt films. The ideal domain wall motion mode follows the $1/\cos\theta$ curve, where θ is the angle between the applied field and the magnetic easy axis. The magnetic reversal mechanism deviated

from the ideal domain wall motion mode and approached the rotation mode with increasing Ag concentration. This change may be due to stronger pinning with increasing Ag concentration. The nonmagnetic isolation made the reversal approach to Stoner-Wohlfarth rotation mode.

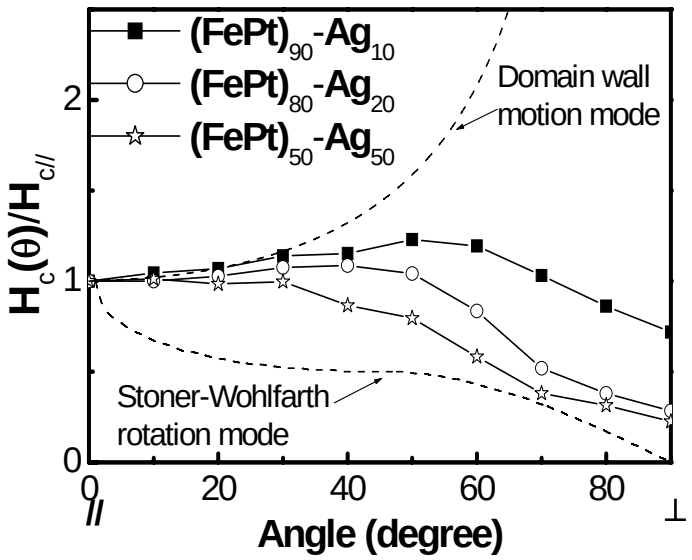

Figure 3-16 Angular coercivity dependence of FePt films with various Ag contents

The $L1_0$ FePt films deposited by magnetron sputtering tend to grow with the (111) texture, tilting *c* axis at 36^o above the film plane.[41] $L1_0$ FePt films with *c* axis normal to the film have been prepared by various methods. However, very few literatures reported on the *fct*-FePt films with *c* axis lying in the film plane. By applying the MBE technique, $L1_0$ FePt was grown epitaxially on $SrTiO_3$ (110) and MgO(110) single-crystal substrates with the *c* axis of grains parallel to film plane, resulting in longitudinal magnetic anisotropy.[91,92] $L1_0$ FePt films with the (200) texture were induced on CrRu (002)/glass by introducing impurities such as air bleeding during deposition.[88] However, it is difficult to control the amount of impurity, grain size, and exchange coupling by this method. Control over the FePt texture by adjusting the Ag concentration would be relatively

easier. In addition, the enhanced coercivity and reduced grain size are favorable for application.

3.2.4 Relationship between microstructure and magnetic properties

The change in coercivity can be caused by many factors. To better understand the coercivity enhancement in cosputtered FePt-Ag thin films, the temperature dependence of H_c and M_s was studied for the sample with 20 vol.% Ag on CrRu underlayer. The selection of 20 vol.% Ag was because of its high H_c.

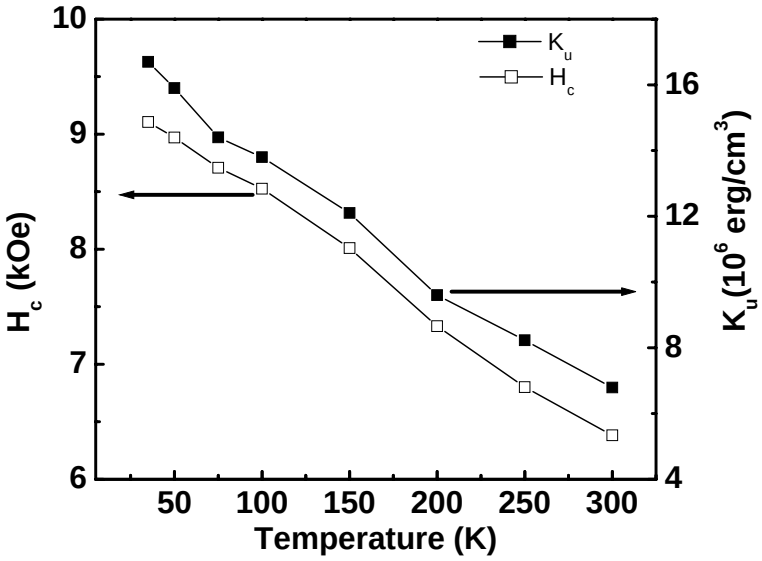

Figure 3-17 Coercivity and anisotropy constant as a function of temperature

Corresponding K_u can be obtained by

$$K_u = H_k \cdot M_s / 2 \qquad \textbf{(3-3)}$$

where the anisotropy field H_k was estimated by extrapolating the in-plane and out-of-plane magnetization curves. The temperature dependence of in-plane H_c and K_u is shown in Fig. 3-17.

Kronmüller and others developed the theory for the coercivity mechanism.[93-95] The model assumes a domain wall pinning by a magnetically inhomogeneous region that is described by $\mathbf{r_0}$ in size. Such an inhomogeneous region is defined as the region that has a different exchange constant A′ and the anisotropy constant K′ from those of the matrix homogeneous region with A and K, respectively. Generally, the coercivity $H_c(T)$ is given by

$$H_c(T) = 2\alpha K_u / M_s - N_{eff} M_s \qquad \textbf{(3-4)}$$

where α is a parameter responsible for a microstructure determined by the coupling strength between the wall and the wall pinning site. N_{eff} is a demagnetization factor, which consists of the macroscopic and microscopic demagnetizing effects. The macroscopic factor is given by the sample geometry and the microscopic one relates to the size and type (magnetic/nonmagnetic) of the pinning site. In case that the inhomogeneous size $\mathbf{r_0}$ is smaller than the wall width $\boldsymbol{\delta_B}$, one can write the coercivity H_c as follows:

$$H_c(T) = \alpha'(r_0 / \delta_B)(2K_u / M_s) - N_{eff} M_s \qquad \textbf{(3-5)}$$

where α' is related to the exchange coupling constant and the anisotropy constant of the matrix and the pinning site. The domain wall width $\boldsymbol{\delta_B}$ is given by $\pi(A/K_u)^{1/2}$, which is temperature-dependent as well.[96] By using the measured values of all K_u, M_s and H_c and assuming the exchange constant A for the FePt host region is 1×10^6 erg/cm^3, exchange constant and the anisotropy constant for the inhomogeneous region are A′=0.5A, K′=0, respectively, we obtain:[94]

$$\alpha' = \frac{\pi}{3\sqrt{3}}\left(\frac{A}{A'} - \frac{K'}{K}\right) = \frac{2\pi}{3\sqrt{3}} \approx 1.2092 \qquad \textbf{(3-6)}$$

The sample of $(FePt)_{80}$-Ag_{20} was tested using Eq. 3-5. Figure 3-18 is the fitting curve based on Eq. 3-5.

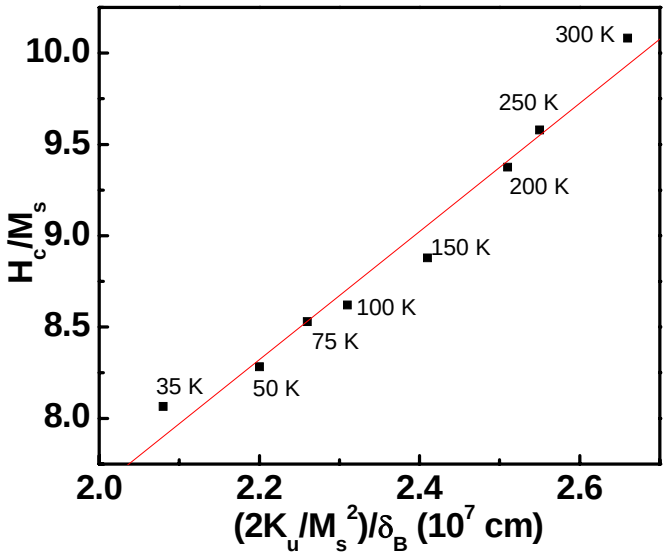

Figure 3-18 A linear fitting to the experimental data after Eq. 3-5

The fact that the $[H_c/M_s, (2K_u/M_s^2)/\delta_B]$ experimental points measured at different temperatures are on a straight line implies that the domain-wall pinning was the dominant mechanism. From the fit, $r_0\alpha'$ was estimated to be 3.51. Therefore the size of Ag as pinning site was estimated to be ~2.9 nm. The small pinning site may account for the absence of Ag peak in XRD spectra (Fig. 3-8).

$L1_0$ FePt material has a fundamental advantage of the narrow wall width (δ_B) estimated at 4 nm from $\delta_B = \pi(A/K_u)^{1/2}$. Hence, the pinning effect would be easily enhanced by small inhomogeneous sites in the film, and the domain size and wall movements would be restricted by the pinning sites.

3.3 Summary

The ordering temperature of FePt thin films deposited on glass substrates can be reduced to 350 ^{o}C by cosputtering with Ag. The film texture and coercivity depended on the Ag concentration.

Cosputtering Ag with FePt on $Cr_{90}Ru_{10}$ underlayer not only changed the film texture and magnetic easy axis from the out-of-plane to the in-plane direction, but also reduced the magnetic grain size and enhanced the coercivity. Ag addition was an efficient way to fabricate $L1_0$ FePt thin film with longitudinal anisotropy.

Ag-rich phase separated from FePt in cosputtered FePt-Ag films with high Ag concentration, which led to high surface roughness. The alloying between FePt and Ag was critical for the understanding of the effects on structural and magnetic properties. However, XRD and TEM alone were not able to confirm the alloying.

Coercivity mechanism study revealed that the coercivity enhancement in cosputtered FePt-Ag thin films was mainly due to the pinning effect of the dispersed Ag.

Chapter 4. AXS and EXAFS investigation on cosputtered FePt-Ag thin films

In cosputtered FePt-Ag thin films, we observed significant effects of Ag concentration on film structure and magnetic properties at a relatively low temperature of 350 °C. The enhancement of ordering may be due to the alloying and diffusion of Ag in the nanostructured FePt thin films. However, the distribution of Ag and its miscibility with FePt in the films remained unclear.

In Chapter 3, it is noted that separated Ag phase was absent in the XRD spectra of the cosputtered FePt-Ag thin films when Ag content was less than 30 vol.%, whereas separated Ag-rich phase was observed by SEM and XRD when Ag concentration was high. Since the film texture and magnetic properties varied significantly with the Ag concentration, the alloying information is critical to understand the properties of these films. It was reported that Ag formed substitutional solid solutions with FePt,[80] and metastable FePt-Ag ternary alloy was claimed. However, the conclusion drawn on conventional XRD and the Vegard's Law may not be necessarily valid. In an inhomogeneous material, single-peak information obtained from XRD may provide the wrong information on phase identification, because a nanostructured solid solution cannot be identified unequivocally from a nanocomposite using conventional XRD.[97] When the grain size is small enough, a single peak may be an overlap of two phases with close lattice parameters and x-ray structural coherence due to the size broadening effect. Therefore, a claim of solid solution based on the single peak becomes misleading. In our

cosputtered FePt-Ag system, the small grain size and close lattice parameter of FePt and Ag must be taken into consideration before reaching the conclusion on alloying.

AXS is a useful tool that can directly provide chemical and structural information simultaneously.[98, 99, 100] Using AXS measurement near Ag edge at a particular FePt Bragg's peak, we can directly find out whether Ag resides in the FePt LRO. In this chapter, the advantages of AXS were taken to examine the phase miscibility of Ag in FePt LRO. The elemental sensitivity of AXS can provide more reliable information on FePt-Ag alloying. In addition, EXAFS analysis is a powerful tool to investigate the local atomic environment of the constituents.

4.1 Sample preparation and characterization

AXS spectrum is the diffraction intensity as a function of the energy near the absorption edge of the element of interest. In the viewpoint of statistics, high diffraction intensity is helpful to reduce the data uncertainty in AXS measurement. Therefore, MgO single crystal substrates were used to induce epitaxial growth and achieve better FePt texture, considering the lattice mismatch between MgO(100) (a = 4.214 Å) and FePt(100) (a = 3.861 Å) is only 8.4%. Good FePt texture on MgO substrates can simplify the analysis and exclude the effects of other factors.

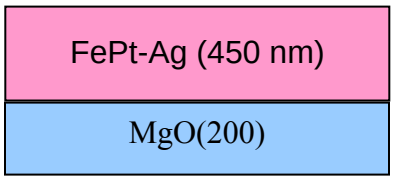

Figure 4-1 Structure illustration of FePt-Ag thin films cosputtered on MgO single crystal substrate

The FePt-Ag thin films were fabricated on MgO(200) single crystal substrates by cosputtering from FePt and Ag targets in an UHV magnetron sputtering system. The substrates were preheated to 350 °C prior to deposition. The volume fraction of Ag was estimated by the deposition thickness rate of FePt and Ag. Film thickness was fixed at 450 nm to further enhance the diffraction counts and reduce the data uncertainty. The vacuum pressure before deposition was better than 5×10^{-8} Torr.

The AXS experiments were conducted on the beamline 20-I of PNC-CAT, Advanced Photon Source (APS), Argonne National Laboratory, USA. Prior to AXS measurements, wide θ-2θ scans were performed on the FePt-Ag samples in order to find out the specific momentum transfer for the LROs. During AXS measurements, the momentum transfer was fixed, while the scattering intensity was monitored when the x-ray energy was scanned through the elemental Fe-*K*, Pt-L_{III} and Ag-*K* absorption edges (7112, 11564 and 25514 eV, respectively).

The EXAFS data were also collected on the beamline 20-I of PNC-CAT, APS, Argonne National Laboratory. For the FePt samples, the data was collected with fluorescence mode. The data collection for the standard Fe, Pt and Ag foils used transmission mode. All the data was collected at room temperature. The data was analyzed using UWXAFS package.[101-105] Theoretical parameters used in the curve-fitting analysis were calculated by FEFF6.[105,107]

4.2 Structural and magnetic properties

The thickness effects on film LRO were compared with XRD to ensure that the alloying in thicker films was similar to that of 20 nm thickness. The XRD spectra of $(FePt)_{70}$-Ag_{30} samples with different thickness were shown in Fig. 4-2. The position of FePt(001) and (200) peaks did not show any difference with the variation of film thickness. Using log scale, the FePt(001)/FePt(200) intensity ratio remained the same, indicating the same texture for the films. The Ag peak remained unobservable in the spectra with larger film thickness. The relatively stable LRO justified the alloying study with thicker films.

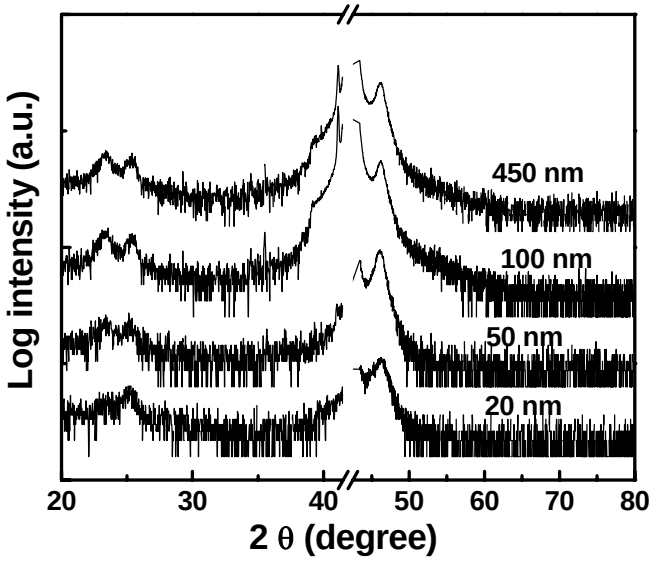

Figure 4-2 XRD spectra for $(FePt)_{70}$-Ag_{30} thin films with different thickness on MgO(200) substrate.

In addition, M_s, as intrinsic magnetic property originating from electronic and crystal structure, can be an indicator of alloying. In another word, M_s is close correlated to the miscibility of magnetic materials. The 450 nm FePt films on MgO substrates

showed similar value of saturation magnetization (~800 emu/cc) and coercivity (2.0 kOe) as 20 nm FePt films on CrRu underlayer (Fig. 4-7). This suggested that MgO substrate

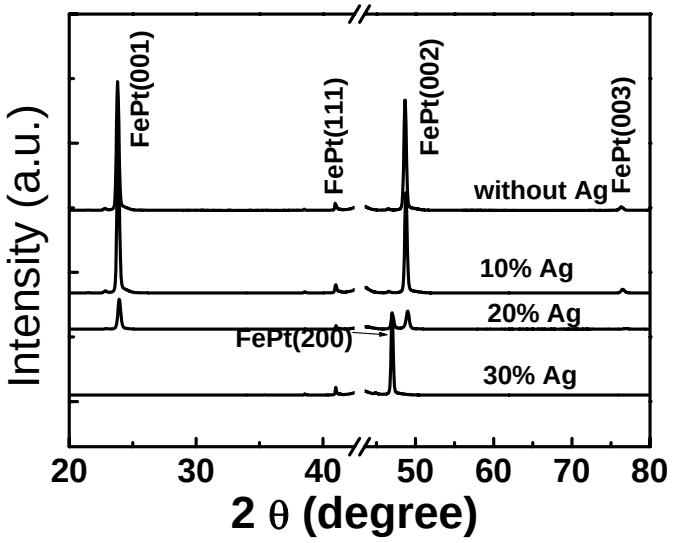

Figure 4-3 XRD scans of 450 nm FePt-Ag thin films cosputtered on MgO substrate at 350 °C

and higher thickness did not affect the alloying in the FePt thin films. It was therefore concluded that thicker FePt films deposited on MgO would be useful for studying the role of Ag using AXS and EXFAS.

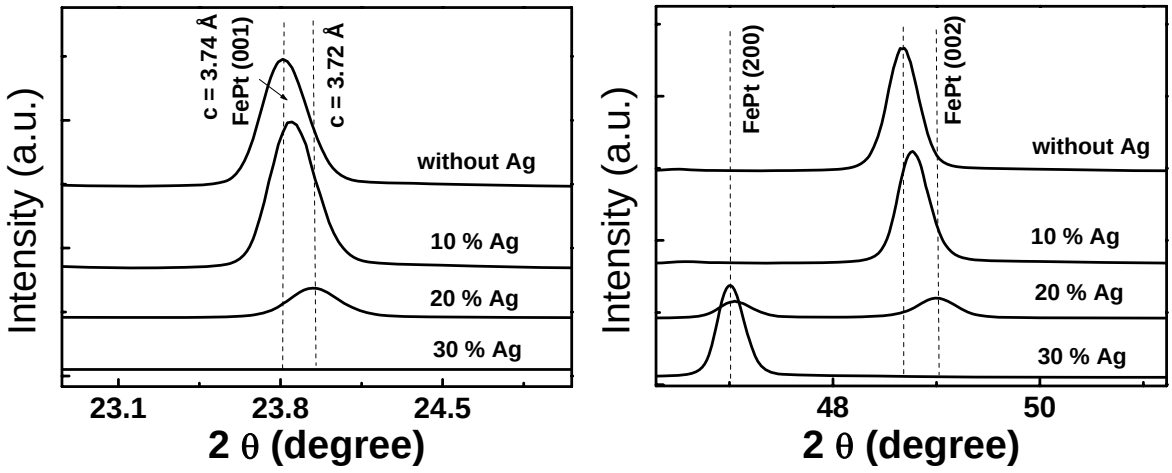

Figure 4-4 Shift of FePt(001) and FePt(002) peaks with increasing Ag fraction

In Chapter 3, cosputtering Ag with FePt on CrRu underlayer led to the longitudinal film texture. With MgO substrates and higher FePt-Ag thickness, similar texture evolution was observed. As shown in Fig. 4-3, pure FePt thin film epitaxially grew on MgO substrate, resulting in perpendicular FePt(001) and (002) texture in the XRD spectra. With Ag cosputtering, the dominant film texture changed to a longitudinal FePt(200). For the FePt thin film with 30 vol.% Ag, separate Ag peak was not observed.

Improved $L1_0$ ordering was reflected by the shift of FePt(001) and FePt(002) peaks to higher angles, which correlated to the decrease of lattice parameter *c*.

Table 4-1 RBS characterization on the global atomic compositions for the cosputtered FePt-Ag samples

Ag volume fraction (vol.%)	Atomic composition (at.%)		
	Pt	Fe	Ag
10	46. 3	47. 2	6. 5
20	43. 1	41. 4	15. 5
30	37. 2	38. 3	24. 5

Global atomic compositions of the samples were confirmed by Rutherford Back Scattering (RBS). The results listed in Table 4-1 indicated that Fe and Pt compositions were approximately equal.

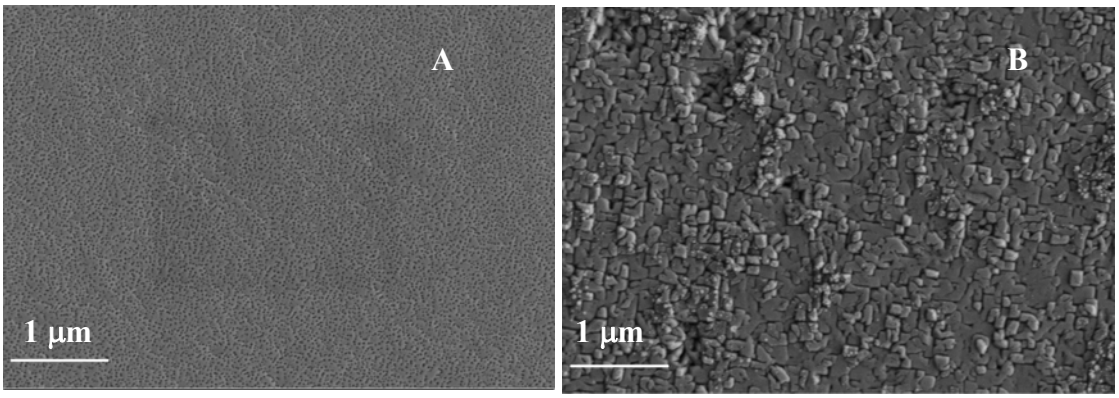

Figure 4-5 SEM images of FePt thin film A)without Ag and B)with 20 vol.% Ag.

Figure 4-5 showed the SEM images for the films without Ag and 20 vol.% Ag. The sample without Ag showed a continuous structure while the sample cosputtered with 20 vol.%Ag showed grain boundaries.

The Ag concentration distribution in the sample of 20 vol.% Ag was obtained from the XPS depth profile (Fig. 4-6). The concentration of Fe and Pt in the XPS data was calibrated with the RBS data. It is noted that Ag enrichment was observed on the film surface and its concentration in the film interior was only ~2 at.%. Although the concentration on sample surface was as high as 50 at.%, no separate Ag phase was shown in the XRD data (Fig. 4-3). Two reasons are possible:

1. Ag alloyed with FePt.

2. Small thickness or grain size was below the detection limit of XRD. Because of the deficiencies of XRD discussed previously, further investigation on the FePt-Ag alloying is necessary.

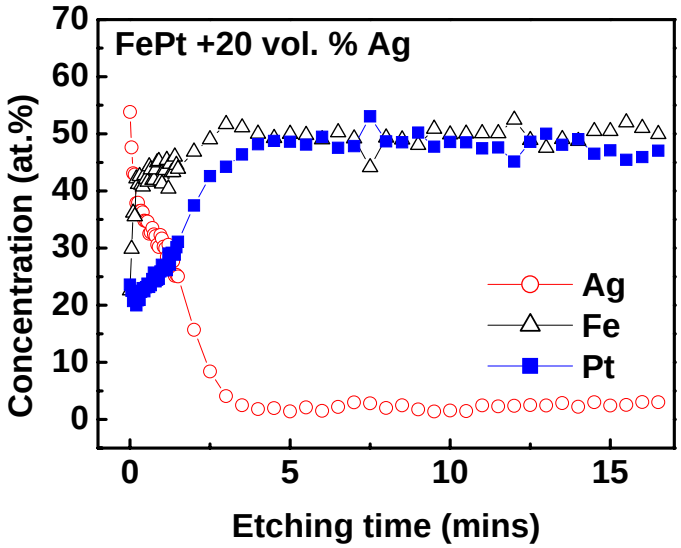

Figure 4-6 XPS depth profile of the cosputtered FePt-Ag thin film of 450 nm on MgO substrate

Figure 4-7 showed the in-plane and out-of-plane hysteresis loops of 450 nm FePt thin films without Ag and cosputtered with 30 vol.% Ag, respectively. The hysteresis loops suggested the change of magnetic easy axis from perpendicular to longitudinal direction, which was consistent with the XRD data in section 4.2.

Film coercivity also increased significantly when cosputtered with Ag. The coercivity enhancement was consistent with the result in Chapter 3.

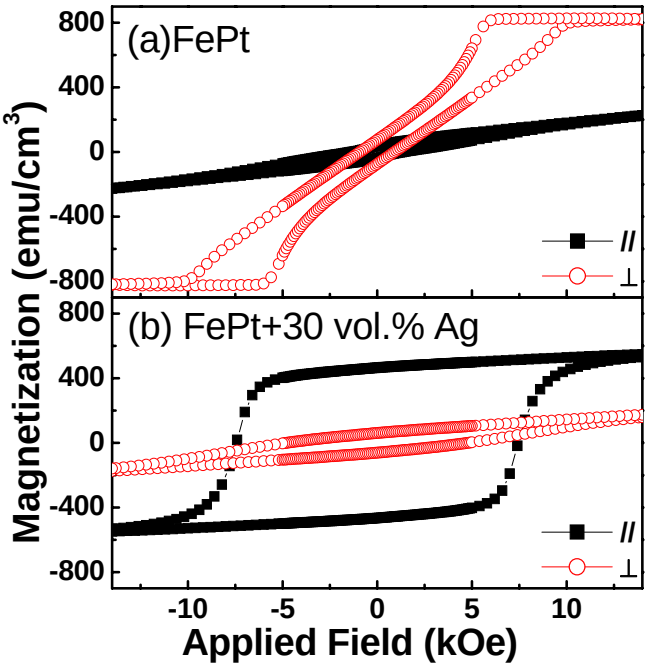

Figure 4-7 In-plane and out-of-plane hysteresis loops of 450 nm FePt thin films (a) without Ag (b) cosputtered with 30 vol.% Ag

4.3 Phase miscibility investigation with AXS

In x-ray diffraction, the scattering intensity is proportional to the squared form factor (Eq. 2-7). Based on the kinematical approximation assuming that the FePt-Ag is a random alloy, we have:

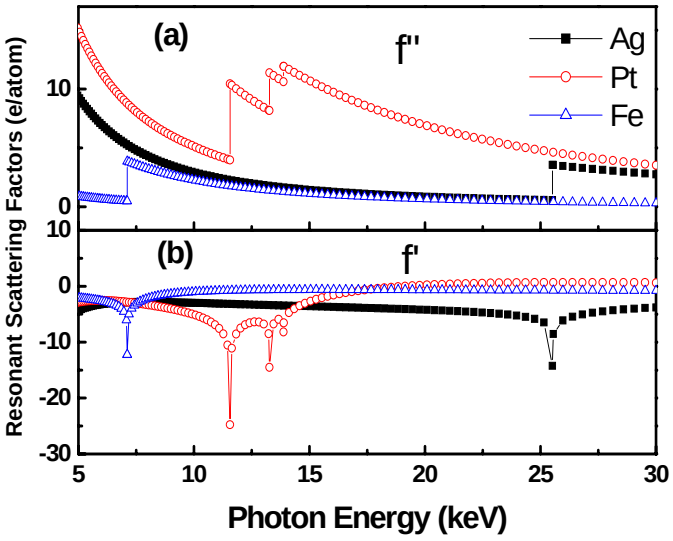

Figure 4-8 The anomalous atomic form factors of Fe *K*-, Ag *K*- and Pt *L* absorption edges, respectively. (a) imaginary part (f′); (b) real part (f″)

$$I(q,E) \sim \left| \chi_{Fe} f^{Fe}(q,E) + \chi_{Pt} f^{Pt}(q,E) + \chi_{Ag} f^{Ag}(q,E) \right|^2 \qquad \textbf{(4-1)}$$

where $I(q,E)$ is the scattering intensity; χ_{Fe}, χ_{Pt}, and χ_{Ag} are elemental concentrations at the specified Bragg reflection, respectively. $f^{Fe}(q,E)$, $f^{Pt}(q,E)$ and $f^{Ag}(q,E)$ are the atomic form factors of Fe, Pt and Ag respectively.

The atomic scattering factors consist of non-resonant Thomson scattering factor f^0 and anomalous scattering factor Δf. And Δf is a complex function composed of a real part (f′) and an imaginary part (f″).

Figure 4-8 shows the real part and imaginary parts of Fe, Pt and Ag anomalous scattering factors.[108] The anomalous scattering factors change dramatically near the absorption edges. The two parts are related to each other through the Kramers relation.

If the element in question is associated with the Bragg peak, the elemental absorption causes a decrease in the diffraction intensity, and a cusp appears at its

absorption edge.[98] Assuming Ag atoms replace the Fe and Pt atoms randomly, simulation results of the scattering intensities for FePt-Ag crystals with different Ag concentrations based on Eq. 4-1 are shown in Fig. 4-9.

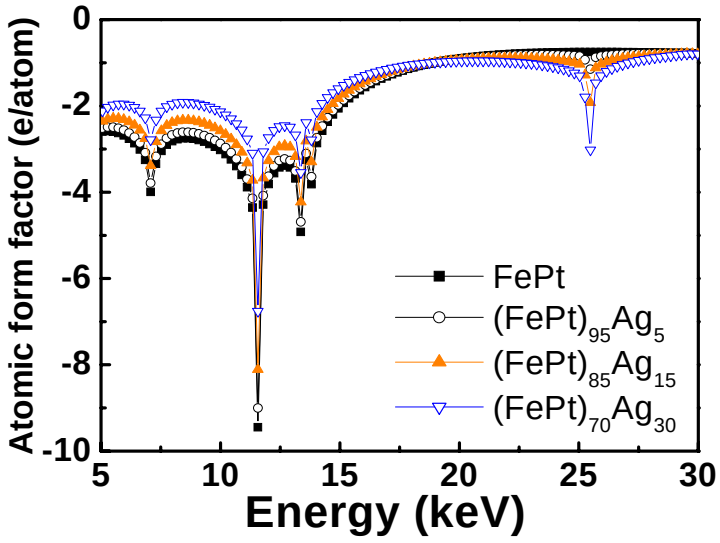

Figure 4-9 Simulated anomalous atomic form factors with various Ag atomic concentrations alloyed with FePt. Ag atoms were assumed to replace the Fe and Pt atoms randomly

The simulation used the data library reported in Ref 108. The results indicated that the depth of the cusp at particular absorption edge depended on the concentration of the element in the LRO. A higher concentration of the element in the LRO corresponds to a deeper cusp at the relevant absorption edge. Absence of cusp at the related absorption edge indicated that the specific element did not reside in the LRO. Therefore, the alloying between Ag and FePt can be characterized by investigating the AXS spectrum near Ag absorption edge.

AXS represents the elemental absorption in specific LRO. Unlike normal θ-2θ scan XRD, the LRO peak in AXS test is fixed. Therefore, the LRO of interest is represented by the moment transfer in reciprocal space, defined as $q = 2k\sin\theta$ ($k = 2\pi/\lambda$)

= 2π/d. The AXS scans to FePt(001) reflection (q = 1.695 Å^{-1}) for the pure FePt sample is shown in Fig. 4-10. The absorption cusp near the Fe-K, and Pt-L_{III} edges indicated the alloying of Fe and Pt. For this sample without Ag, the absence of absorption cusp near Ag-K edge was consistent with the simulation result in Fig. 4-9.

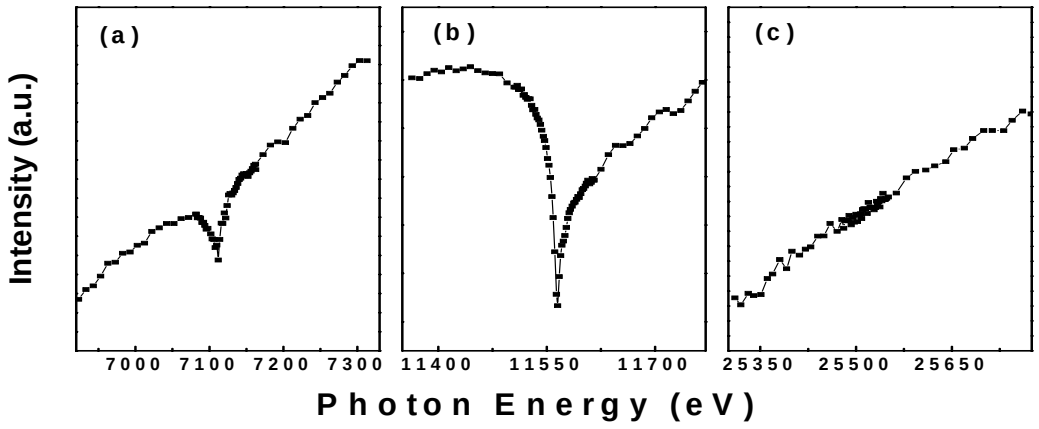

Figure 4-10 AXS scans near (a) Fe-K, (b) Pt-L_{III} and (c) Ag-K edges for the FePt thin film (without Ag) deposited on MgO(100) substrate. q was fixed at FePt(001) peak

Similar AXS scans were conducted for the FePt sample cosputtered with 20 vol.% Ag (Fig. 4-11). In addition to the absorption cusps near Fe K and Pt L_{III} edges, an

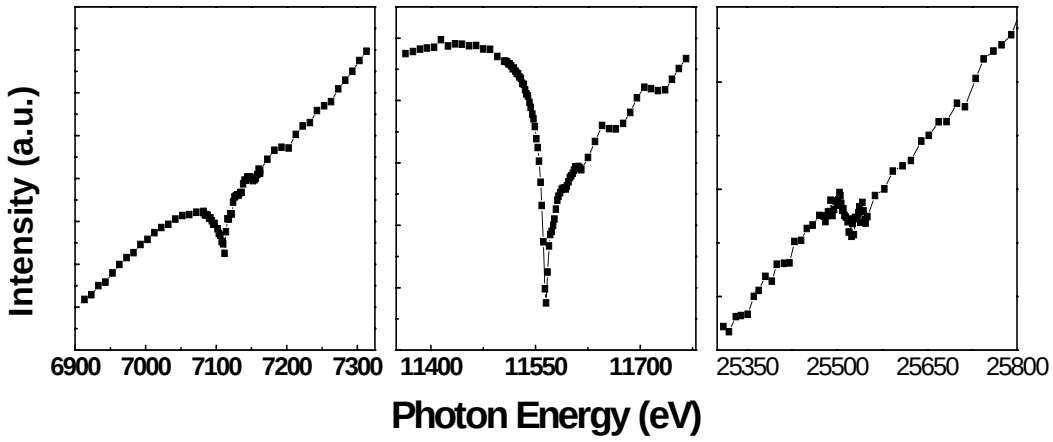

Figure 4-11 AXS scans near (a) Fe-K, (b) Pt-L_{III} and (c) Ag-K edges for the FePt thin film cosputtered with 20 vol.% Ag on MgO(100) substrate. q was fixed at FePt(001) peak

absorption cusp near the Ag K edge was observed, indicating the existence of Ag in the FePt(001) LRO.

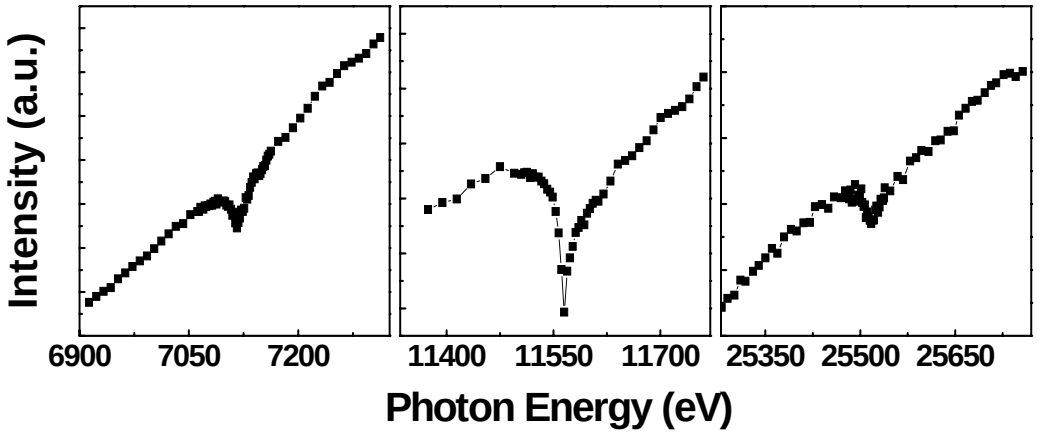

Figure 4-12 AXS scans near (a) Fe-*K*, (b) Pt-L_{III} and (c) Ag-*K* edges for the FePt thin film cosputtered with 30 vol.% Ag on MgO(100) substrate. *q* was fixed at FePt(200) peak

When the Ag volume fraction increased to 30 vol.%, the FePt film texture changed from perpendicular FePt(001) to longitudinal FePt(200) as shown in Fig. 4-3. Accordingly, the moment transfer was fixed at the FePt(200) reflection (q = 3.254 $Å^{-1}$) for the AXS measurement. The AXS spectra are shown in Fig. 4-12. The absorption cusp appeared near the Ag *K* edge confirmed that Ag atoms resided in FePt(200) LRO.

Simulations based on Eq. 4-1 showed that the cusp intensity increased with increasing alloying fraction in the films. This relationship can be used to characterize the alloying fraction in textured samples. The miscibility of Ag in FePt was further studied by fitting of the AXS spectra. For comparison, a 450 nm pure Ag thin film was sputtered on MgO single crystal substrate at 350 °C. The small lattice mismatch (2.85%) between MgO(200) and Ag(200) resulted in good Ag(200) texture, which was favorable for AXS test. The AXS spectra of FePt-Ag thin films after background subtraction were compared to that of the pure Ag thin film (Fig. 4-13).

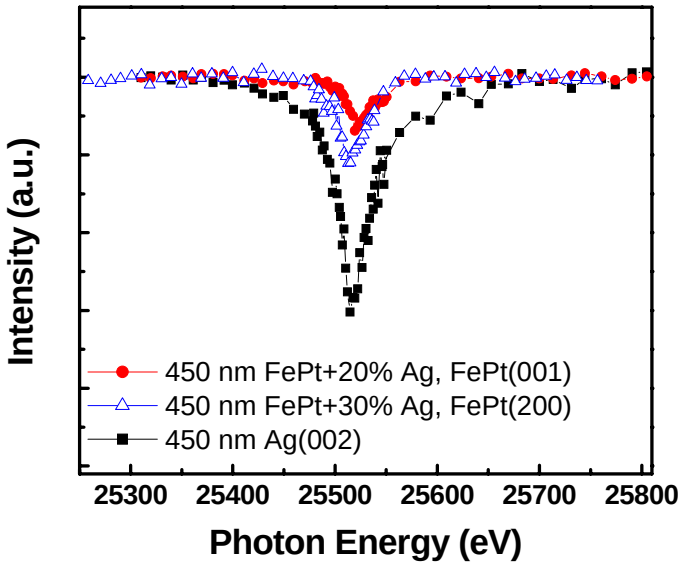

Figure 4-13 Ag *K* edge AXS spectra of 450 nm thin films for sputtered Ag, FePt+20 vol.%Ag and FePt+30 vol.% Ag. The AXS spectra were measured at Ag(002), FePt (001) and FePt(200), respectively

Since the part of AXS spectrum near the elemental absorption edge mainly arises from anomalous (resonance) scattering, the variation of non-resonant Thomson scattering factor can be ignored.

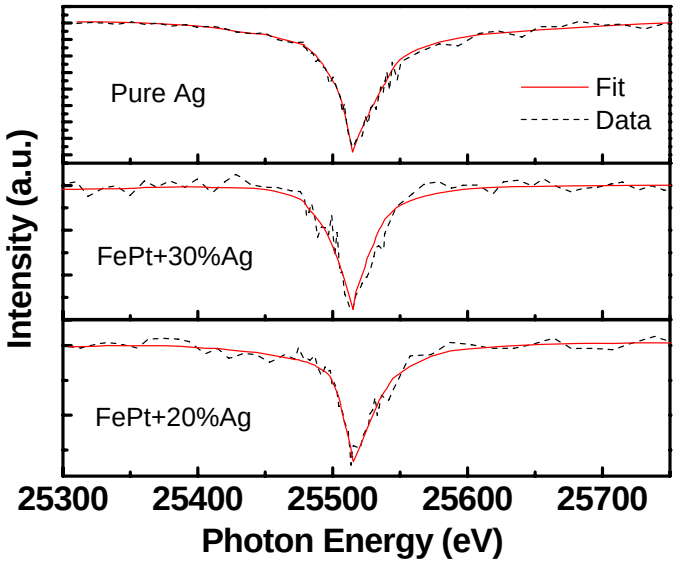

Figure 4-14 Ag-*K* edge fitting of AXS data of 450 nm Ag thin film and 450 nm FePt thin films co-sputtered with 20 vol.% and 30 vol.% Ag

We assumed that the AXS absorption cusp near Ag *K* edge at the position of FePt(200), FePt(001) and Ag(002) had same scaling factor in Eq. 4-1. The scaling factor was determined by fitting the data of the pure Ag sample with Eq. 4-1.

With the determined scaling factor, the Ag-*K* edge AXS spectra of the FePt-Ag samples with 20 vol.% and 30 vol.% Ag were fitted with Eq. 4-1, respectively, to estimate the Ag alloying fractions in the cosputtered FePt-Ag thin films. The fitted results are shown in Fig. 4-14.

The fitting result of Ag concentration for the FePt thin films co-sputtered with 20 vol.% and 30 vol.% Ag was summarized in Table 4-2. The miscibility of Ag in FePt lattice (χ_{Ag}) is relatively lower than the global Ag composition obtained by RBS, indicating that most Ag segregated from FePt.

Table 4-2 AXS fitting result of Ag-*K* edge for the 450 nm FePt-Ag thin films

Sample	χ_{Ag} (at.%)	ChiSquared
FePt+20 vol.%Ag	4.21±0.35	1.40
FePt+30 vol.%Ag	5.85±0.27	2.43

By means of above AXS analysis, the alloying between Ag and FePt in the cosputtered FePt-Ag thin films was confirmed. As discussed previously, the big size of Ag atom is unfavorable for it to reside in the interstitial sites of FePt alloy. According to the Hume-Rothery Rules, substitutional FePt-Ag alloy remain possible, because:

- Although the relative atomic size between Fe and Ag is 16.1% (>15%), the difference between Pt and Ag is much smaller (4.2%).
- The electronegativity of Ag (1.93) is between that of Fe (1.83) and Pt (2.28), and closer to that of Fe.

- Although Fe and Ag have different crystal structure, Pt and Ag are all *fcc* structure.

4.4 Local atomic environment investigation with EXAFS

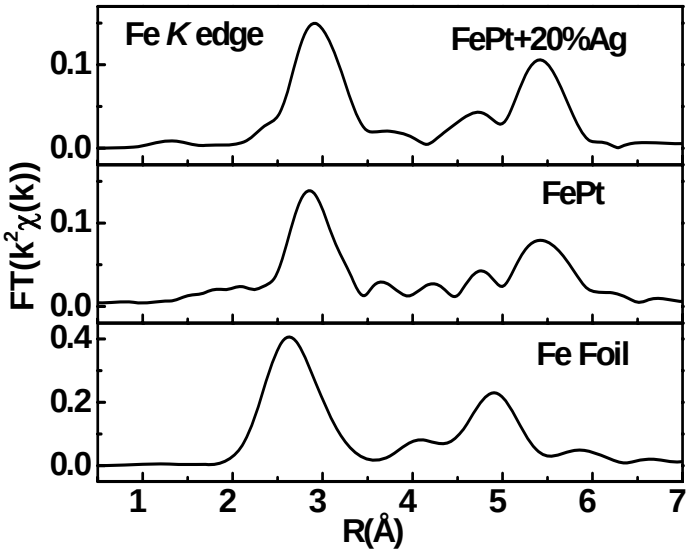

Figure 4-15 Fourier transfer of the Fe *K* edge EXAFS spectra of Fe foil standard, pure FePt and the FePt sample cosputtered with 20 vol.% Ag

Ag alloying and miscibility in FePt thin films was characterized with AXS in section 4.3. However, it cannot be determined whether Ag substituted Fe or Pt by means of AXS. In order to further study the microstructure and local atomic environment in cosputtered FePt-Ag films, EXAFS analysis was conducted on the same samples discussed in section 4.3.

After background subtraction, EXAFS data was transformed to a function of photoelectron wave number *k*. Since EXAFS amplitude generally falls off with increasing *k*, Fourier transforms of EXAFS spectra to R space were done using k^2 weighting up to $k_{max} = 15$ Å^{-1}. Fourier-transformed Fe *K* edge EXAFS data was compared in Fig. 4-15.

While the first neighboring shell of the Fe foil was located at 2.62 Å, the FePt sample cosputtered with 20 vol.% Ag resembled the pure FePt sample in terms of the first coordinate shells position at 2.92 Å, corresponding to the Fe-Pt bond length. Compared with pure FePt sample, fewer oscillating peaks for the cosputtered FePt-Ag sample suggested a decreased ordering and smaller particles.

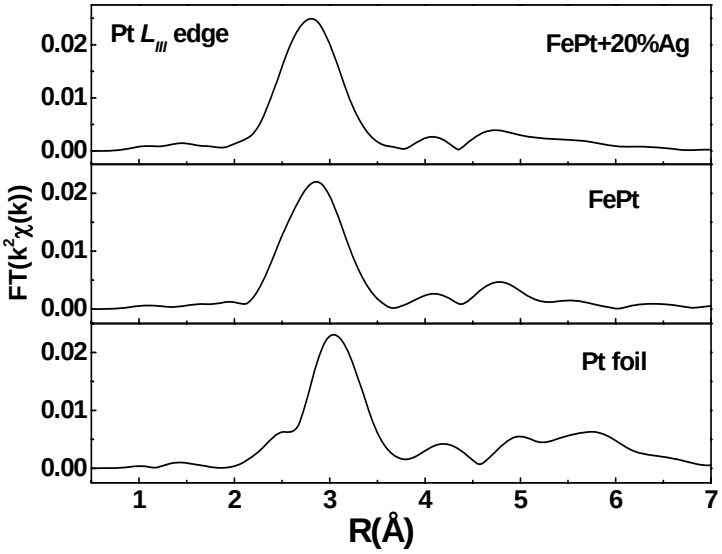

Figure 4-16 Fourier transfer of the Pt L_{III} edge EXAFS spectra of Pt foil standard, pure FePt and the FePt sample cosputtered with 20 vol.% Ag

The similarity between the FePt-Ag and FePt samples was also reflected in the Fourier-transformed EXAFS data at Pt L_{III} edge (Fig. 4-16). This result indicated that FePt structure did not change significantly when cosputtered with Ag. While the alloying between FePt and Ag was evident from the AXS results, the small change in FePt structure reflected by EXAFS suggested that Ag solubility in FePt lattice was low or the majority of Ag was segregated from FePt. Because of the low Ag concentration (2-3 at.%) in the film interior as observed previously in XPS (Fig. 4-6), it is possible that the

miscibility between Ag and FePt at the deposition temperature was less than 5 at.%, if taking the XPS resolution (~2 at.%) into consideration.

The low FePt-Ag miscibility was confirmed in previous AXS analysis that showed 4-6 at.% Ag in FePt lattice for the samples with 20 vol.% and 30 vol.% global Ag concentrations.

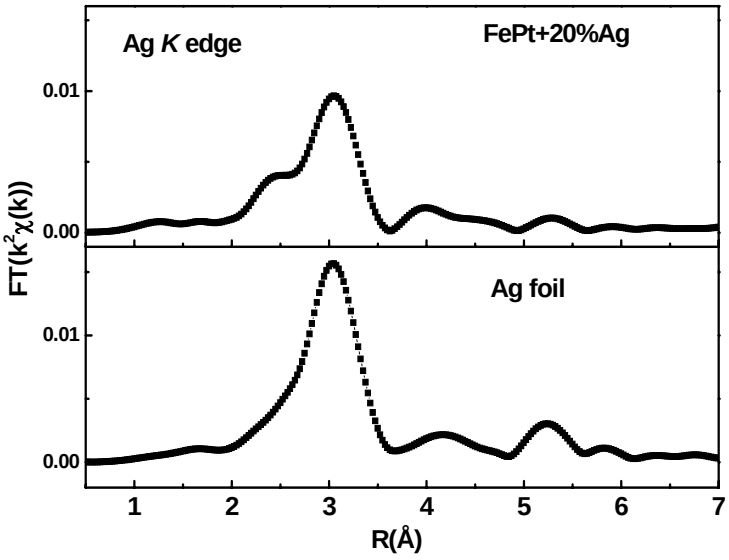

Figure 4-17 Fourier transfer of the Fe *K* edge EXAFS spectra of Ag foil standard and the FePt sample cosputtered with 20 vol.% Ag

At Ag *K* edge, the FT of the FePt-Ag EXAFS data showed some difference from that of Ag foil standard (Fig. 4-17). As the amplitude of FT spectrum is an indicator of short-range order (SRO), the lower FT amplitude of the first neighboring shell of the FePt-Ag sample indicated that the Ag atoms were very disordered. In addition, a shoulder at lower R perhaps resulted from the Ag-Fe coordination, which was shorter than Ag-Ag.

In order to further clarify the local structure around Ag atoms, fitting of EXAFS spectra was conducted. We first fitted the EXAFS data from Ag foil with a standard EXAFS analysis process.[109] A theoretical $\chi(k)$ was constructed whose adjustable

structural parameters r_i ,N_i , σ^2 were refined against the experimental data by nonlinear least squares minimization of the statistical chisquare χ^2:

$$\chi^2 = \sum_{i=1}^{N} (\chi^{ex}(r_i) - \chi^{th}(r_i))^2 \quad \textbf{(4-2)}$$

where χ^{ex} and χ^{th} are experimental and theoretical values, respectively.

Small R factor (< 0.02) is an important criteria for a good fit. The R factor is defined as:

$$R\_factor = \frac{\chi^2}{\sum_{i=1}^{N} \chi^{ex}(r_i)^2} \quad \textbf{(4-3)}$$

In fitting refinement, correlation between parameters should be less than 85% and the fitted uncertainty should be at least one order of magnitude lower than the parameter value.

A fit with a fully occupied fm3m model up to 4 Å well agreed with the crystalline structure of Ag bulk. From the best fitting on the Ag foil data, the passive electron reduction factor S_0^2 for Ag edge, which is an empirical amplitude correction factor parameter taking into account many-body losses in the photo absorption process, was determined as 0.81. This value was fixed in the fitting for the FePt-Ag sample.

Setting the central absorber as Ag atom, we attempted to use FePt $L1_0$ structure (space group P4/mmm) to fit the Ag-*K* edge EXAFS data of the cosputtered FePt-Ag sample with 20 vol.% Ag. However, we could not obtain a satisfactory fit to the EXAFS data. This suggested that the local environment of Ag atoms in the sample was much different from FePt lattice structure. The difference reflected in EXAFS spectra is

consistent with previous conclusion of low Ag solubility in FePt, because EXAFS represented the averaged SRO information of the whole sample.

However, when fitting the EXAFS Ag K edge data of the FePt-Ag sample with fcc Ag structure (space group fm3m), the best fitting showed acceptable fitting with R factor of 0.03, which is close to our criteria of 0.02. Fitting spectra are shown in Fig. 4-18(a). The coordination number of Ag for the FePt sample with 20 vol.% Ag is ~6.9 with this model, much lower than the value of foil standard, indicating that Ag was very disordered in the FePt film.

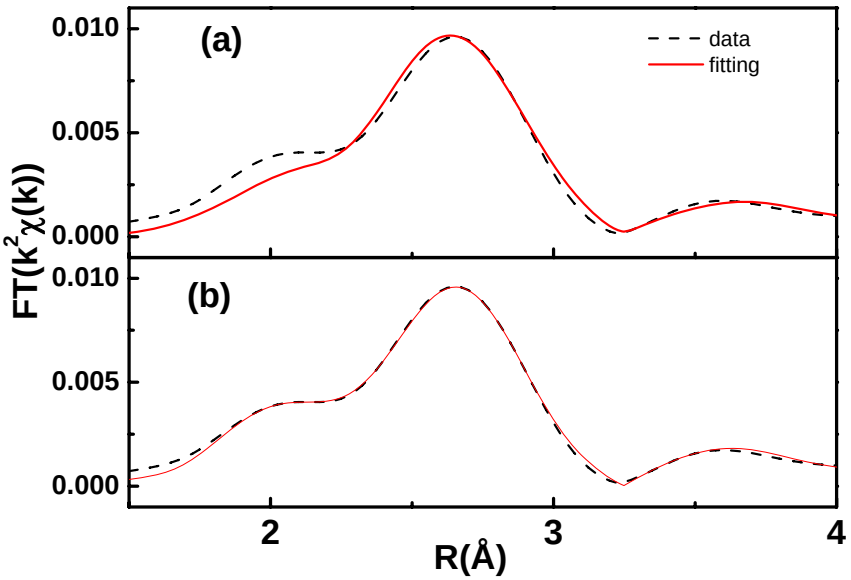

Figure 4-18 Fitting of the FePt-Ag (20 vol.%Ag) sample with (a) fcc Ag model only; (b) adding a scattering path of Ag-Fe in the *fcc* Ag model

This result suggested that most Ag atoms in the film were segregated Ag *fcc* structure. Only a small portion of Ag alloyed with FePt as shown in AXS. The absence of separate Ag peak in the XRD data may result from the close lattice parameter between FePt and Ag, small grain size or poor LRO of Ag.

In the effort to refine the fitting, the scattering paths in FePt structure were calculated with FEFF after the substitution of scattering Fe (or Pt) with Ag. The newly

generated scattering paths were then added into the *fcc* Ag model. In the followed EXAFS fitting, a 10:1 weighting was applied to the *fcc* Ag paths and the calculated Ag-Fe/Ag-Pt, considering that the majority of Ag atoms were in separate Ag phase. In this way, the fitting was refined with the combination of *fcc* Ag and Ag-Fe scattering path. The fitting result was shown in Fig. 4-18(b). The fitting results are summarized in Table 4-3.

Table 4-3 Fit parameters of the first cell around an Ag absorber for the FePt-Ag (20 vol.%Ag) sample. *k* weight is 2. The S_o^2 was fixed at 0.81 as in bulk Ag. N is the coordination number, R is the bond length of the nearest neighboring atoms, and δ^2 is the Debye-Waller factor that serves as a measure of local disorder

	Model A	**Model B**		**Model C**	
Coordination	Ag-Ag	Ag-Ag	Ag-Fe	Ag-Ag	Ag-Pt
N	7.414± 0.89	5.86±0.33	1.52±0.14	3.54±0.22	2.83±0.34
R (Å)	2.87±0.04	2.86±0.06	2.13±0.05	2.76±0.04	2.68±0.07
δ^2 ($\times 10^{-3}$ Å^2)	1.2±0.8	3.2±0.6	4.2±0.6	6.3±0.5	3.5±0.5
R factor	0.03	0.02		1.56	

Model A: fcc Ag model
Model B: Model A + Ag/Fe replacing in FePt model
Model C: Model A + Ag/Pt replacing in FePt model

Because the EXAFS data fitting by model B showed lower R factor and smaller uncertainty, the model B was likely to be a better reflection of the local environment of Ag in the FePt-Ag sample. Therefore, some Ag atoms replaced the Fe sites in FePt lattice. In another point of view, the mixing enthalpy of Fe-Ag and Pt-Ag is $\Delta H_{mix(Fe\text{-}Ag)} >> 0$, and $\Delta H_{mix(Pt\text{-}Ag)} < 0$, Ag is unlikely to occupy the Pt site in the $L1_0$ lattice, so $L1_0$ FePt with Ag would be (Fe, Ag)Pt.

Since the weighting ratio given to Ag-Ag and Ag-Fe paths was 10:1 in the fitting, the alloying by Ag/Fe replacement was small. With 5:1 weighting for Ag-Ag and Ag-Fe paths in the same model B, the fitting failed to achieve satisfactory good fit, indicating

that high Ag alloying was unlikely. Therefore most Ag was in a segregated phase. This was consistent with the low miscibility in previous AXS analysis.

It is noted that the Ag coordination number in the fitting by all the A, B and C models were much lower than the theoretical value of 12, indicating a very disordered SRO of Ag. As previous analysis, three phases of Ag coexisted in the cosputtered FePt-Ag thin films: the separated crystalline phase, the disordered phase in grain boundaries and the phase in FePt lattice. The poor Ag ordering in the later two phases can explain the low coordination numbers in the EXAFS fitting, because EXAFS is a reflection of average information for the whole sample.

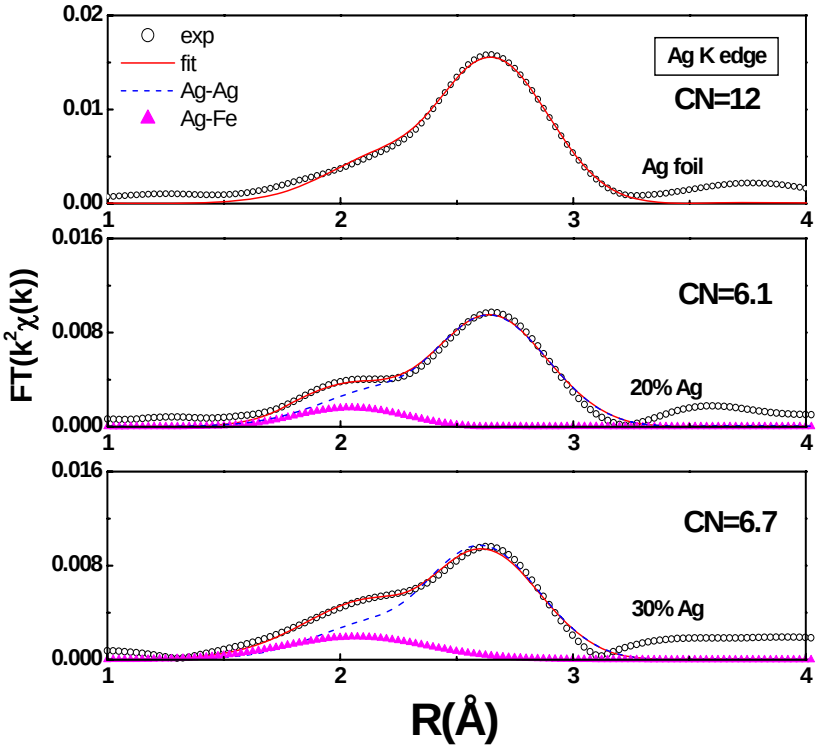

Figure 4-19 Experimental spectra and corresponding fitting curve with scattering path components for the FePt-Ag thin films on MgO substrate

In order to estimate the Ag alloying fraction, Ag-*K* edge EXAFS spectra of the FePt thin films with 20 vol.% and 30 vol.% Ag were further fitted with the model B,

respectively. The fitting was conducted to the first neighboring shell. The weighting constraint for Ag-Ag and Ag-Fe scattering paths was relaxed in the fitting. As obtained in Table 4-3, the δ^2 values for Ag-Ag and Ag-Fe scattering paths were fixed at 3.2×10^{-3} Å^2 and 4.2×10^{-3} Å^2, respectively. Individual contribution to the fitted EXAFS spectra by Ag-Fe scattering path was assumed to be proportional to the fraction of Ag-Fe replacement.

Figure 4-19 showed the experimental and fitting curves for the films. Our EXAFS fitting showed that the alloyed Ag fractions for the samples with 20 vol.% and 30 vol.% Ag were about 4.45 at.% and 6.48 at.%, respectively. The low Ag miscibility in FePt was consistent with previous XPS and AXS analysis, although the values were slightly higher than those obtained by AXS fitting. Note that the composition analysis by AXS only applied to a particular (*hkl*) peak, whereas the composition analysis from EXAFS referred to the average global composition. The Ag-Ag coordination number remained low for the two samples. Compared the sample with 20 vol.% Ag, the slightly higher Ag-Ag coordination number for the sample with 30 vol.% Ag suggested better Ag ordering with increasing Ag fraction.

Table 4-4 Fitting results with Model B for the FePt samples with 20 vol.% and 30 vol.% Ag. *k* weight is 2. δ^2 values were fixed with the results in Table 4-3

Sample	**FePt+20 vol.%Ag**		**FePt+30 vol.%Ag**	
Coordination	Ag-Ag	Ag-Fe	Ag-Ag	Ag-Fe
N	6.14±0.43	1.19±0.18	6.72±0.28	2.62±0.24
R (Å)	2.86±0.05	2.09±0.06	2.87±0.05	2.11±0.06
Ag-Fe fraction (at. %)	4.45±0.96		6.48±1.53	
R factor	0.02		0.02	

In summary, Ag miscibility in FePt obtained by EXAFS fitting was comparable to the values by AXS fitting. It can be concluded that only small portion of Ag alloyed with FePt. Large portion of Ag was segregated from FePt.

Both AXS and EXAFS study showed low miscibility of Ag in FePt. However, the large portion of separate Ag was not reflected in XRD data by Ag peak. One reason may be that the small Ag crystal size was below the detection limit of XRD. In addition, the low coordination number in EXAFS analysis revealed poor Ag SRO, indicating that most Ag could be amorphous or resided in grain boundaries.

The FePt-Ag samples selected for alloying study have 20-30 vol.% Ag. It is unlikely that all the Ag atoms resided in the grain boundaries. Most of them either diffused out to the surface or existed as a second phase. Since the quench rate after sample deposition was very low, it was not able to form pure Ag metallic glass. It was likely that Ag formed an amorphous alloy or compound. Thermodynamically, Ag can form silver oxide (Ag_2O) by reaction with oxygen at room temperature, since the reaction has a negative standard free energy of formation of Ag_2O (ΔG_{298} = -11.2 kJ mol^{-1}) at room temperature. [110]

Based on the alloying information, the improved $L1_0$ ordering observed previous in cosputtered FePt-Ag thin films can be understood from two aspects: alloying and vacancy.

It is known that the melting temperature of FePt is higher than 1500 °C, whereas that of Ag is 961 °C. Although the miscibility between FePt and Ag is low based on the AXS and EXAFS result, the melting points of FePt alloy could be decreased by alloying with Ag, resulting in the enhancement of atomic mobility compared to the binary system. By accelerating the atomic diffusions, the ordering process could be promoted.

The promotion of $L1_0$ ordering with Ag addition may also be explained as follow: Ag has low solubility with both Fe and Pt. In addition, Ag has low surface energy that is

favorable for surface segregation.[111,86] When Ag is incorporated in FePt, it tends to diffuse out of FePt lattice upon heat treatment and segregated as Ag phase. This creates vacancies at the FePt lattice, since the atomic size of Ag is comparable to that of Fe and Pt. The A1-to-$L1_0$ phase transformation in FePt is a diffusion-based reaction by the vacancy mechanism. The activation energy can be described as the sum of the energy needed for the dissociation of constituting atoms for vacancy formation and the energy for the mobility of diffusing atoms. The activation energy value of 257-259 kJ/mol for the self-diffusion of Fe and Pt atoms was reported.[112] Lower activation energy of ~219 kJ/mol was reported in 10 at.% Ag-doped FePt nanoparticles.[113] If activation energy only depends on the contribution from the vacancy formation, a 15% reduction of activation energy in Ag-doped FePt resulted in ~66 times higher diffusion coefficient of Fe and Pt than that of pure FePt at 350 °C based on the following Arrhenius relationship:

$$D \propto X_{vac} \propto EXP(-Q_{vac}/RT) \quad \textbf{(4-4)}$$

where D is the diffusion coefficient of Fe and Pt, $X_{vac.}$ is the vacancy concentration, and Q_{vac} is the activation energy for vacancy formation. Hence the FePt $L1_0$ ordering can be enhanced with Ag doping due to the increased number of vacancies.

With the conclusion of the AXS and EXFAS analysis in this chapter and the coercivity mechanism analysis in section 3.3, a better understanding on the magnetic and structure properties of FePt-Ag thin films was obtained.

Firstly, a small fraction of Ag in the FePt lattice prevented a drastic deterioration of the intrinsic magnetic properties, such as K_u and M_s. Originated from the electron interactions and band structure, intrinsic magnetic properties are significantly influenced by the alloying and elemental distribution in crystal structure. Therefore, the main

advantages of $L1_0$ FePt alloy, high K_u and M_s, were maintained when cosputtered with Ag that showed low solubility in FePt. The high K_u and M_s are favorable for the application of $L1_0$ FePt thin film as magnetic recording media. Secondly, the majority of segregated disordered Ag phase provided both magnetic isolation and pinning sites, which was favorable for better magnetic SNR performance and higher coercivity, respectively.

4.5 Summary

By means of AXS, FePt-Ag alloying and miscibility in the cosputtered FePt-Ag film was characterized. This method overcome the deficiencies of conventional XRD and gave a direct identification of alloying in nanostructured thin film with good structure.

XPS data revealed the surface segregation of Ag and low Ag concentration in interior films. The absence of Ag reflection in XRD and TEM diffraction pattern could be due to the small grain size.

EXAFS analysis indicated that Fe was more likely replaced by Ag in the alloyed FePt-Ag system. By EXAFS fitting, the alloyed Ag fractions for the samples with 20 vol.% and 30 vol.% Ag deposited at 350 °C showed comparable values with those obtained by AXS fitting.

$L1_0$ ordering was enhanced when FePt alloyed with Ag. The ordering enhancement can be understood in terms of the melting point decrease caused by FePt-Ag alloying and vacancy-enhanced diffusion.

Chapter 5. Perpendicular FePt thin films with Ag insertion

In Chapter 3, cosputtered FePt-Ag thin films on CrRu underlayer showed favorable effects on magnetic properties, such as exchange decoupling and coercivity enhancement. However, cosputtering with Ag tended to form longitudinal FePt texture. Considering the advantages of PMR, it is desirable to maintain the FePt perpendicular texture. It was reported that sequential FePt deposition on Ag underlayer showed FePt(001) texture on Si[114] and MgO substrates[115] after annealing. The Ag underlayer not only promoted perpendicular FePt texture but also lowered the ordering temperature. The FePt(001) texture resulted from the small lattice mismatch (7.1%) between Ag(002) and FePt(002). This result suggested a method to achieve perpendicular FePt texture with sequential deposition. In this chapter, FePt/Ag/FePt sequential deposition on CrRu(002) underlayer at 350 °C was studied. An Ag insertion was expected to improve the magnetic properties by means of Ag pinning and decoupling effects observed in Chapter 3. Meanwhile, perpendicular texture was expected to be maintained considering the close lattice mismatch between Ag(002) and FePt(002).

5.1 Sample preparation and characterization

Samples of FePt(5nm)/Ag(*t* nm)/FePt(5 nm) were fabricated by DC magnetron sputtering. The sample structure is illustrated in Fig. 5-1. The nominal Ag thickness *t* was varied from 0 to 3nm. A 30 nm CrRu underlayer (for inducing FePt(001) texture) and a 4

nm Pt buffer layer were sequentially deposited on corning 7059 glass substrates prior to the deposition of FePt. The Ag layer was deposited between successive 5 nm FePt layers. The substrates were maintained at 350 °C during deposition. The base pressure prior to sputtering was 2 $\times 10^{-8}$ Torr. The deposition argon gas pressure used was 10 mTorr for FePt and Ag, and 3 mTorr for Pt and CrRu layers. 3-inch $Fe_{50}Pt_{50}$, Ag, Pt and $Cr_{90}Ru_{10}$ sputtering targets were used.

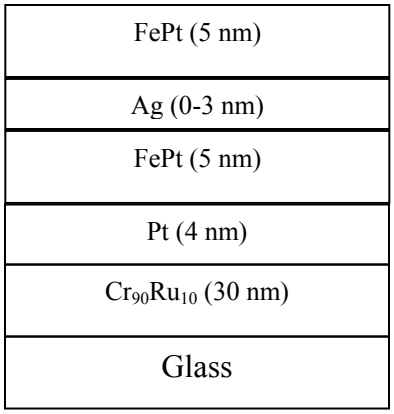

Figure 5-1 Structure illustration of the FePt/Ag/FePt thin films.

5.2 Structure and microstructure characterization

The XRD scans of the films are shown in Fig. 5-2. All the films showed perpendicular (001) texture. When Ag thickness exceeded 2 nm, the Ag(002) peak appeared, due to small lattice mismatch between FePt(002) and Ag(002). The Ag peaks suggested a separate Ag phase in the FePt films. The asymmetric FePt(002) peaks suggested the overlap of Ag(002), Pt(002), FePt(200) and FePt(002).

The increased broadening of FePt(001) peaks indicated the decrease of magnetic grain size with increasing Ag thickness. It is known that the grain size generally increases

with increasing film thickness. However, the inserted Ag layer disrupted the otherwise continuous growth of the film and reduced the grain size.

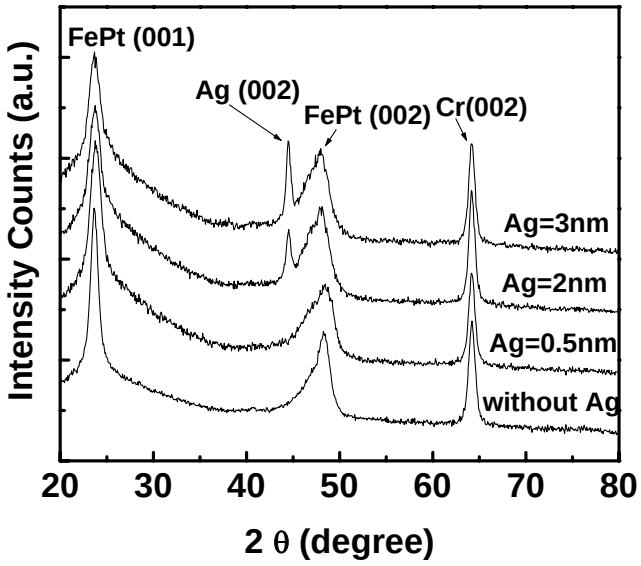

Figure 5-2 XRD scans of FePt films with various inserted Ag thickness

This was consistent with the TEM observations (Fig. 5-3), where the average magnetic grain size decreased from ~17 nm (without Ag) to ~5 nm (3 nm Ag layer).

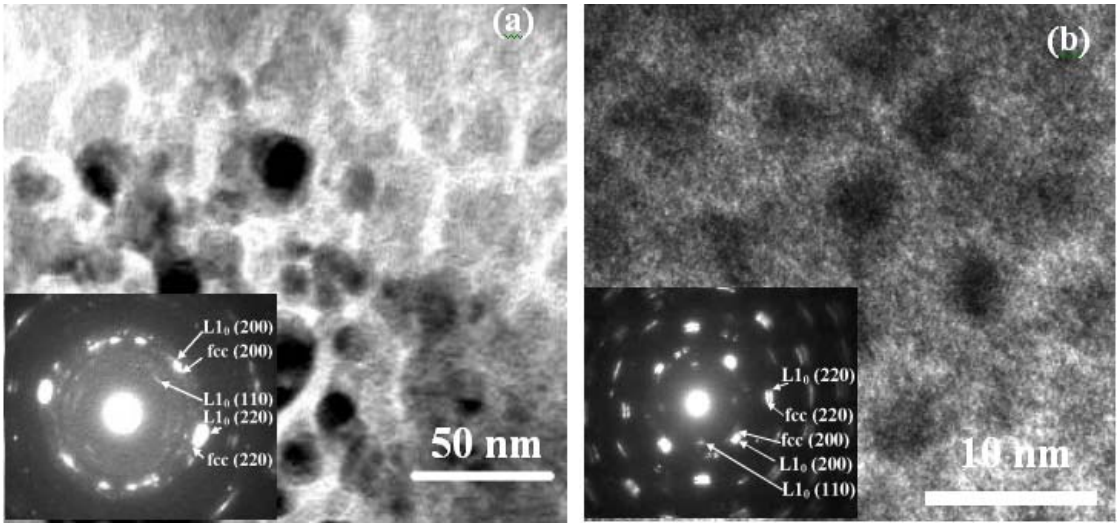

Figure 5-3 Bright-field TEM images of 10 nm FePt thin films (a) without Ag insertion and (b) with 3 nm Ag layer inserted, respectively. The insets are the selected area electron diffraction patterns

FePt(110) superlattice reflections shown in the selected area electron diffraction (SAED) patterns for both samples (insets in Fig. 5-3) confirmed the $L1_0$ ordering of FePt. However, both the samples showed distinct *fcc* (200) and $L1_0$ (200) reflections, indicating an incomplete ordering.

Figure 5-4(a) showed the cross-section TEM images of the FePt thin films with initial inserted 2 nm Ag. The Pt layer (dark contrast) and FePt layer (light contrast) are shown at higher magnification in Fig. 5-4(b). The fringes corresponded to the FePt(002) planes perpendicular to the film surface. It was induced by the CrRu (200) underlayer texture due to the lattice relationship FePt(002)[100]//CrRu(200)[110]. The continuous FePt(002) lattice fringe in Fig. 5-4(b) suggested the absence of continuous Ag layer.

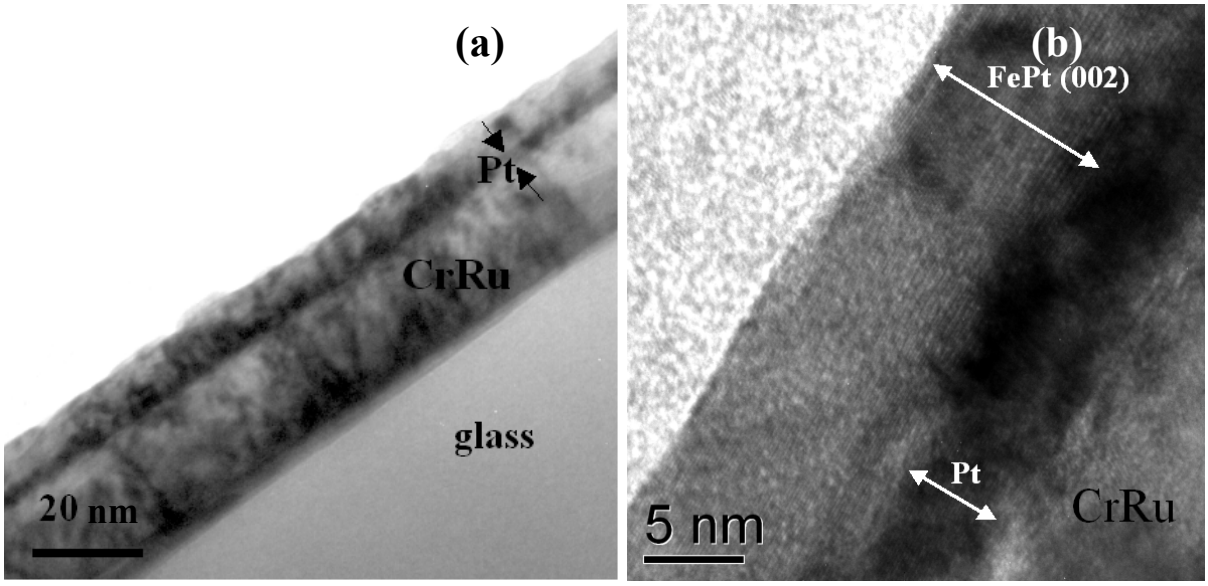

Figure 5-4 Cross-section TEM images of FePt thin film with 2 nm Ag inserted (a) bright-field (b) High-resolution image

In order to ensure that TEM image is able to identify the Ag continuous layer in between the FePt layers, a sample with the structure of FePt(5 nm)/Ag(2 nm)/FePt(5 nm)/glass but deposited at room temperature was studied by TEM (Fig. 5-5). The

continuous Ag layer could be clearly identified by the image contrast. Thus the absence of continuous Ag layer for the sample deposited at 350 °C suggested the Ag diffusion in the sample.

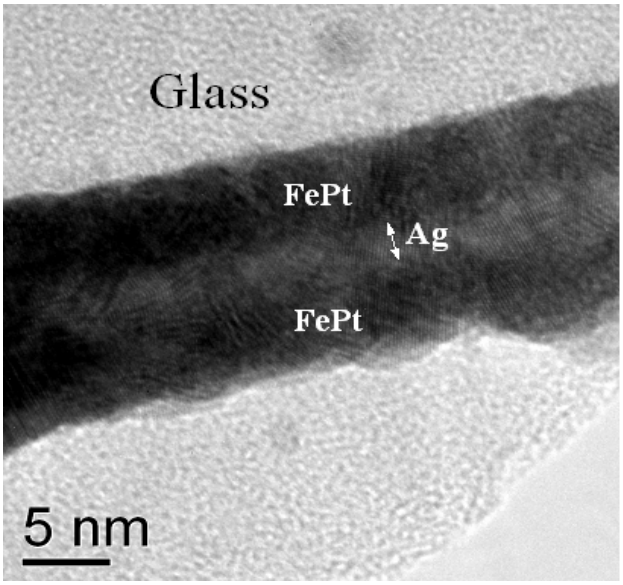

Figure 5-5 Cross-section TEM bright field image of FePt thin film with 2 nm Ag insertion deposited at room temperature on glass

5.3 Magnetic properties

Figure 5-6 showed the out-of-plane hysteresis loops of FePt films with different thickness of sandwiched Ag deposition. All the samples showed magnetic saturation. The perpendicular coercivity ($H_{c\perp}$) increased from 2 kOe (without Ag) to 4.4 kOe (with a 3 nm Ag sandwich layer). The hysteresis loop of the sample with a 0.5 nm Ag layer showed squareness (S) of 0.968 with a negative nucleation field, indicating a highly coherent magnetic reversal behavior. With further increase of Ag insertion, the slope of the hysteresis loop at H_c decreased, suggesting a decrease of exchange coupling.

The effects of Ag thickness on $H_{c\perp}$ and in-plane coercivity ($H_{c//}$) are shown in Table 5-1. $H_{c\perp}$ increased with increasing Ag thickness. The increase of $H_{c//}$ was less significant compared with $H_{c\perp}$. $H_{c//}$ also decreased noticeably when Ag thickness increased from 2 nm to 3nm. The ratio of $H_{c\perp}$ to $H_{c//}$ increased monotonically with increasing Ag thickness, indicating the improvement of perpendicular anisotropy.

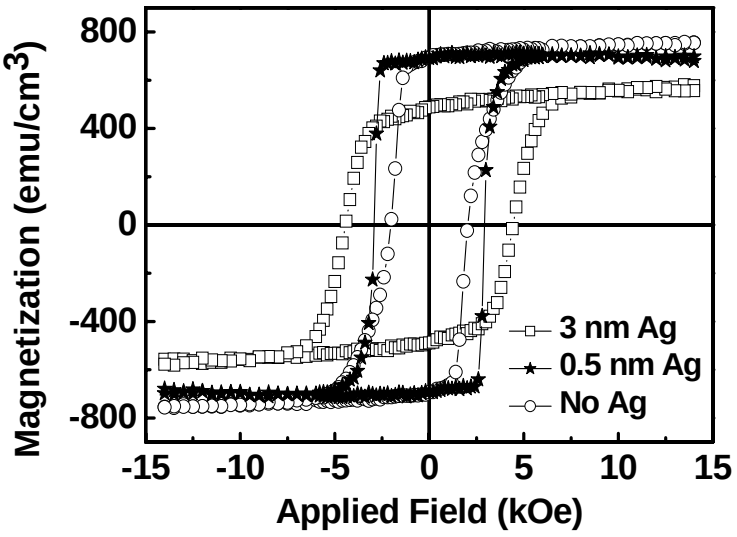

Figure 5-6 Out-of-plane hysteresis loops of FePt films with various inserted Ag thickness

In TEM observation (Fig. 5-3), the average FePt grain size was well below the critical single-domain size for FePt particles (~300 nm)29 and grain size was reduced with the Ag insertion. The increased coercivity with decreasing magnetic grain size due to increased Ag thickness suggested that other factors such as the degree of ordering and magnetic reversal mechanisms were involved.

Table 5-1 Out-of-plane coercivity ($H_{c\perp}$), in-plane coercivity ($H_{c//}$) and the ratio of $H_{c\perp}$ to $H_{c//}$ for 10 nm FePt films with various inserted Ag thickness

Ag Thickness	$H_{c\perp}$(Oe)	$H_{c//}$(Oe)	$H_{c\perp}$/ $H_{c//}$	M_s (emu/cm^3)
0	1960	1281	1.53	761
0.5	2923	1812	1.61	719
2	4003	1824	2.20	627
3	4440	1485	2.99	578

The pinning effect of Ag was reflected in the virgin magnetization curves (Fig. 5-7). With increasing Ag thickness, the steep increase of magnetization occurred at a larger field value, indicating a stronger domain wall pinning effect introduced by thicker Ag layer.

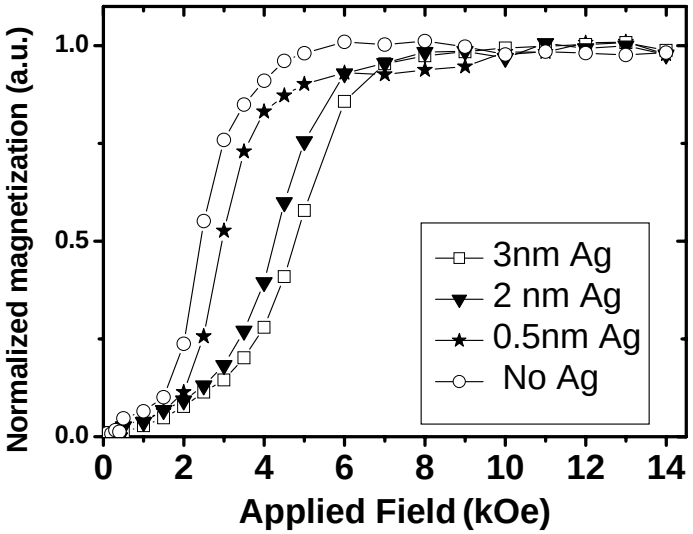

Figure 5-7 Virgin curves of samples with different Ag thickness

The peak position in the first derivative of the virgin curves refers to the maximum increase rate of magnetization under external field (Fig. 5-8).

The pinning effect decreased with decreasing Ag thickness, and the domain wall would expand and propagate easily through the magnetic grains. As a result, rapid increase of magnetization process occurred at low external magnetic fields. With increasing Ag thickness, the pinning field became stronger and the motion of domain wall would be retarded. The bowing or reversible movement of domain wall resulted in a slower increase of magnetization until a higher critical external field was reached to overcome the pinning effect. Beyond this critical field, irreversible magnetization dominated, resulting in a rapid increase in magnetization.[116,117]

To further investigate the Ag distribution, the XPS depth profile was measured for the FePt film with 2 nm sandwiched Ag. A standard sample of $Fe_{40}Pt_{60}$ was used to calibrate the Fe and Pt concentration. Note that Ag was found with high concentration (>30 at.%) near the film surface (Fig. 5-9). From the surface toward the film interior, the concentration of Ag showed a continuous decrease, which was not expected from a presumed sandwiched layer. These results showed that Ag had been dispersed throughout the film, instead of forming an uninterrupted layer sandwiched between two FePt layers, as would have been suggested by the sequential deposition of FePt and Ag layers.

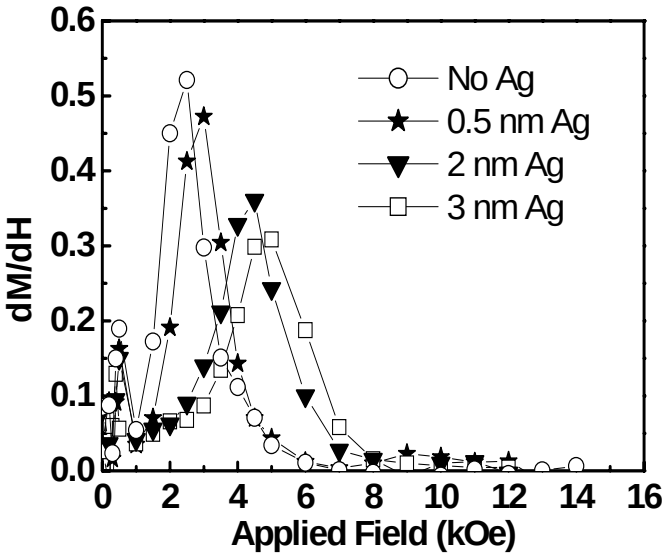

Figure 5-8 First derivative analysis on the virgin curves of the samples with different Ag thickness

The diffusion of Ag occurred after its deposition between the depositions of FePt layers. The driving forces for the surface enrichment of Ag are the surface energy and elastic strain energy. The kinetics of surface segregation can be described in terms of semi-infinite solution of Fick's equations and the application of the grain boundary formula obtained by McLean.[118] Generally, the lower the surface energy of the element, the higher the probability its segregation to the surface.[119] The values of surface energy

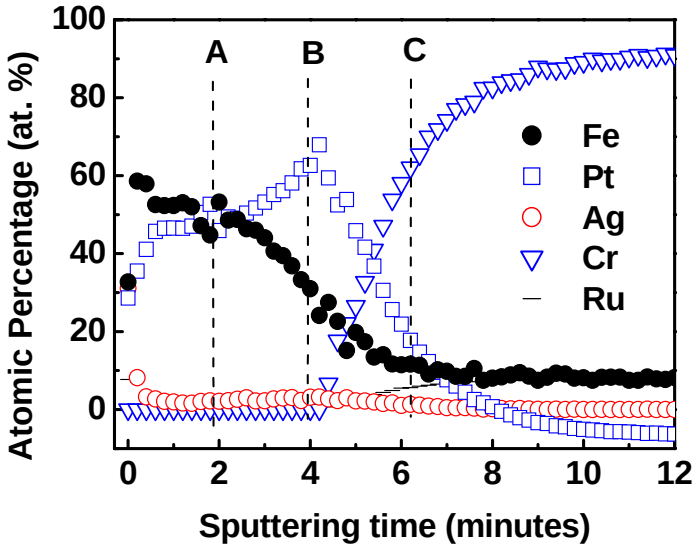

Figure 5-9 XPS depth profile of the FePt film with 2 nm Ag insertion

and melting temperatures of the elements are tabulated in Table 5-2.[120] Ag has the lowest surface energy and melting temperature that favor its surface segregation and diffusion, compared to other constituents in the film.

Table 5-2 Values of surface energy and melting temperatures of constituent elements

Element	Crystal Structure	Surface Energy at 0 K (mJ/m^2)	Melting Temperature T_m (K)	Surface Energy at T_m (mJ/m^2)
Fe	*bcc*	2550	1809	1830
Pt	*fcc*	2550	2042	1860
Ag	*fcc*	1250	1234	910
Cr	*bcc*	2400	2130	1700
Ru	*hcp*	3050	2523	2250

In the compositional depth profile where Ag would have been expected at the region if it were sandwiched by FePt (indicated by line A in Fig. 5-9), the Fe and Pt

concentrations showed anomalous variations. The Fe concentration decreased more than 8.0 at.% whereas Pt concentration increased by more than 8.0 at.%. This may be due to the redistribution of Fe and Pt as a consequence of Ag diffusion. When Ag diffused outwardly and throughout the film, Fe or Pt atoms substituted the voids left behind by Ag. The difference in diffusion activation energy of Fe and Pt could account for their compositional anomaly in that region. Although $Fe_{50}Pt_{50}$ target was used, Fe and Pt were not equiatomic in the sample. The Pt concentration was consistently higher than Fe throughout the whole film. This was due to the difference in elemental sputtering yield. In addition, the gradually increased Pt concentration with the depth suggested the Pt diffusion from the 4 nm Pt layer.

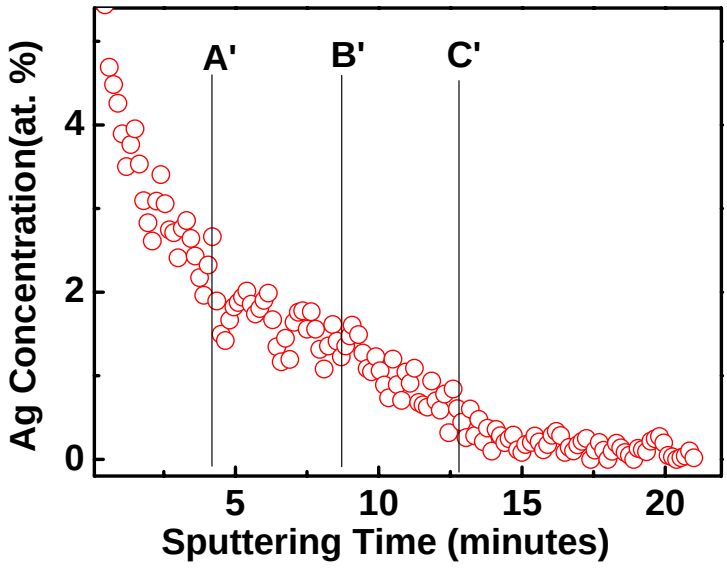

Figure 5-10 Ag concentration as a function of etching time for the FePt film with 2 nm Ag insertion

The diffusion of Cr and Ru from the underlayer to the magnetic layer was effectively blocked by the continuous Pt barrier layer (indicated by the region between lines B and C in Fig. 5-9). The low mobility and big atomic radius of Pt allowed the formation of a continuous layer that served as a diffusion barrier.

Figure 5-10 showed the high resolution of the compositional profile of Ag beneath the surface. The data points collected near the surface region, where the Ag concentration was high, were excluded in this figure for better scaling in data presentation of low Ag concentrations throughout the film. This data showed a decreasing Ag concentration from the film surface to the CrRu underlayer. The results confirmed that the Ag deposited between the two layers of FePt underwent diffusion. Note that the uncertainty of XPS was ~1 at.%. The Ag concentration in the film interior was smaller than 3 at.%.

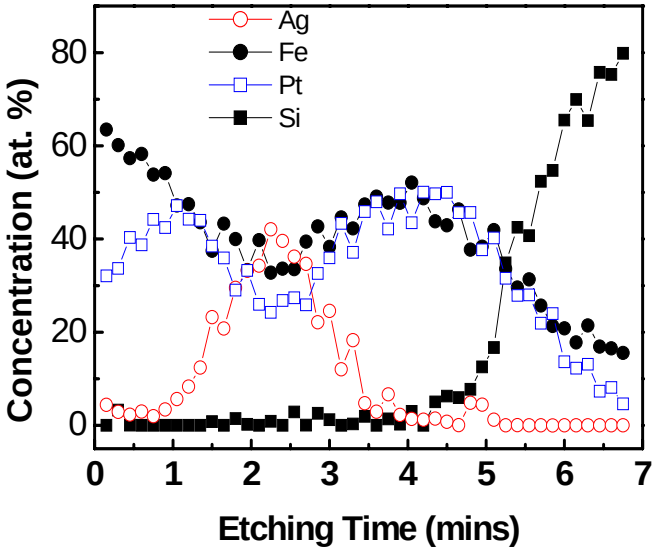

Figure 5-11 XPS depth profile of the FePt film with 2 nm Ag insertion deposited at room temperature on glass

As a comparison, XPS depth profile for the sample deposited at room temperature is shown in Fig. 5-11. Consistent with continuous Ag layer observed in the cross-section TEM image in Fig. 5-5, a range with high Ag concentration was evidenced in the middle of the magnetic layer.

It is known that the mass diffusion is governed by the first and second diffusion laws. And the diffusion coefficient follows the Arrhenius equation:

$$D = D_0 \exp(-\frac{E_a}{RT}) \quad \textbf{(5-1)}$$

Where E_a is the activation energy for the diffusion and T is the absolute temperature. The exponential relationship between D and T in Eq. 5-1 indicates the significant effect of temperature on diffusion coefficient. Thus, the diffusion in the sample deposited at room temperature would be less remarkable compared with the sample deposited at 350 °C.

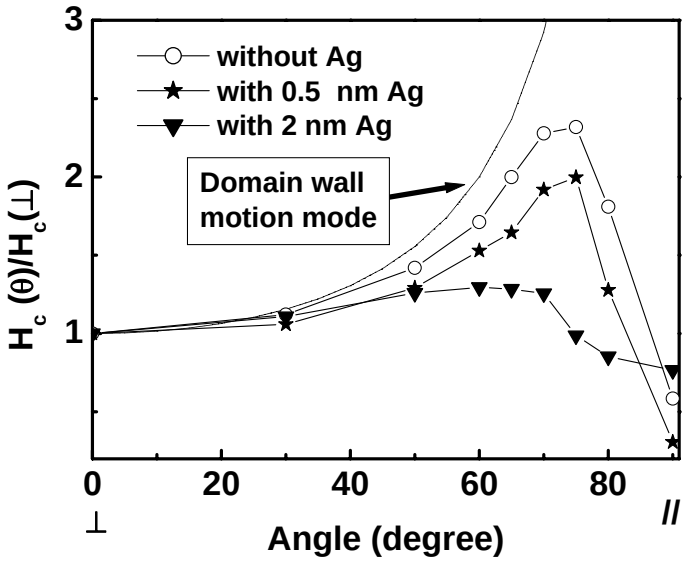

Figure 5-12 Coercivity angular dependence of the samples with varied thickness of Ag insertion (nominal)

Magnetization reversal mechanism in sequential deposited FePt/Ag/FePt structure was investigated in terms of coercivity angular dependence (Fig. 5-12). Without Ag insertion, the magnetic reversal mechanism was close to the domain wall motion mode. With increasing Ag thickness, the magnetic reversal mechanism approached the Stoner-Wohlfarth rotation mode, which is favorable for reducing the media noise. The result was similar with that in cosputtered FePt-Ag system.

The out-of-plane coercivity increased with FePt/Ag/FePt sequential deposition. However, coercivity is influenced by many factors such as ordering, grain size, magnetic

reversal mode. To investigate the relationship between $L1_0$ ordering and the coercivity, we examined the degree of $L1_0$ ordering by two different methods. One method involved the ratio of integrated intensities between FePt(001) and (002) peaks in the XRD spectra, commonly used as an indicator of the ordering. The ordering parameter S was calculated according to[121]

$$S^2=\frac{\left[I_{(001)}/I_{(002)}\right]_{exp}}{\left[I_{(001)}/I_{(002)}\right]_{theo}} \qquad \textbf{(5-2)}$$

The theoretical intensities of both the fundamental and superlattice diffractions can be estimated by considering the parameters of atomic fractions, atomic scattering factors, Debye-Waller corrections, Lorentz polarization factors, and structure factors.

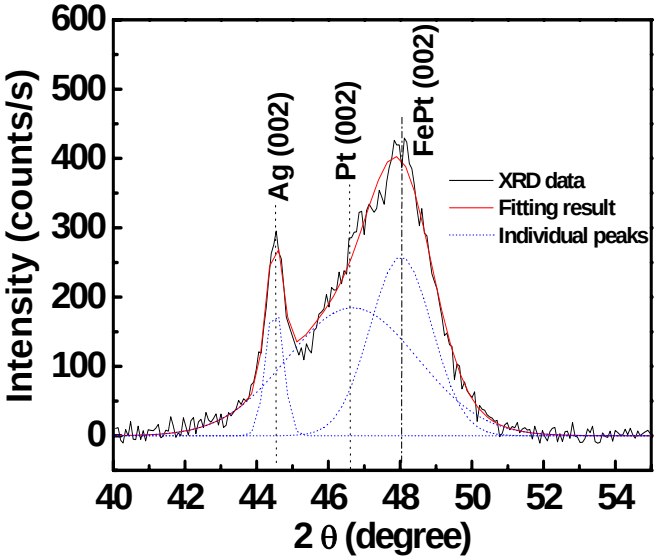

Figure 5-13 Multi-peak deconvolution fitting to the asymmetric FePt(002) peak

The asymmetric peak in the range of 45-50° in Fig. 5-2 resulted from the overlap of Pt(002), FePt(200) and FePt(002) peaks. To calculate the FePt(002) intensity, peak deconvolution was performed by fitting the spectra after the removal of background signal, assuming the Gaussian shape and 1.5° of the FWHM for each peak in the overlap. The fitting result (Fig. 5-13) showed that the intensity ratio of FePt(001)/(002) for the

sample with 2 nm Ag insertion was 23.7% lower than that of pure 10 nm FePt sample, indicating a reduced ordering due to Ag addition.

The other method was based on calculating the magnetocrystalline anisotropy constant K_u from Eq. 3-3. The calculated Ku values are listed in Table 5-3. It is observed that the use of Ag resulted in a reduction of anisotropy constant.

Table 5-3 Anisotropy field (H_k) estimated by extrapolating the hysteresis loops measured along magnetic easy axis and hard axis anisotropy energy (K_u) values calculated based on Eq. 3-3

Sample structure	H_k (KOe)	K_u (erg/cm^3)
No Ag	25.5	9.68×10^6
With 2 nm Ag	16.7	6.33×10^6

It has been reported in CoPt and FePt systems, the ordering process was enhanced by defects left behind in the film after the dopants diffused to the surface during annealing process.[40,85,111] The cosputtered FePt-Ag thin films also showed enhanced ordering with Ag. However, in FePt/Ag/FePt structure, the formation of FePt-Ag alloying may not be favored due to the subsequent deposition. Our results in this section confirmed that the pure FePt sample had a better chemical ordering than the sample with FePt/Ag/FePt structure. Ag subsequently diffused towards the surface after its deposition. The increased coercivity with the observed low degree of ordering could therefore not be dominated by chemical ordering.

To exclude the oxidation effect on the reduced $L1_0$ ordering, XPS spectra of pure $Fe_{50}Pt_{50}$ target and the FePt thin film sample with Ag insertion were compared (Fig. 5-14). No chemical shift compared with that of pure FePt (707 eV, 720 eV), even on the surface layer. Therefore, the reduced K_u was not associated with sample oxidation.

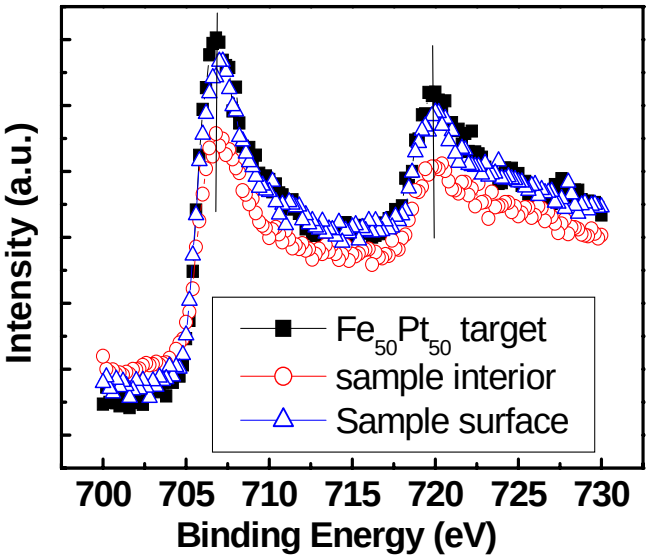

Figure 5-14 XPS spectra of pure $Fe_{50}Pt_{50}$ target and the FePt thin film sample with Ag insertion

The introduction of strong domain wall pinning sites is important for enhancing the coercivity of the FePt alloy, because the pinning effect of the nonmagnetic phase is more effective than that of the FePt polycrystalline grain boundaries.[122] The dominant pinning effect in coercivity mechanism was seen in our previous discussion on cosputtered FePt-Ag system. Therefore, even with lower K_u, the FePt-Ag system possessed high H_c due to the stronger pinning effect introduced by Ag.

5.4 Recording performance

The read/write test was performed on a Guzik spin-stand (1701B) using a 30 Gb/in^2 commercial ring head. The media noise and SNR of the FePt media with different thickness of Ag are shown in Fig. 5-15 and Fig. 5-16, respectively. With increasing Ag

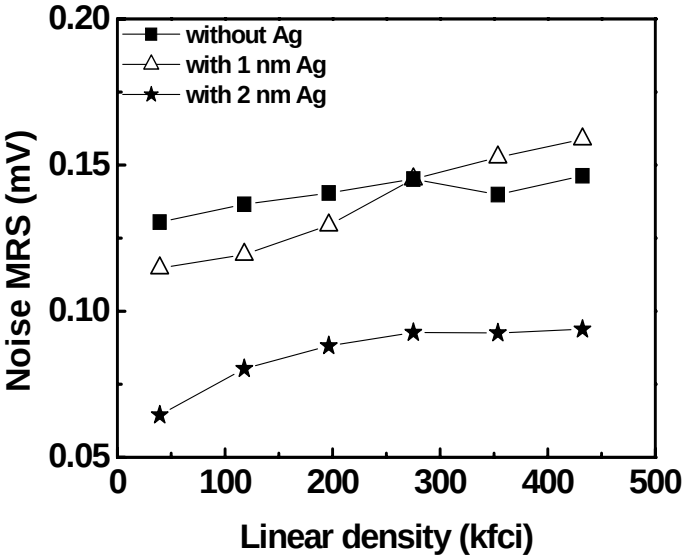

Figure 5-15 Recording noise as a function of linear density for FePt samples with different one-layer Ag thickness

thickness up to 2 nm, media noise is effectively reduced and the SNR is remarkably improved. The SNR of the FePt film with 2 nm Ag layer at 200 kfci is 10 dB higher than that without Ag layer.

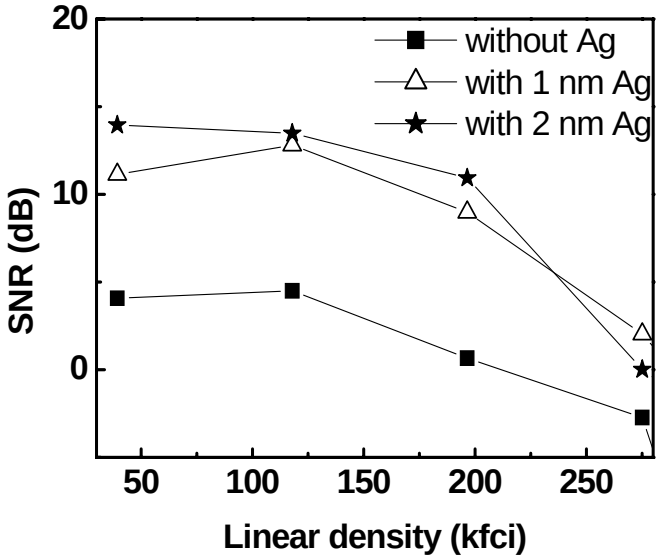

Figure 5-16 SNR as a function of linear density for FePt samples with different one-layer Ag thickness

Micromagnetic simulation showed that the densely distributed domain wall pinning sites ensure relatively smooth transition boundaries and much reduced transition noise.[123] The reduction in media noise and improvement in SNR are mainly due to the pinning of the domain wall by Ag itself and some structure defects of FePt layer caused by the inserting Ag layer between FePt.

5.5 Summary

The sequential deposition of FePt/Ag/FePt not only increased the coercivity, but also reduced the magnetic grain size. This was an effective way to improve the magnetic properties of perpendicular FePt thin films.

In FePt/Ag/FePt sequential deposition, 2 nm Ag deposition (nominal thickness) did not form a continuous layer but diffused into the FePt films with surface enrichment. Ag diffused throughout the FePt film with predominant segregation to the film surface. The surface segregation of Ag, confirmed by compositional profile analysis, could be due to the lower melting temperature and surface energy of Ag compared to other constituents. Though Ag did not promote the FePt $L1_0$ ordering process in the sandwiched structure, dispersed Ag and accompanying defects acted as pinning sites to increase the coercivity. Magnetic measurements showed that the exchange coupling was reduced by the sequential FePt/Ag/FePt deposition.

The sequential FePt/Ag/FePt deposition may significantly reduce the media noise and improve the SNR performance.

Chapter 6. Perpendicular FePt thin films with Ag underlayer

Lattice mismatch between substrate and film could either expand or shrink in the film direction, depending on the negative or positive mismatch. For a negative lattice mismatch, i.e. the lattice constant of film is less than that of substrate; the lattice constant could be expanded in the film direction and shrunk in the film normal direction. It has been suggested that the lattice mismatch at the interface between FePt film and underlayer may expand the *a* axis and shrink the *c* axis of the FePt film, favoring the ordering at low temperatures. Suzuki et al successfully fabricated $L1_0$ ordered FePt film at temperature of 400 °C using the high pressure sputtering.[124] It is suggested that the compressive stress along the *c*-axis resulted from high gas pressure (100 Pa) favored the formation of the $L1_0$ phase. The $L1_0$ FePt film was also prepared at 275 °C by the so-called dynamic stress, where FePt films were deposited on Cu underlayer/HF-cleaned Si (100) substrate, followed by post-deposition annealing.[125] Relationships between the lattice mismatch and the chemical ordering of the FePt films, and their magnetic anisotropic constant have been investigated with different intermediate layers.[126] The results showed that the *c* value decreased with increasing lattice mismatch from about 2.23% to 6.33%. Upon further increase of lattice mismatch, *c* increased in turn. The value of *c*/*a* held a minimum for lattice mismatch near 6.33%. These results suggested that there was a critical lattice mismatch, which was most favorable for improving the chemical ordering of FePt films.

Ag underlayer on Si substrate and CrX underlayer were used to fabricate the $L1_0$ FePt films at low temperature.[114, 127] The ordering of FePt films occurred even at the temperature as low as 200 °C based on the phase transformation induced by lattice mismatch.[128]

Previously, Pt buffer layer was used between the CrRu underlayer and the FePt layer. The lattice mismatch between Pt(002) and FePt(002) is only 2.23%. The relatively larger mismatch between Ag(002) and FePt(002) (7.1%) may be more favorable for FePt chemical ordering. In this chapter, the effects of Ag underlayer on the properties of perpendicular FePt thin films were studied.

6.1 Development of Ag(002) texture

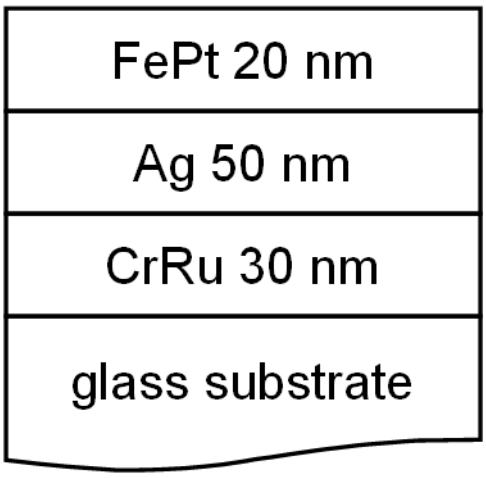

Figure 6-1 Sample structure for FePt thin films with Ag underlayer

In the structure of Glass/CrRu/Ag/FePt (Fig. 6-1), Ag(002) texture was necessary to ensure the perpendicular texture of FePt layer. To optimize the deposition conditions, the crystalline texture of Ag layer as a function of the experimental parameters such as,

working gas pressure, sputter power and substrate temperature was investigated. The magnetic properties of the multilayer films were investigated accordingly.

Table 6-1 Deposition conditions for optimization of Ag(002) texture

Layer	CrRu	Ag	FePt
Thickness (nm)	30	50	20
Temperature (°C)	350	200,250,300	320
Argon pressure (mTorr)	2	3,10	10

Experiment conditions are summarized in Table 6-1. The deposition temperature for CrRu and FePt layer were fixed at 350 °C and 320 °C, respectively. Their thickness was fixed at 30 nm and 20 nm, respectively. Based on the result in Chapter 5, Ag continuous layer required a relatively larger thickness due to its small surface energy. The thickness of Ag layer was fixed at 50 nm while the temperature and gas pressure was varied respectively.

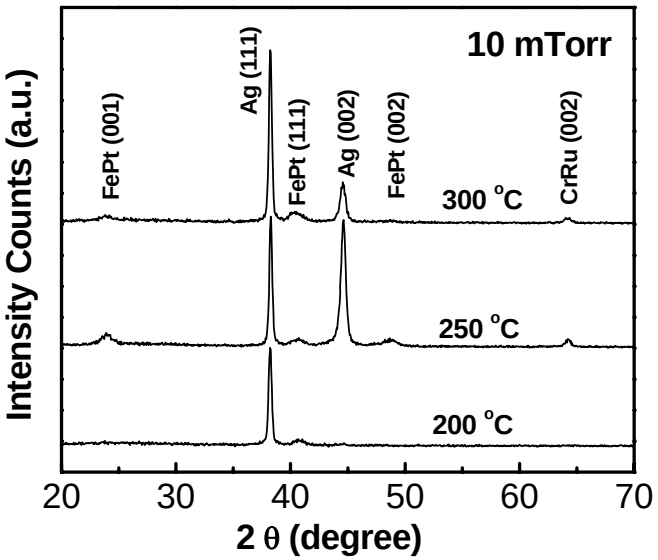

Figure 6-2 XRD spectra of samples deposited with 10 mTorr argon pressure but different temperature

The XRD spectra of the samples with 10 mTorr gas pressure are compared for different deposition temperatures (Fig. 6-2). At 200 °C, only Ag(111) and FePt(111)

peaks existed, indicating the absence of perpendicular texture of Ag layer and FePt layer. When the temperature increased to 250 °C and above, CrRu(002) peaks appeared. The Ag(002), FePt(001) and FePt(002) peaks also developed. However, Ag(111) texture kept dominant for all the three deposition temperatures, although Ag(002) can be promoted with higher temperature.

With 3 mTorr gas pressure, the XRD spectra of the samples for different deposition temperatures are compared again in Fig. 6-3. With increasing temperature, Ag(200) became dominant texture under relatively low temperature of 250 °C. As a consequence, FePt(001) and FePt(002) peaks with higher diffraction intensity can be observed and became dominant texture in the media.

The XRD results suggested that Ag texture closely rely on the deposition temperature and gas pressure.

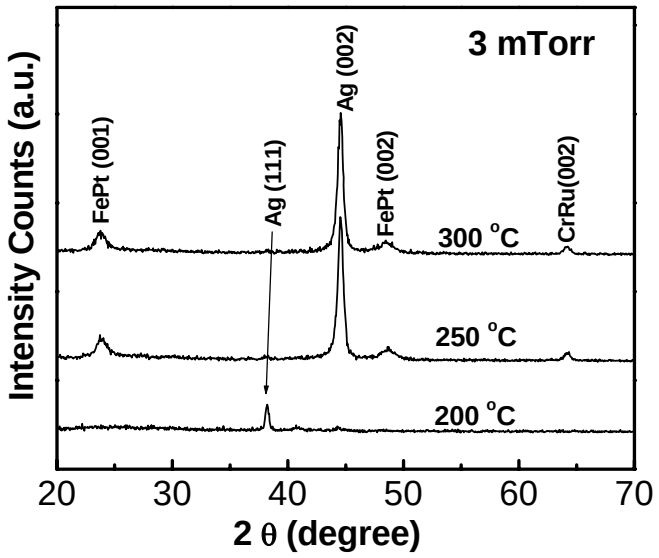

Figure 6-3 XRD spectra of samples deposited with 3 mTorr argon pressure but different temperature

Figure 6-4 showed the magnetic properties of the glass/CrRu/Ag/FePt multilayer films with Ag layer deposited at different conditions. For the samples with Ag deposited at 10

mTorr, the coercivities were comparable to each other. M-H loops were unsaturated under the maximum magnetic applied field, because the magnetic easy axis was not perpendicularly aligned according the XRD data.

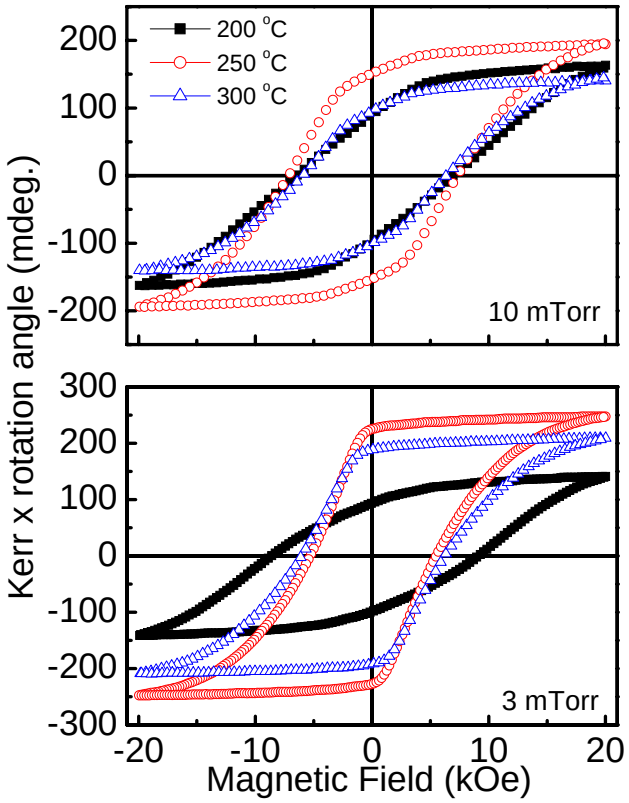

Figure 6-4 M-H loops of glass/CrRu/Ag/FePt where Ag layer was prepared with 10 mTorr and 3 mTorr gas pressure

Small kink were observed for the samples prepared with 10 mTorr, indicating the co-existence of soft FePt *fcc* phase. This was consistent with the weak *fcc* FePt(111) diffraction peaks in XRD spectra. The existence of the soft phase FePt gave rise to a positive nucleation field for the samples, which was unfavorable for the recording media application. The diffraction peak of soft phase FePt(111) was also observed for 3 mTorr sample deposited on substrate heated at 200°C. However, it was mainly due to the poorly formed CrRu (200) as shown in the XRD spectra. The relatively large coercivity for the

sample with 10 mTorr was probably due to the pinning at the boundaries of the FePt fct/fcc phases.

6.2 Effects of deposition temperature and thickness for Ag layer

Based on the results in section 6.1, 3 mTorr gas pressure gave a better texture and magnetic performance. To further study the film properties, the effects of Ag thickness under 200 °C were studied.

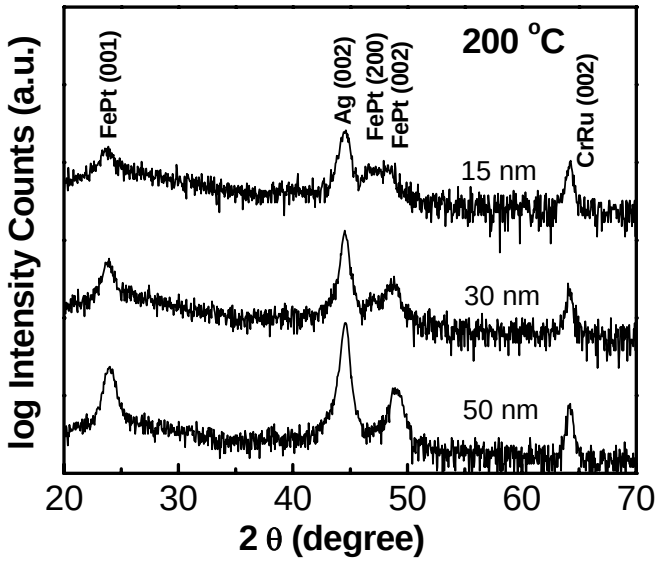

Figure 6-5 XRD spectra of glass/CrRu/Ag/FePt thin films deposited at 200 °C with different Ag thickness

The log-scale XRD spectra for the samples with different Ag thickness were shown in Fig. 6-5. FePt(001) intensity was enhanced with increasing Ag thickness,

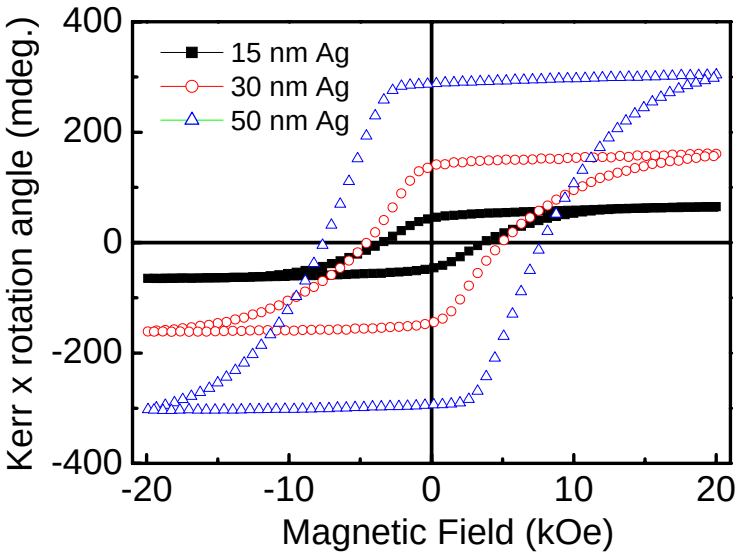

Figure 6-6 Out-of-plane M-H loops of glass/CrRu/Ag/FePt thin films deposited at 200 °C with different Ag thickness

indicating the improved ordering and perpendicular texture. Corresponding M-H loops were shown in Fig. 6-6. The observed increase of H_c and M_s with increasing Ag thickness was consistent with the better texture. The low M_s with lower Ag thickness could be due to Cr diffusion into FePt, because a continuous layer was not formed.

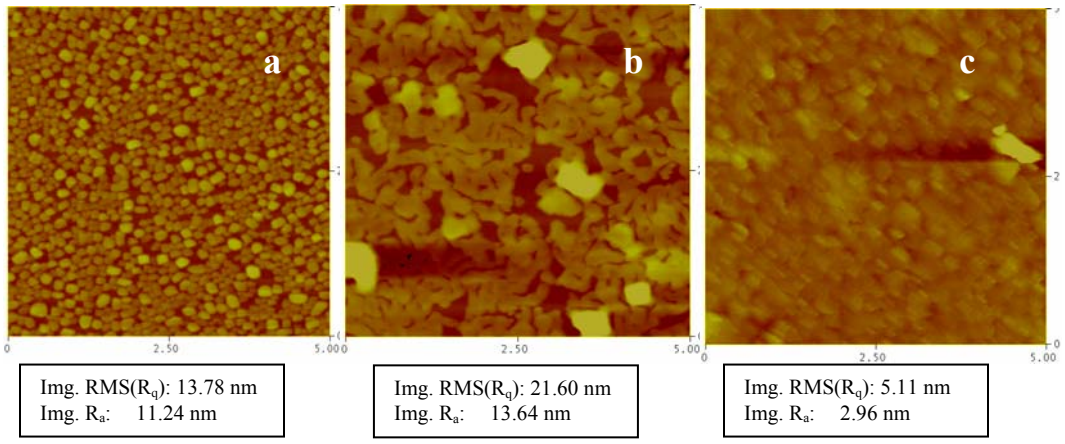

Figure 6-7 AFM images of CrRu/Ag/FePt thin film prepared at 200°C with a)15 nm; b) 30nm; c) 50 nm Ag layer

The nucleation field changed from positive to negative with increasing Ag thickness. The slope at H_c increased with increasing Ag thickness, indicating higher

magnetic coupling. The increased coupling with Ag increasing Ag thickness may be due to the closer intergranular distance observed in the AFM images (Fig. 6-7). Although the surface roughness R_q of about 5.1 nm was obtained for the samples with 50 nm Ag layer, the peak-valley distance is about 40 nm. A reason could be that the lager grain size of Ag layer was deposited at such high temperature.

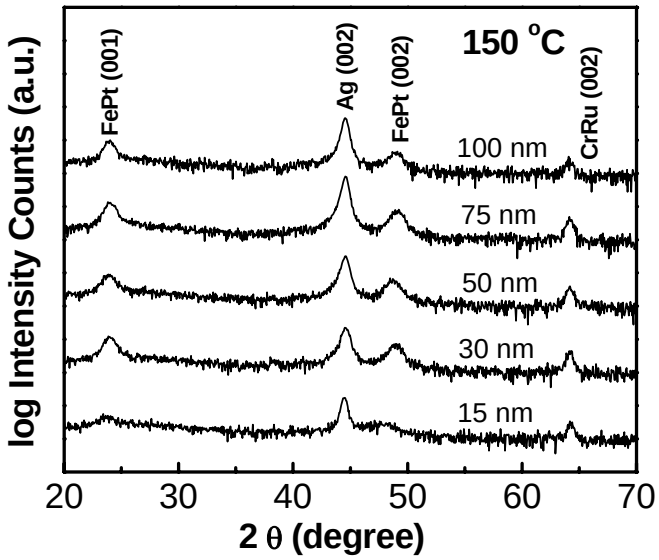

Figure 6-8 XRD spectra of glass/CrRu/Ag 50nm/FePt samples with different Ag thickness deposited at 150 °C

In order to improve the surface morphology of the multilayer film for application purpose, the deposition temperature for Ag layer was reduced to 150°C.

Figure 6-8 shows the XRD spectra of CrRu/Ag/FePt with different thickness of Ag layer prepared at 150°C. The Ag(200) texture was formed for Ag layer with different thickness and the growth of $L1_0$ ordered FePt films was obtained. The magnetic properties showed weak dependence on Ag layer thickness when it exceeded 30 nm.

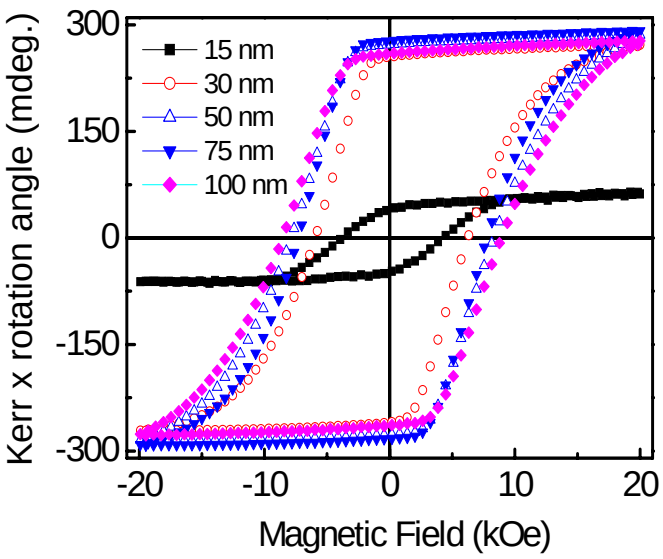

Figure 6-9 Out-of-plane M-H loops of glass/CrRu/Ag 50nm/FePt thin films deposited at 150 °C with different Ag thickness

Figure 6-9 shows the M-H loops for the samples deposited at 150 °C. The sample with 15 nm Ag layer demonstrated loops with a relatively small slope at H_c, suggesting a low magnetic coupling compared to these samples with thicker Ag layers. Once the Ag layer thickness exceeded 30 nm, the M-H loops showed similar slopes at the coercive field. Similarly with 200 °C, the sample with 15 nm Ag layer showed a much lower Ms than the others with a thicker Ag.

The AFM images for multilayer film samples with different Ag layer thickness were given in Fig. 6-10. The sample with 15 nm Ag layer demonstrated an isolated island morphology, which suggested that the Ag did not form continuous layer at the given temperature due to the low surface energy of Ag.

Compare to the films with Ag layer prepared at 200 °C, the reduction of the Ag deposition temperature improved the surface morphology of the multilayer film, a smoother surface with R_q of about 3.6 nm and the peak-valley distance of about 20 nm were obtained.

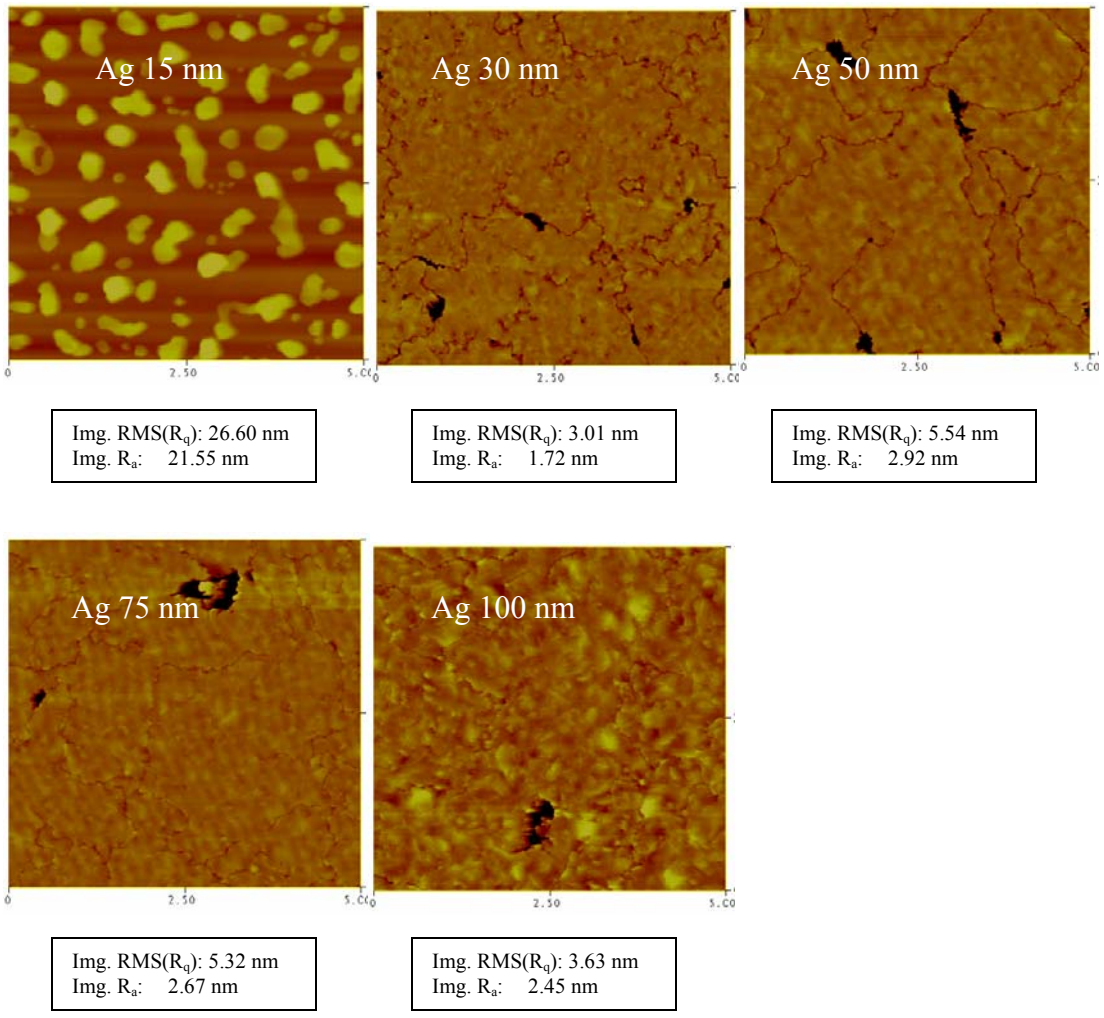

Figure 6-10 AFM images of CrRu/Ag/FePt thin films deposited at 150°C with different Ag thickness

6.3 Effects of deposition power for Ag layer

In order to further improve the surface morphology of the film, especially the peak-valley distance for application, the multilayer films with 50 nm Ag layer prepared at 150°C under different sputter powers were prepared.

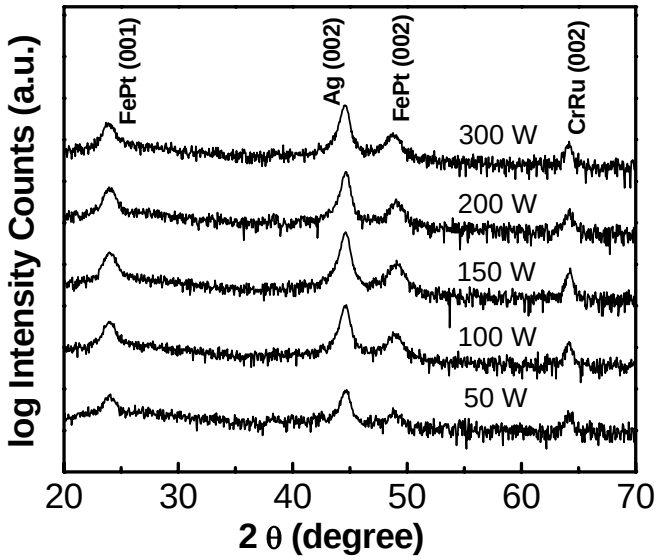

Figure 6-11 XRD spectra of glass/CrRu/Ag/FePt samples with different power

XRD spectra for the samples with different deposition power were shown in Fig. 6-11. The Ag(002) texture was developed for Ag layer under different sputter powers and the growth of $L1_0$ ordered FePt films were obtained. The film texture did not change significantly with the variation of Ag power.

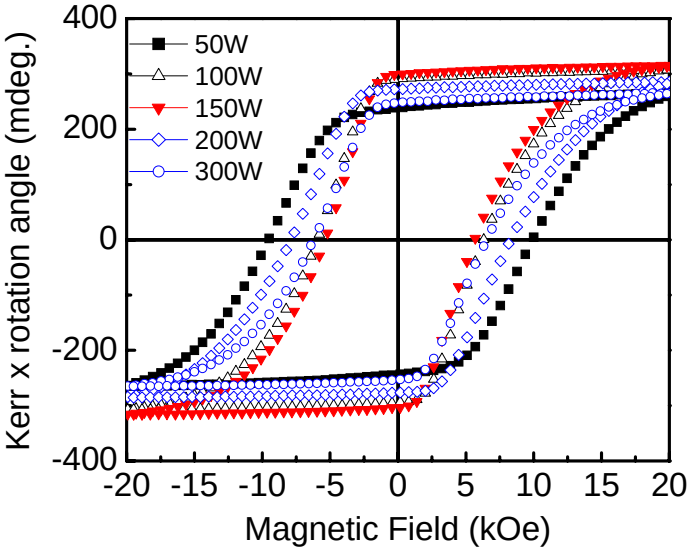

Figure 6-12 M-H loops of CrRu/Ag 50 nm/FePt, where Ag layer was deposited at different sputter powers

M-H loops of the samples with different Ag power were shown in Fig. 6-12. The magnetic properties showed a negative nucleation field for all the samples, which is favorable to the recording media application. The shape and slope of the loops did not change significantly with the variation of Ag power.

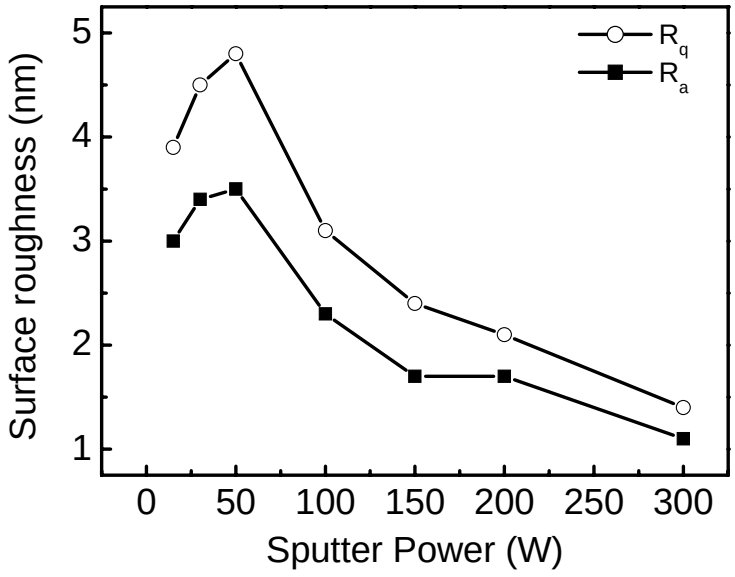

Figure 6-13 The effect of Ag sputter power on surface roughness

The surface roughness and data were shown in Fig. 6-13. It can be seen that the surface roughness decreased with the increasing sputter power for Ag deposition. The surface roughness R_q of about 1.4 nm was obtained for Ag layer deposited under 300W sputter power.

The decrease in the peak-valley distance with increasing Ag power was also observed as shown in Fig. 6-14. The peak-valley distance of about 13 nm were obtained for Ag layer deposited under 300W sputter power.

In terms of surface and a smaller peak-valley distance, higher sputter power for Ag sink layer deposition is favorable to obtain a smoother film. The reason may be due to

the higher kinetic energy provided with the higher deposition power, which enhanced atomic mobility and improved the film roughness.

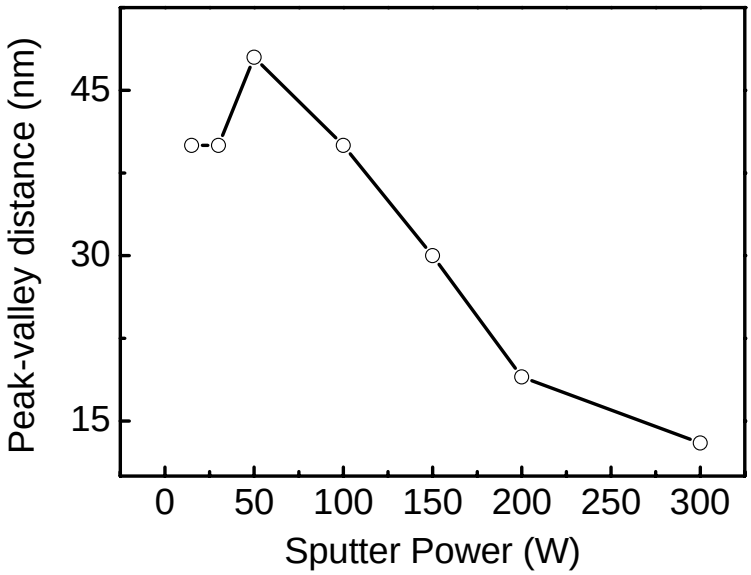

Figure 6-14 The effect of Ag sputter powers on peak-valley distance

6.4 Summary

In this chapter, the effects of Ag underlayer were investigated in terms of films texture, morphology and magnetic properties.

The texture of the Ag underlayer closely relied on experimental conditions. A lower working gas pressure was favorable to form the Ag(200) texture at a relatively low substrate temperature.

The Ag layer showed island growth in films with smaller thickness (below 15 nm) and became continuous as the layer thickness increased. When the Ag underlayer thickness exceeded 30 nm in our study, it did not have much influence on the magnetic properties of the FePt layer grown on the top.

Although multilayer films showed a small value of R_q and R_a, the peak-valley distance of the films was over 30 nm in most of cases. It was found that higher sputter power for Ag underlayer deposition was favorable to obtain a smoother film surface and a smaller peak-valley distance.

Writing on magnetically harder media requires a higher writing field. Heat assisted magnetic recording (HAMR) has been proposed to overcome the writing problem, which requires localized heating for recording and ease the writing. In the design of HAMR, the heat generated must be dissipated after the writing process to prevent the erasure of the stored information in the magnetic layer. A heat sink layer with sufficient thermal diffusivity and sufficient thickness is a solution for dissipating heat generated by the rise in localized temperature. Ag is a good candidate because of its high thermal conductivity (429 W/m•K). The favorable result in this chapter is encouraging for the application of Ag as heat sink layer in FePt HAMR system.

Chapter 7. Summary and Conclusions

This thesis studied how to improve the magnetic and structural properties of high anisotropy $L1_0$ FePt magnetic thin films. The optimizing of magnetic properties, the reduction of FePt grain size, exchange coupling and control over crystallographic texture are major concerns in application.

The Ag concentration showed significant effects on the texture of FePt thin films when cosputtered with FePt on both CrRu underlayer and glass substrates. With increasing Ag concentration up to 30 vol.%, longitudinal texture became favorable. The variation of the film texture was associated with the competition between grain boundary energy, surface energy and interface strain energy during the thin film growth. The FePt thin films with Ag concentration over 40 vol.% showed significant Ag surface segregation and led to high surface roughness that was unfavorable for application.

Conventional XRD and TEM have deficiencies to characterize the phase and miscibility in nanostructured materials composed of elements with close atomic numbers, lattice parameters. With the advantages of AXS and EXAFS techniques, semi-quantitative analysis on the FePt-Ag alloying and the atomic local environment of specific element in the textured FePt thin films was realized. It was found that only less than 7% Ag alloyed with FePt for the samples with a global concentration of 20-30 vol.% Ag. The alloyed Ag tended to replace Fe in the FePt thin film. The majority of Ag remained segregated phases. FePt-Ag alloying may account for the enhanced $L1_0$ ordering due to the resultant lower melting point. In addition, the diffusion process of the

Ag surface segregation was favorable for $L1_0$ ordering because of more vacancies generated.

The enhanced coercivity in the cosputtered FePt-Ag thin films was mainly due to the pinning effect of the dispersed Ag, which would pin the domain wall motion and make the magnetic reversal mechanism close to the Stoner-Wolfarth rotation mode. The nonmagnetic Ag neighboring FePt also reduced the magnetic exchange coupling.

Although a continuous Ag layer was not formed for the sequential FePt/Ag/FePt deposition at 350 °C with a nominal Ag thickness of 2 nm, the perpendicular FePt texture was maintained with improved H_c and recording SNR. The anisotropy calculation for the perpendicular FePt samples with Ag insertion did not show improved $L1_0$ ordering that was reported in cosputtered FePt-Ag system. The coercivity enhancement and decoupling effects with the FePt/Ag/FePt sequential deposition suggested a potential way to tune the magnetic properties of perpendicular recording media by means of introducing pinning sites.

When deposited at 350 °C, Ag diffused throughout the FePt thin films and preferred to segregate to film surface regardless of cosputtering or sequential sputtering with FePt layers. Both methods showed restraining effect on FePt grain size and enhanced coercivity. The surface segregation of Ag was attributed to the low surface energy and melting temperature of Ag. The Ag diffusion in the sample deposited at room temperature was less significant, indicating the important role of thermal energy in the diffusion process.

Ag could be used as underlayer between CrRu and FePt layers to promote the FePt ordering. Film structure and magnetic properties closely depended on deposition

conditions and the thickness of Ag layer. The Ag layer showed an island growth mode when the thickness was less than 15 nm and became continuous as the layer thickness increased. Ag may be a promising candidate for heat sink layer in FePt HAMR system because of its close lattice mismatch with FePt and good thermal conductivity.

Publications

1. **Y.Z. Zhou**, J.S. Chen, G.M. Chow, J.P. Wang, "Structural and magnetic properties of perpendicular FePt thin films with inserted Ag layer", Journal of Applied Physics, 95:7495 (2004).
2. **Y.Z. Zhou**, J. S. Chen, G. M. Chow, J. P. Wang "FePt-Ag nanocomposite thin films with longitudinal magnetic anisotropy", Journal of Nanoscience and Nanotechnology, 4:704 (2004).
3. **Y.Z. Zhou**, J.S. Chen, G.M. Chow and J.P. Wang, "Structure and magnetic properties of in-plane oriented FePt-Ag nanocomposites", Journal of Applied Physics, 93: 7577 (2003).
4. J.S. Chen, **Y.Z. Zhou**, B.C. Lim, J. Zhang, G.M. Chow, "Improvement of Recording Performance in FePt Perpendicular Media by Ag Pinning Layer", IEEE Transaction on Magnetics, 41: 3196 (2005).

References

1 R. L. White, J. Magn. Magn. Mater., **209**, 1(2000)
2 R. Wood, IEEE Trans. Magn., **36**, 36(2000)
3 D. E. Speliotis, J. Mag. Soc. Japan 21 Suppl., **S2**, 152(1997)
4 S. Iwasaki, Y. Nakamura, IEEE Trans. Magn., **24**, 2850(1988)
5 Hehn M, Ferre R, Ounadjela K, Bucher J. P and Pousseau F, J. Magn. Magn. Mater., **165**, 5(1997)
6 Chou, S, Proc. of the IEEE , **85**, 652(1997)
7 Http://www.westerndigital.com
8 R.Wood, Y. Sonobe, Z.Jin, B.Wilson, J.Mag.Mag.Mater., **235**, 1(2001)
9 R. Street, J. C. Woolley, Proc. Phys. Soc. A, **62**, 562(1949)
10 E. Isaac, G. Tammann, and Z. Anorg, Chem., **55**, 63(1907)
11 U. Dehlinger and L. Graf, Physik., **64**, 359(1930)
12 A. kussma and G.V. Tittberg, Metallkunde, **42**, 470(1950)
13. L. Graf and A. Kussman. Physik., **36**, 544(1935)
14 H. Lipson, D. Schoenburg, and G.V. Rittberg, J. inst. Metal., **67**, 333(1941)
15. A. kussma, M. Auwarter, and G.V. Rittberg, Ann. Physik., **4**, 147(1948)
16 V.A. Nemilov and Izevest, Inst. Platiny., **7**, 1(1912)
17 M.Hansen, 2nd ed., McGraw-Hill, (1958)
18 C. Kittel, *Introduction to solid physics*, 7th ed., John Wiley& Sons, New York, (1996)
19 O. A. Ivanov, L. V. Solina, and V. A. Demshina, Phys. Met. Metallogr., **35**, 81(1973)
20 O.A. Ivanov, L.V. Solina, V.A. Demshina, and L.M. Magat, Fiz.metal. Metalloved., **35**, 92(1973)
21 M. Fallot, Compt. Rend. **199**, 128(1934)
22 V.G .Pynko, A.S. Komalov, and L.V. Ivaeva, Phys. Stat. Sol., **63a**, 127(1981)
23 M. Watanabe, T. Nakayama, K.Watanabe, T. Hirayama, and A. Tonomura, Mater. Trans. JIM., **37**, 489(1996)
24 D. Weller, A. Moser, L. Folks, M. E. Best, W. Lee, M. F. Toney, M. Schwickert, J. Thiele, and M. F. Doeerner, IEEE Trans. Magn., **36**, 10(2000)
25 M. Watanabe, T. Nakayama, K. Watanabe, T. Hirayama, and A. Tonomura, Mater. Trans., JIM **37**, 489(1996)
26 T. Massalsky (Eds.), *Binary Alloy Phase Diagrams*, 2nd Edition, ASM International, 1996
27 Y.K. Takahashi, M. Ohnuma, K. Hono, J. Magn. Magn. Mater., **246**, 259(2002)
28 T. Maeda, T. Kai, A. Kikitsu, T. Nagase, and J. Akiyama, Appl. Phys. Lett., **80**, 2147(2002)
29 C.P. Luo, S.H. Liou, D.J. Sellmyer, J. Appl. Phys., **87**, 6941(2000)
30 P.C. Kuo, Y.D. Yao, C.M. Kuo and H.C. Wu, J. Appl. Phys., **87**, 6146(2000)
31 C.M. Kuo, P.C. Kuo, J. Appl. Phys., **87**, 419(2000)
32 M. Daniil, P.A. Farber, H. Okumura, G.C. Hadjipanayis, D. Weller, J. Magn. Magn. Mater., **246**, 297(2002)
33 S.C. Chen, P.C. Kuo, C.T. Lie, J.T. Hua, J. Magn. Magn. Mater., **236**, 151(2001)
34 C.P. Luo, S.H. Liou, L. Gao, Y. Liu, and D.J. Sellmyer, Appl. Phys. Lett., **77**, 2225(2000)
35 J.A. Christodoulides, Y. Huang, Y. Zhang, G. C. Hadjipanayis, I. Panagiotopoulos, D. Niarchos, J. Appl. Phys., **87**, 6938(2000)
36 C. Kuo, P.C. Kuo, W. Hsu, C. Li, A. Sun, J. Magn. Magn. Mater., **209**, 100(2000)
37 S. R. Lee, S. Yang, Y. K. Kim, and J. G. Na, Appl. Phys. Lett., **78**, 4001(2001)
38 S.C. Chen, P.C. Kuo, A.C. Sun, C.T. Lie, W.C. Hsu, Mater. Sci. Eng. B, **88**, 91(2002)
39 T. Yang, E. Ahmad, and Suzuki, J. Appl. Phys., **91**, 6860(2002)
40 C.L. Platt, K.W. Wierman, E.B. Svedberg, R. Van de Veerdonk, J.K. Howard, A.G. Roy and D.E. Laughlin, J. Appl. Phys., **92**, 6104(2002)
41 K.R. Coffey, M.A. Parker, J.K. Howard, IEEE Trans. Magn. Mag., **31**, 2737(1995)
42 Yu-Nu Hsu et al, IEEE Trans. Magn., **36**, No. 5, 68(2000)
43 Yingfan Xu, J. S. Chen, and J. P. Wang, Appl. Phys. Lett., **80**, 3325 (2002)

44 M. Ohring, The Materials Science of Thin films, Academic Press, Inc. (1992)
45 L. Eckertova, Physics of Thin Films, New York: Plenum Press (1986)
46 W.D. Westwood, MRS Bulletin, Vol. XIII No. 12, 46(1988)
47 B. Chapman, Glow Discharge Processes, John Wiley & Sons, (1980)
48 B. D. Cullity, *Elements of X-ray Diffraction (2nd edition)*, Addison-Wesley, (1978)
49 Fricke, H., Phys. Rev., **16**, 202(1920)
50 Hertz, G., Z. Phys., **3**, 19(1920)
51 Coster, D., Z. Phys., **25**, 83(1924)
52 Lindh, A.E., Z. Phys., **6**, 303(1921); **31**, 210(1925)
53 Ray, B.B., Z. Phys., **55**, 119(1929)
54 Kievit, B. and Lindsay, G.A., Phys. Rev., **36**, 648(1930)
55 Hanawalt, J.D., Z. Phys., **70**, 20(1931); Phys. Rev., **37**, 715(1931)
56 de L. Kronig, R., Z. Phys., **70**, 317(1931)
57 de L. Kronig, R., Z. Phys., **75**, 468(1932)
58 Peterson, H., Z. Phys., **76**, 768(1932); **80**, 528(1933); **98**, 569(1936)
59 Kostarev, A.I., Zh. Eksp. Teor. Fiz., **11**, 60(1941); **19**, 413(1949)
60 Sawada, M., Rep. Sci. Works Osaka Univ., **7**, 1(1959)
61 Shmidt, V.V., Izv. Akad. Nauk SSSR, Ser. Fiz., **25**, 977(1961); **27**, 392(1963)
62 Kozlenkov, A.I., Izv. Akad. Nauk SSSR, Ser. Fiz., **25**, 957(1961); **27**, 364(1963); **38**, 500(1974)
63 Sayers, D.E., Stern, E.A., and Lytle, W.F., Phys. Rev. Lett., **27**, 1024(1971)
64 Thole, T., Carra, P., Sette, F., and Van der Laan, G., Phys. Rev. Lett., **68**, 1943(1992)
65 Chen, C.T., Sette, F., Ma, Y., and Modesty, S., Phys. Rev. B, **42**, 7262(1990)
66 Darty, E., Depautex, C., et al., Nucl. Instrum. Methods, Phys. Res. A, **246**, 452(1986)
67 P.A. Lee, P.H. Citrin, P. Eisenberger, and B.M. Kinkaid, Rev. Mod. Phys., **53**, 769(1981)
68 G. M. Chow, W. C. Goh, Y. K. Hwu, T. S. Cho, J. H. Je, H. H. Lee, H. C. Kang, D. Y. Noh, C. K. Lin and W. D. Chang, Appl. Phys. Lett., **75**, 2503(1999)
69 C. Mallinson, *The Foundations of Magnetic Recording*, Academic Press, Inc. (1987)
70 S. Chikazumi, *Physics of Ferromagnetism*, Oxford University Press, (1997)
71 Y. Huang, H. Okumura, G. C. Hadjipanayis, and D. Weller, J. Magn. Magn. Mater., **242**, 317(2002)
72 M. Watanabe, T. Masumoto, D. H. Ping, and K. Hono, Appl.Phys.Lett., **76**, 3971(2000)
73 D. H. Ping, M. Ohnuma, K. Hono, M. Watanabe, T. Iwase, and T. Masumoto, J. Appl. Phys., **90**, 4708(2001)
74 Y.-C. Wu, L.-W. Wang and C.-H. Lai, Appl. Phys. Lett., **91**, 072502(2007)
75 S. R. Lee, S. H. Yang, Y. K. Kim, and J. G. Na, J. Appl. Phys., **91**, 6857(2002)
76 C. L. Platt, K. W. Wierman, J. K. Howard, A. G. Roy, and D.E. Laughlin, J. Magn. Magn. Mater., **260**, 487 (2003)
77 N. Li, B. M.Lairson, and O. H. Kwon, J. Magn. Magn. Mater., **205**, 1(1999)
78 N. Li and B.M.Lairson, IEEE Trans. Magn., **35**, 1077(1999)
79 T.Kai, T.Maeda, A.Kikitsu, J.Akiyama, T.Nagase, T.Kishi, J. Appl. Phys., **95**, 609(2004)
80 T. Maeda, A. Kikitsu, T. Kai, T. Nagase, H. Aikawa, and J. Akiyama, IEEE Trans. Magn., **38**, 2796(2002)
81 K.W.Wierman, C.L.Platt, J.K.Howard, J.Magn.Magn.Mater., **278**, 214(2004)
82 X.C.Sun, S.S.Kang, J.W.Harrell, D.E.Nikeles, Z.R.Dai, J.Li, Z.L.Wang, J. Appl. Phys., **93**, 7337(2003)
83 K.W.Wierman, C.L.Platt, J.K.Howard, F.E.Spada, J.Appl.Phys., **93**, 7160(2003)
84 K.Barmak, D.C.Berrya, B.J.Kima, K.W.Wierman, E.B.Svedberg, J.K.Howard, Engineering Conference International, Copper Mountain, CO, August 15-20, (2004)
85 S.S. Kang, D.E. Nikles and J.W. Harrell, J. Appl. Phys., **93**, 7178(2003)
86 O. Kitakami, Y. Shimada, K. Oikawa, H. Daimon and K. Fukamichi, Appl. Phys. Lett., **78**, 1104(2001)
87 K.Barmak, J. Kim, L.H. Lewis, K.R. Coffey, M.F. Toney, A.J. Kellock, J.U. Thiele, J. Appl. Phys., **95**, 7501(2004)
88 J. S. Chen, B. C. Lim, and J. P. Wang, Appl. Phys. Lett., **81**, 1848(2002)
89 C.V. Thompson, Interf. Sci., **6**, 85(1998)
90 C.V. Thompson, Annu. Rev. Mater. Sci., **20**, 245(1990)
91 R. F. C. Farrow, D. Weller, R. F. Marks, M. F. Toney, A. Cebollada, and G. R. Harp, J. Appl. Phys., **79**, 5967(1996)

92 R. F. C. Farrow, D. Weller, R. F. Marks, M. F. Toney, D. J. Smith, and M. R. McCartney, J. Appl. Phys., **84**, 934(1998)
93 H.R. Hilzinger, Appl. Phys. A, **12**, 253(1997)
94 H. Kronmüller, K.D. Durst and M. Sagawa, J. Magn. Mag. Mat., **74**, 291(1988)
95 H. Kronmüller, Phys. Stat. Sol. (b), **144**, 385(1987)
96 T. Suzuki, H. Notarys, D. C. Dobbertin, C.J. Lin, D. Weller, D.C. miller and G. Gorman, IEEE trans. Magn., **28**, 2754(1992)
97 C. Michaelsen, Phil. Maga. A, **72**, 813(1995)
98 H. Stragier, J. O. Cross, J. J. Rehr, L. B. Sorensen, C. E. Bouldin, and J. C. Woicik, Phys. Rev. Lett., **69**, 3064(1992)
99 H. Renevier, J. L. Hodeau, P. Wolfers, S. Andrieu, J. Weigelt, and R. Frahm, Phys. Rev. Lett., **78**, 2775(1997)
100 T. Bigault, F. Bocquet, S. Labat, O. Thomas, and H. Renevier, Phys. Rev. B, **64**, 125414(2001)
101 S.-W. Han, E. A. Stern, D. Haskel, and A. D. Moodenbaugh, Phys. Rev. B, **66**, 94101(2002)
102 E. A. Stern, Phys. Rev. B, **10**, 3027(1974)
103 J. J. Rehr and R. C. Albers, ibid. **41**, 8139(1999)
104 E. A. Stern, M. Newville, B. Ravel, Y. Yacoby, and D. Haskel, Physica B, **208&209**, 117(1995)
105 A. L. Ankudinov, B. Ravel, J. J. Rehr, and S. D. Conradson, Phys. Rev. B, **58**, 7565(1998)
106 A. L. Ankudinov and J. J. Rehr, ibid. **56**, R1712(1997)
107 S. I. Zabinsky, J. J. Rehr, A. Ankudin, R. C. Albers, and M. J. Eller, ibid., **52**, 2995(1995)
108 B.L. Henke, E.M. Gullikson, and J.C. Davis., Atomic Data and Nuclear Data Tables, **54**, 181(1993)
109 Y. Maeda and M. Asahi, J. Appl. Phys., **61**, 1972(1987)
110 D. R. Lide *CRC Handbook of Chemistry and Physics, 88th Edtion*, CRC press, (2007)
111 C. Chen, O. Kitakami, S. Okamoto, and Y. Shimada, Appl. Phys. Lett., **76**, 3218(2000)
112 K. Barmak, J. Kim, D.C. Berry, W.N. Hanani, K. Wieman, E.B. Svedberg, K.J. Howard, J. Appl. Phys., **97**, 024902(2005)
113 Y.-M. Sung, M.-K. Lee, K.-E. Kim and T.G. Kim, Chem. Phy. Lett., **443**, 319(2007)
114 Yu-Nu Hsu, S. Jeong, D.E. Laughlin and D.N. Lambeth, J. Appl. Phys., **89**, 7068(2001)
115 K. Kang, Z.G. Zhang, C. Papusoi and T. Suzuki, , Appl. Phys. Lett., **82**, 3284(2003)
116 D. C. Crew and L.H. Lewis, J. Appl. Phys., **87**, 4783(2000)
117 P.D. Mitchler, R.M. Roshko, and E.Dan Dahlberg, J. Appl. Phys., **85**, 4385(1999)
118 D. McLean, *Grain Boundaries in Metals*, Oxford University Press, Oxford, (1957)
119 D. Mainardi and P. Balbuena, Int. J. Quan. Chem., **85**, 580(2001)
120 James M. Howe, *Interfaces in Materials: Atomic Structure, Thermodynamics and Kinetics of Solid-Vapor, Solid-Liquid and Solid-Solid Interfaces*, John Wiley & Sons, Inc., (1997)
121 H. Kanazawa, G. Lauhoff and T. Suzuki, J. Appl. Phys., **87,** 6143(2000)
122 A. A. Kündig, N. Abe, M. Ohnuma, T. Ohkubo, H. Mamiya, and K. Hono, Appl. Phys. Lett., **85**, 789(2004)
123 J.G. Zhu and Y.H. Tang, J. Appl. Phys., **99**, 08Q903(2006)
124 T.Suzuki, K.Harada, N.Honda, K.Ouchi, J.Magn.Magn.Mater., **193** 85(1999)
125 C. H. Lai, C. H. Yang, C. C. Chiang, and T. K. Tseng, Appl.Phys.Lett., **85**, 4430(2004)
126 Y.F.Ding, J.S.Chen, E.J.Liu, C.J.Sun, G.M.Chow, J.Appl.Phys., **97**, 10H303(2005)
127 Y.-N. Hsu, S. Jeong, D. N. Lambeth, D. Laughlin, IEEE Trans. Magn., **36**, 2945(2000)
128 J.S.Chen, B.C.Lim, T.J.Zhou, J.Vac.Sci.Technol. A, **23**, 184(2005)